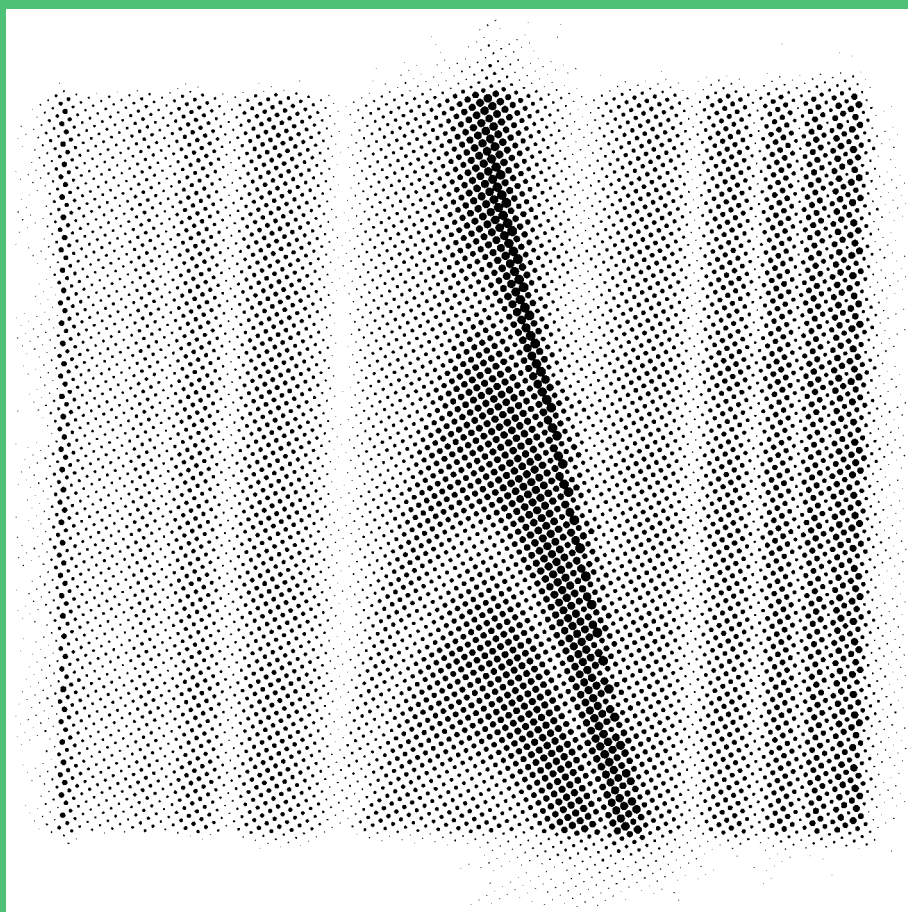


# Phase Resolved Dark-Field X-ray Microscopy

Mads Allerup Carlsen





## **Phase Resolved Dark-Field X-ray Microscopy**

PhD Thesis  
August 31, 2022

By  
Mads Allerup Carlsen

Copyright:      Reproduction of this publication in whole or in part must include the customary bibliographic citation, including author attribution, report title, etc.  
Published by:   DTU, Department of Physics, Fysikvej, Building 309, 2800 Kgs. Lyngby Denmark

## Approval

This thesis has been prepared over 2019-2022 at the Section for Neutrons and X-rays for Materials Physics (NEXMAP) and the Section for Nanoscale Materials and Devices (NANOMADE), Department of Physics, at the Technical University of Denmark (DTU). The study was funded by European Research Council through starting grant No. 804665. The supervisors were Hugh Simons and Henning Friis Poulsen from DTU Physics.

Mads Allerup Carlsen -



.....  
*Signature*

30/08/2022

.....  
*Date*

## Abstract

This thesis presents dark-field x-ray microscopy (DFXM) as a tool for characterizing ferroelectric domain structures and investigates new approaches to the data analysis of DFXM images based on methods from computational, coherent microscopy.

The underlying theory of DFXM is described and applied to study characteristic diffraction peak splitting due to coherent twinning in perovskite ferroelectrics. This constitutes the first quantitative comparison of DFXM measurements with theoretical predictions based on coherent twinning of ferroelectrics and thereby provides new evidence for the quantitative nature of DFXM.

It is shown that using Fourier Ptychography (FP), the phase-profile of the x-ray beam in transmission- and Bragg-scattering experiments can be recovered. This is promising for the study of crystals containing inversion domain boundaries, that are visible to x-ray scattering in the phase of the scattered beam. Furthermore, images of the complex aperture-function of the objective lens can be acquired. The reconstructions do not succeed in improving the resolution of the images compared to the conventional data-analysis which is shown to be identical to a kind of differential phase contrast (DPC).

Several experimental challenges are investigated both theoretically and experimentally. This includes thick-lens behavior of the applied CRL objective lenses, multiple x-ray scattering effects in the sample crystal, and partial coherence of the incident x-ray light. The role of these experimental sources of error are discussed both in relation to conventional DFXM as well as FP. Finally, a complete simulation of a DFXM experiment based on the propagation of coherent wave fronts and the Takagi-Taupin approach to dynamical scattering is presented. The simulation is compared to experiment and good agreement is found.

## Resumé

I denne afhandling præsenteres Dark-Field X-ray Microscopy (DFXM) som en værktøj til karakterisering af ferroelektriske domænestrukturer og nye metoder til databehandling af DFXM data undersøges, baseret på metoder fra computerbaseret kohærent mikroskopi.

Den tilgrundliggende teori bag metoden bliver beskrevet og anvendt til at studere karakteristiske splitting af diffraktionspletter i ferroelektrika med preovskit strukturen. Dette udgør den første kvantitative sammenligning af DFXM målinger med teoretiske forudsigelser baseret på den mekaniske teori for tvillingekrystaller i ferroelektrika.

Det demonstreres at Fourier Ptychografi (FP) kan benyttes til at genskabe faseprofilen af røntgenstrålen i transmissionsgeometri og Bragg-sprædningsgeometri. Dette er lovende for at kunne studere krystaller med inversionsdomæner, som kun er synlige for røntgensprædningseksperimenter i fasen af den sprædte stråle. Derudover kan billeder af den komplekse blændefunktion opnås. Rekonstruktionerne lykkedes ikke med at forbedre opløsningen af billederne, sammenlignet med den konventionelle dataanalyse i DFXM, som kan omformuleres som en slags differential fasekontrast (DPC)

Adskillelige eksperimentelle udfordringer undersøges både teoretisk og eksperimentelt. Dette inkluderer tyk-linse effekter, multiple sprædning i prøvekrystallen og partiel kohærens i den indkommende røntgenstråle. Konsekvenserne af disse eksperimentelle fejlkilder bliver diskuteret i relation til konventionel DFXM så vidt som FP. Til sidst præsenteres en komplet computersimulering af DFXM baseret på propagering af kohærente bølgefonter og Takagi-Taupin formuleringen af dynamisk sprædning. Resultaterne af sådan en simulering sammenlignes med eksperimentale billeder og god overensstemmelse findes.

## Acknowledgements

I would like to thank my supervisors Hugh Simons for giving me the opportunity of this PhD project and guiding me over these past 3 years and Henning Friis Poulsen for much good advice and encouragement.

I am grateful to the people at the ID06 beamline, Carsten Detlefs, Raquel Lamas-Rodriguez and Can Yildirim. Both for their hard work and valuable advice in direct connection to this PhD project but especially for being very welcoming and taking good care of me during my stay at the ESRF. Also to Rafael Celestre, Laura Wollesen and Julia Garriga-Ferrer for fruitful scientific discussions.

A thanks is owed to my fellow PhD students at NEXMAP, Philipp Lenzen, Winjie Wan and Mathias Huss-Hansen for sharing many good times and for keeping me sane during hard months of quarantine in the first year of the COVID-19 pandemic.

A great number of people at DTU Physics have helped me with various small and large practical problems. Peter Willendrup, Erik Bergbäck Knudsen and Ole Holm Nielsen for tech support of various kinds and Hanne Sørensen, Helle Grunnet-Jepsen, and Christina Rochat for patient and much appreciated (and much needed) help with sorting out paperwork.

Finally a great thanks to my colleagues at DTU who have been involved in this project one way or another, Jeppe Ormstrup, Antonella Gayoso, Leonardo Oliveira, Trygve Ræder, Theodor Holstad, Marion Höfling, Mads Laursen, Mustafacan Kutsal, Albert Zelenika, Sina Borghi, and others who I have briefly forgotten.



# Contents

Preface . . . . .	ii
Abstract . . . . .	iii
Resumé . . . . .	iv
<b>1 Introduction</b>	<b>1</b>
<b>2 X-ray Scattering</b>	<b>3</b>
2.1 Derivation of the Takagi-Taupin Equations . . . . .	3
2.2 Dynamical scattering in the two beam case . . . . .	6
2.3 Kinematical scattering & geometric optics . . . . .	14
<b>3 Dark-Field X-ray Microscopy with twinned crystals</b>	<b>19</b>
3.1 The geometry of a DFXM instrument . . . . .	21
3.2 Twinned crystals . . . . .	31
3.3 Experimental demonstration . . . . .	35
<b>4 Paraxial Fourier optics and coherent phase contrast microscopy</b>	<b>45</b>
4.1 Free-space propagation . . . . .	45
4.2 The projection approximation . . . . .	46
4.3 Discetization & numerical calculations . . . . .	50
4.4 Differential phase contrast (DPC) . . . . .	52
4.5 Fourier ptychography (FP) . . . . .	58
4.6 Examples of FP reconstructions . . . . .	61
<b>5 Aberrated compound refractive lenses</b>	<b>67</b>
5.1 CRLs in the thin lens approximation . . . . .	67
5.2 The quadratic-phase propagator . . . . .	69
5.3 Effective apertures . . . . .	74
5.4 Aberrated lenses . . . . .	76
<b>6 Implementing Fourier ptychography in an X-ray microscope</b>	<b>81</b>
6.1 Experimental description . . . . .	81
6.2 Registration correction . . . . .	83
6.3 Transmission experiments . . . . .	86
6.4 Thin film Bragg-reflection experiments . . . . .	93
6.5 Role of the decoherer . . . . .	98
6.6 Discussion & outlook . . . . .	99
<b>7 Simulating a Dark-Field X-ray Microscope</b>	<b>103</b>
7.1 Characterizing the incident beam . . . . .	103
7.2 Model of the sample crystal . . . . .	107
7.3 Integrating the Takagi-Taupin Equations . . . . .	110
7.4 Propagating through the imaging forming optics . . . . .	116
7.5 Comparison with experiment . . . . .	118
7.6 Future prospects for simulations . . . . .	121
<b>A Appendicies</b>	<b>131</b>
A.1 Fourier series & crystallography . . . . .	131

A.2 Properties of the continuous Fourier transform . . . . . 132

# 1 Introduction

Many functional properties of crystalline materials are thought to be influenced by the generation, annihilation and movement of crystal defects. The macroscopic properties of the materials are the result of complicated interactions between these defects with the lattice, other defects in the crystal, grain boundaries, and macroscopic fields. This is fundamentally a problem with multiple length-scales ranging from the unit cell of the crystal lattice to the size of the macroscopic object of interest. The understanding of these materials therefore require methods that cover all these length-scales.

Ferroelectrics are one such family of materials with a long list of technological applications, ranging from dielectric layers in capacitors to ultrasonic transducers. These materials are used for their strong electrical and mechanical response to external perturbations which is caused by the movement of twin-domain boundaries. Microscopic studies of these materials typically only probe the surfaces of large samples or thin slices that must be cut out of macroscopic samples. These samples are therefore taken out of the environment where they are used and the interactions with the features on longer length scales are lost.

Dark-Field X-ray Microscopy (DFXM)[66, 59] is a microscopy technique that makes full advantage of the high penetrating power of x-rays to non-destructively image small buried volumes (field of view  $\approx 300\ \mu\text{m}$ ) of a macroscopic sample in a realistic sample environment with sub-micron resolution. Thanks to the high sensitivity of x-ray scattering to small lattice distortions DFXM has excellent angular sensitivity ( $\approx 10^{-4}$  rad) and is able to image fundamental defects of the crystal lattice such as twin-domain boundaries and dislocations.

DFXM has been used to study a broad spectrum of phenomena including re-crystallization in deformed polycrystalline metals,[2, 85] failure in battery materials,[16] lattice distortions in bio-minerals,[63] and dynamics of fundamental defects in large single crystals.[54, 22]

Ferroelectrics constitute interesting samples for DFXM as they form hierarchical structures over a long range of length scales. The most important defect is the *twin-domain boundary* or the *domain wall*, a planar defect that separates two different regions of different space group symmetry. This domain structure arises from the slight breaking of a number of symmetries that are still approximately maintained in the ferroelectric crystal. The application of these broken symmetries on the ferroelectric crystal generates a number of different domain variants separated by domain walls. Because the symmetry breaking is small, the lattices of the different domains can also be regarded as slightly strained and rotated versions of each other.

From an x-ray scattering point of view, it is useful to distinguish two different types of domain walls: *Elastic domain walls* are domain walls that separate two domains of the crystal where the lattices are related by a rotation (or mirror-symmetry) that is not a symmetry of the point group of either lattice. And *non-elastic domain walls* where the twinning symmetry is a symmetry of the point group and both domains have the same point group. Typically in ferroelectrics, the non-elastic domain walls are those where the spontaneous polarization between the two domains are anti-parallel.

The non-elastic domain walls are a particular challenge to image with DFXM as the crystal lattice is not affected by the domain wall. Therefore the Bragg-condition is the same in

the two domains and x-ray beam is scattered into the same direction. For this reason, the normal approach to data analysis in DFXM, which relies on determining the direction of the scattered beam, does not work to characterize these domain walls. This however does not mean that the domain walls do not generate contrast in DFXM images. The phase of the scattered beam is different on each side of the domain wall which should give subtle phase-contrast on the images.

The overarching goal of the work done in the course of this PhD programme was to investigate whether computational phase contrast microscopy methods can be implemented on a DFXM instrument to yield a new approach to data analysis that can account for the contrast caused by these domain walls and possibly other sample features, that cause phase contrast.

The theoretical description of the DFXM method in the existing literature[59] has relied on geometric optics. To understand the phase contrast in DFXM, we need results from wave-optics. For this we use the formalism of the Takagi-Taupin equations(TTE)[72, 74, 73] to treat the scattering in the sample-crystal and a cascaded-lenses approach to model the compound refractive lenses(CRL) used as the objective lens the the microscope.

In the wave-optics description of DFXM, we can describe the measurement as a band-pass filtered image of a high-resolution scattering function, where the position of the filter is scanned in 3D reciprocal space. This is similar to certain methods in computational visible light microscope such as differential phase contrast(DPC) and Fourier ptychography(FP) which we implement on the existing hardware of the ID06-HXM instrument in a proof-of-principle experiment.

We have developed and presented a numerical approach to simulate the full DFXM experiment including multiple-scattering events, partial coherence, thick-lens effects in the CRL, and aberrations. This simulation is compared against experimental data from a near perfect crystal containing a stacking fault, which can be seen as a kind of prototype of the inversion domain boundary that displays only phase contrast.

All in all, this thesis provides a comprehensive presentation of the DFXM method in the view of coherent optics and discusses a number of errors and experimental challenges that the method is faced with.

## 2 X-ray Scattering

In this chapter we will derive the equations of x-ray scattering by a periodic medium and derive a number of equations that will be used throughout the rest of this thesis.

Often when x-ray scattering is treated, multiple scattering effects are small and can be ignored. This leads to the *kinematical* theory of x-ray scattering. This turns out to be insufficient for DFXM where multiple scattering effects are a common source of errors and a fundamental restriction to be considered when designing experiments. We therefore need to include these multiple scattering events and derive what is known as the *dynamical* theory of X-ray scattering.

We start by deriving the Takagi-Taupin-equations, which are the dynamical equations for scattering by a deformed crystal. We recover the theory for scattering by perfect crystals as a special solution to these equations. Finally, we make the approximations to arrive at the kinematical equations and geometric optics.

### 2.1 Derivation of the Takagi-Taupin Equations

X-rays are a part of the electromagnetic spectrum with wavelengths in the range below 10 nm.[4] X-rays have a number of desirable qualities that are utilized in DFXM: they are able to penetrate through thick ( $>10\ \mu\text{m}$ ) samples of dense material, and because the wavelength is on the same order of magnitude as the lattice parameter of crystalline materials, interference of the scattered waves lead to scattering at large angles, characteristic of the crystal structure.

Like in any other classical problem concerning electromagnetic radiation, the governing equations are the Maxwell's equations:

$$\begin{aligned}\nabla \cdot \mathbf{D} &= \rho_f \\ \nabla \times \mathbf{E} &= -\frac{\partial \mathbf{B}}{\partial t} \\ \nabla \cdot \mathbf{B} &= 0 \\ \nabla \times \mathbf{H} &= \mathbf{J}_f + \frac{\partial \mathbf{D}}{\partial t}\end{aligned}\tag{2.1}$$

At x-ray frequencies, we can assume that the charge distribution does not have time to respond to the rapidly changing fields and therefore the charge and current terms are zero. Taking the curl of the second equation yields:

$$\nabla \times (\nabla \times \mathbf{E}) = \nabla \times \left( -\frac{\partial \mathbf{B}}{\partial t} \right)\tag{2.2}$$

Assuming no magnetic response ( $\mathbf{B} = \mu_0 \mathbf{H}$ ) and no free currents ( $\mathbf{J}_f = 0$ ) we can eliminate the magnetic field from the expression, by inserting the fourth of Maxwell's equations:

$$\nabla \times (\nabla \times \mathbf{E}) = -\mu_0 \frac{\partial}{\partial t} (\nabla \times \mathbf{H}) = -\mu_0 \frac{\partial^2 \mathbf{D}}{\partial t^2}\tag{2.3}$$

Using an identity for the curl-of-curl, we can rewrite this equation in terms of the vector laplacian and the gradient of the divergence.

$$\nabla(\nabla \cdot \mathbf{E}) - \nabla^2 \mathbf{E} = -\mu_0 \frac{\partial^2}{\partial t^2} \mathbf{D} \quad (2.4)$$

Assuming a linear, isotropic, local, and instantaneous response means:  $D = \epsilon_0(1 + \chi(\mathbf{r}))E$ . Importantly, we do not assume that the medium is homogeneous and the susceptibility  $\chi(\mathbf{r})$  is allowed to vary as a function of position in space,  $\mathbf{r}$ . We can then write the equation only in terms of the  $\mathbf{E}$ -field:

$$\nabla(\nabla \cdot \mathbf{E}) - \nabla^2 \mathbf{E} = -\mu_0 \epsilon_0 (1 + \chi(\mathbf{r})) \frac{\partial^2}{\partial t^2} \mathbf{E} \quad (2.5)$$

Introducing the monochromatic vector field  $\mathbf{E}(\mathbf{r}, t) = \exp(-i\omega t) \mathbf{E}'(\mathbf{r})$  we finally arrive at the Helmholtz equation for monochromatic radiation in a medium:

$$\nabla^2 \mathbf{E} - \nabla(\nabla \cdot \mathbf{E}) = -k^2 (1 + \chi(\mathbf{r})) \mathbf{E} \quad (2.6)$$

Here we have utilized the equation  $\mu_0 \epsilon_0 = 1/c^2$  and defined  $k = \omega/c$ .  $c$  is the speed of light in a vacuum.

### 2.1.1 Perfect periodic medium

We want to solve the Helmholtz equation for the propagation of a monochromatic, linearly polarized X-ray beam inside a periodic medium. With the term *beam* we mean a field that is spatially confined in two directions orthogonal to the direction of propagation, given by the vector  $\mathbf{k}_0$ . The field of such a beam can be written as a modulated plane wave:

$$\mathbf{E}(\mathbf{r}) = E(\mathbf{r}) e^{-i\mathbf{k}_0 \cdot \mathbf{r}} \mathbf{p} \quad (2.7)$$

Where  $\mathbf{p}$  is the polarization vector. Importantly, the scalar envelope function  $E(\mathbf{r})$  should be a slowly varying function on the scale of the wavelength,  $\lambda = 2\pi c/\omega$ . This requirement does not give a unique choice of  $\mathbf{k}_0$  as a small change of this vector by a value much smaller than one over the wavelength will also yield a slowly varying envelope function.

In a periodic medium, we can write the susceptibility as a Fourier series:

$$\chi = \sum_{\mathbf{h}'} \chi_{\mathbf{h}'} \exp(-i\mathbf{h}' \cdot \mathbf{r}) \quad (2.8)$$

where the sum runs over all the infinitely many reciprocal lattice vectors  $\mathbf{h}' = B[h, k, \ell]^T$  of the crystal. We use the bold  $\mathbf{h}$  to denote the reciprocal lattice vector in units of angular spatial frequency (rad/length) and we use the italic  $h$  as a subscript as a shorthand for the three integer indexes. The constants  $\chi_{\mathbf{h}'}$  are the Fourier coefficients of the periodic susceptibility function.  $\chi_0$  is the average electric susceptibility of the crystal that describes both refraction and absorption in the situations where Bragg-scattering can be ignored. Definitions of the notation used here is explained in Appendix A.1 along with a brief introduction to Fourier transforms and crystallography.

Now we make a guess for the solution to the Helmholtz equations which is a sum of modulated plane waves:

$$\mathbf{E}(\mathbf{r}) = \sum_{h''} \mathbf{E}_{h''}(\mathbf{r}) \exp(-i\mathbf{k}_{h''} \cdot \mathbf{r}) \quad (2.9)$$

where  $\mathbf{k}_{h''} = \mathbf{k}_0 + \mathbf{h}''$ .

We have not fully specified the choice of the vector  $\mathbf{k}_0$  yet. The conventional choice[72, 74, 73] is the complex wave vector of the refracted wave inside the crystal with  $|\mathbf{k}_0| = k(1 + 1/2\chi_0)$ . With this choice one arrives at two-beam equations, without the refraction/absorption term in the equation for the transmitted beam, but with complicated boundary conditions connecting the interior and exterior of the crystal.

Another choice, is to take  $\mathbf{k}_0$  as the average *vacuum* wave vector of the incident radiation, that is  $|\mathbf{k}_0| = k$ . This choice gives a set of more physically intuitive equations, the authors call them the *symmetrical* TTEs because the incident and scattered beam are handled equivalently.[78]

The functions  $\mathbf{E}_{h''}(\mathbf{r})$  are a set envelope functions of modulated plane waves.<sup>1</sup> They are assumed to be slowly varying functions, which will allow us to ignore terms involving their second derivatives.

We plug in these expressions for  $\mathbf{E}$  and  $\chi$  into equation 2.6 and rewrite term by term. First the vector laplacian:

$$\nabla^2 \mathbf{E} = \sum_{h''} (\nabla^2 \mathbf{E}_{h''} - 2i(\mathbf{k}_{h''} \cdot \nabla) \mathbf{E}_{h''} - |\mathbf{k}_{h''}|^2 \mathbf{E}_{h''}) \exp(-i\mathbf{k}_{h''} \cdot \mathbf{r}) \quad (2.10)$$

Now the grad-div term:

$$\begin{aligned} -\nabla(\nabla \cdot \mathbf{E}) &= -\nabla \left( \sum_{h''} \nabla \cdot \mathbf{E}_{h''} \exp(i\mathbf{k}_{h''} \cdot \mathbf{r}) - i \exp(i\mathbf{k}_{h''} \cdot \mathbf{r}) \mathbf{k}_{h''} \cdot \mathbf{E}_{h''} \right) \\ &\approx -\sum_{h''} \left( \nabla(\nabla \cdot \mathbf{E}_{h''}) + (\nabla \cdot \mathbf{E}_{h''}) i\mathbf{k}_{h''} \right) \exp(i\mathbf{k}_{h''} \cdot \mathbf{r}) \end{aligned} \quad (2.11)$$

where the  $\mathbf{k}_{h''} \cdot \mathbf{E}_{h''}$  terms have been omitted because the waves are approximately transverse. The first term on the final line is a 2nd order derivative of the slowly varying envelope function. The final term is also omitted in the usual form of the TTEs.[74, 40]

Right hand side of Eq. (2.6):

$$\begin{aligned} -k^2(1 + \chi)\mathbf{E} &= -k^2 \left( 1 + \sum_{h'} \chi_{h'} \exp(-i\mathbf{h}' \cdot \mathbf{r}) \right) \sum_{h''} \mathbf{E}_{h''} \exp(-i\mathbf{k}_{h''} \cdot \mathbf{r}) \\ &= -k^2 \sum_{h'} (\delta_{0h'} + \chi_{h'}) \exp(-i\mathbf{h}' \cdot \mathbf{r}) \sum_{h''} \mathbf{E}_{h''} \exp(-i\mathbf{k}_{h''} \cdot \mathbf{r}) \\ &= -k^2 \sum_{h', h''} (\delta_{0h'} + \chi_{h'}) \mathbf{E}_{h''} \exp(-i(\mathbf{k}_{h''} + \mathbf{h}') \cdot \mathbf{r}) \\ &= -k^2 \sum_{h', h''} (\delta_{h''h'} + \chi_{h''-h'}) \mathbf{E}_{h'} \exp(-i\mathbf{k}_{h''} \cdot \mathbf{r}) \end{aligned} \quad (2.12)$$

<sup>1</sup> These are sometimes called Bloch waves in the literature[74], but they are not the same as the usual Bloch-waves known from electron structure in crystals. In our case the fast variation is described by a harmonic and the slow variation is given by the arbitrary function.

Where the last line results from the second-to-last by the substitution  $h' \rightarrow h' - h''$  and then swapping the two dummy indices. Comparing Eq (2.10) and (2.12) we see that both the LHS and the RHS contain sums over  $h''$  and the same exponential functions. Since the complex exponentials constitute an orthogonal basis and the equation holds for any  $\mathbf{r}$ , the equation must hold term for term in the  $h''$  sum which, after some re-organization, gives the set of coupled equations:

$$2(\mathbf{k}_{h''} \cdot \nabla) \mathbf{E}_{h''} = -i \sum_{h'} \left( (k^2 - |\mathbf{k}_{h''}|^2) \delta_{h''h'} + k^2 \chi_{h''-h'} \right) \mathbf{E}_{h'} \quad (2.13)$$

for all  $h''$  in the reciprocal lattice. This is the general form of the TT equations. We will deal with scattering situations, where the incoming field is smooth and can be given by a single modulated plane wave,  $\mathbf{E}_0$ . In this case only waves where the term  $(|\mathbf{k}_{h''}|^2 - k^2)$  is close to zero will contribute significantly to the solution while all other terms are killed off due to destructive interference. Writing out this requirement as:  $|\mathbf{k}_0 + \mathbf{h}''|^2 = k^2$ , we recognize it as the Bragg-condition.

## 2.2 Dynamical scattering in the two beam case

We now look at the case where only a single reciprocal lattice vector satisfies the Bragg-condition. In this case only two modulated waves contribute significantly: the transmitted wave  $E_0$  and the scattered wave  $E_h$ . The set of equations (2.13) simplifies to two coupled differential equations.

We furthermore assume that the incident radiation consists of a single polarization state. Either we have  $\sigma$ -polarization where both  $\mathbf{E}_0$  and  $\mathbf{E}_h$  are orthogonal to the plane spanned by  $\mathbf{k}_0$  and  $\mathbf{k}_h$ , called *the scattering plane*. Or we have  $\pi$ -polarization, where both vectors fall within this plane. This approximation allows us to rewrite the vectorial equations as scalar equations by the introduction of the parameter  $C$ :

$$C = \begin{cases} 1 & \text{for } \sigma\text{-polarization.} \\ \cos(2\theta_0) & \text{for } \pi\text{-polarization.} \end{cases} \quad (2.14)$$

Where  $2\theta_0$  is the angle between the vectors  $\mathbf{k}_0$  and  $\mathbf{k}_h$ . The 2D plane spanned by these vectors is called *the scattering plane*.<sup>2</sup> The resulting two-beam TT equations are:

$$\begin{aligned} 2(\mathbf{k}_0 \cdot \nabla) E_0 &= -i(k^2 \chi_0 - (|\mathbf{k}_0|^2 - k^2)) E_0 - ik^2 C \chi_{\bar{h}} E_h \\ 2(\mathbf{k}_h \cdot \nabla) E_h &= -i(k^2 \chi_0 - (|\mathbf{k}_h|^2 - k^2)) E_h - ik^2 C \chi_h E_0 \end{aligned} \quad (2.15)$$

We now choose  $\mathbf{k}_0 = R(\mu) \mathbf{k}_0^{\text{Exact}}$  where  $\mathbf{k}_0^{\text{Exact}}$  is a wave-vector that exactly satisfies the Bragg condition and  $R(\mu)$  is a rotation within the scattering plane by an angle  $\mu$ . To illustrate the reciprocal space geometry of the  $k$ -vectors, one often makes use of a drawing called the Ewalds constructions. which is drawn as follows:

The 2D slice of reciprocal space parallel to the scattering plane and passing through zero is considered. The reciprocal lattice vectors of the crystal lattice are plotted as points where the zeroth lattice vector lies on the origin, labeled  $O$ . The wave vector of the

<sup>2</sup>This should not be confused with *the scattering planes*, which is sometimes used to denote the set of lattice planes corresponding to a given reciprocal lattice vector.

incident light is drawn in from a point  $T$  and ending on the origin. Now a circle is drawn centered on  $T$  with radius  $k$ . If any point of the reciprocal lattice falls on this circle, the Bragg condition is fulfilled for the reflection corresponding to that Bragg reflection. Figure 2.1 shows the Ewald construction for the two incident wave-vectors  $\mathbf{k}_0^{\text{Exact}}$  and  $\mathbf{k}_0$  used here.

Writing up the 2-beam TTEs with this choice yields:

$$\begin{aligned} 2(\mathbf{k}_0 \cdot \nabla) E_0 &= -ik^2 \chi_0 E_0 - ik^2 C_{\chi_{\bar{h}}} E_h \\ 2(\mathbf{k}_h \cdot \nabla) E_h &= -ik^2 (\chi_0 + \beta) E_h - ik^2 C_{\chi_h} E_0 \end{aligned} \quad (2.16)$$

where  $\beta = (|\mathbf{k}_h| - k^2)/k^2 \approx 2 \sin(2\theta_0) \mu$  and  $\bar{h}$  is used as a shorthand for  $-h$ . These are the same symmetric 2-beam TT equations as stated by [78].

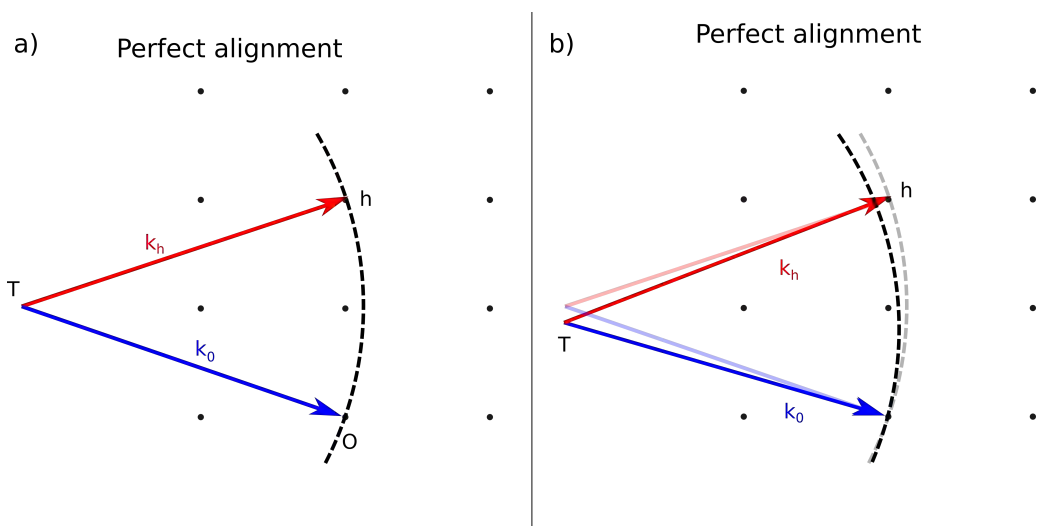


Figure 2.1: Ewald construction for 2-beam diffraction a) with exact satisfaction of the Bragg condition and b) a slightly rotated geometry. In the rotated geometry,  $\mathbf{k}_h$  does not end on the Ewald sphere.

## 2.2.1 Ewald-Laue Theory

In the simplest geometric case, that of a plane wave incident on a perfect semi crystal (spanning the semi-infinite space  $z > 0$ ) we can calculate analytical solutions to the TT equations. The result of this is known as Ewald-Laue theory<sup>3</sup> and will give us the characteristic length-scales of dynamical diffraction as well as insight into some of the features we can expect to see in the diffraction patterns of near-perfect crystals. Our approach shall be to solve the PDEs (2.16) in a semi crystal for  $z > 0$  as boundary-value problems in a single variable  $z$  utilizing the fact that both the crystal and initial condition is constant in the two transverse directions. We distinguish between two different geometries: the *Laue-geometry* (transmission) where both the incident and the scattered beam propagate into the semi-crystal, and the *Bragg-geometry* (reflection) where the scattered beam

<sup>3</sup>Named after the two authors who developed it in 1917[26] and in 1931[49] respectively.

travels out of the crystal. For simplicity we only write up the result for symmetric geometries, where both the incident and the scattered beam make the same angle relative to the surface. The two different geometries are sketched in Fig 2.2.

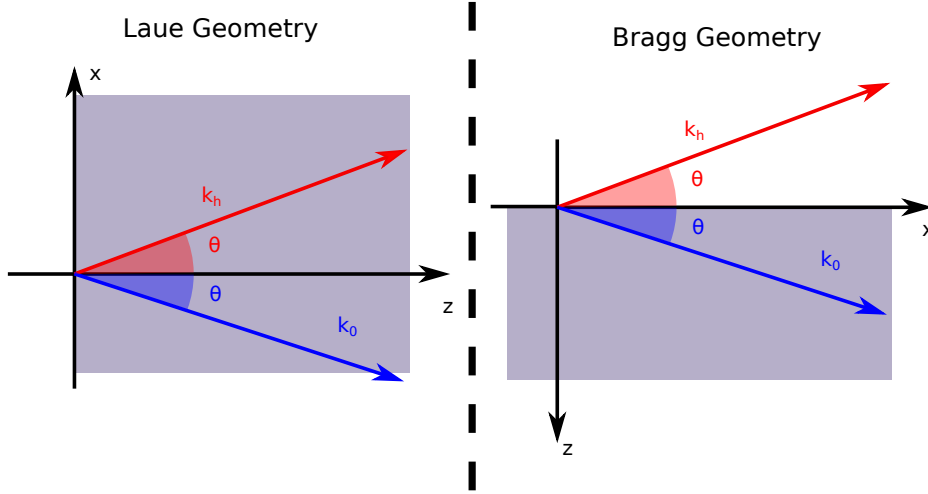


Figure 2.2: Schematic drawing of symmetric Laue and Bragg geometries. Note the different coordinate systems.

### Symmetric Laue diffraction

In Laue diffraction both the transmitted and the scattered waves travel into the crystal. *Symmetric* means that both waves make the same angle with the surface normal, or equivalently, that the scattering vector is orthogonal to the surface normal. This condition can be written:  $\mathbf{k}_0 \cdot \hat{z} = \mathbf{k}_h \cdot \hat{z} = k \cos(\theta_0) > 0$ , where  $\theta_0$  is half of  $2\theta_0$ . The appropriate boundary conditions (which in this case turns out to be a pair of initial conditions) is:  $E_0(x, y, 0) = E_{\text{init}}$  and  $E_h(x, y, 0) = 0$ .

The PDEs (2.16) turn into a pair of coupled homogeneous linear ODEs in the parameter,  $z$  and can be written:

$$\frac{d}{dz} \begin{bmatrix} E_0 \\ E_h \end{bmatrix} = \frac{k}{2i \cos(\theta_0)} \begin{bmatrix} \chi_0 & C\chi_{\bar{h}} \\ C\chi_h & \chi_0 + \beta \end{bmatrix} \begin{bmatrix} E_0 \\ E_h \end{bmatrix} \quad (2.17)$$

The system has two linearly independent solutions (called *wave fields* in the traditional literature on the subject) found by solving the eigenvalue problem of the 2-by-2 system matrix. The Eigenvalues are:

$$\lambda_{\pm} = \frac{k}{2i \cos \theta} \left( \chi_0 + \beta/2 \pm \sqrt{C^2 \chi_{\bar{h}} \chi_h + (\beta/2)^2} \right) \quad (2.18)$$

and the eigenvectors are:

$$\mathbf{v}_{\pm} = \begin{bmatrix} \frac{\beta}{2\chi_h} \pm \sqrt{C^2 \chi_{\bar{h}} \chi_h + (\beta/2)^2} / \chi_h \\ -1 \end{bmatrix} \quad (2.19)$$

The solution that satisfies the initial condition, is given by:

$$\mathbf{E} = \frac{E_0 C \chi_h}{\sqrt{C^2 \chi_h \chi_{\bar{h}} + (\beta/2)^2}} (\mathbf{v}_+ \exp(z\lambda_+) - \mathbf{v}_- \exp(z\lambda_-)) \quad (2.20)$$

In the special case where  $\mu = 0$  and assuming that the product  $\chi_h \chi_{\bar{h}}$  is real<sup>4</sup>, the result simplifies to:

$$\begin{aligned} E_0(z) &= E_0 \exp\left(z \frac{k\chi_0}{2i \cos(\theta)}\right) \cos\left(z \frac{k}{2 \cos(\theta)} C \sqrt{\chi_h \chi_{\bar{h}}}\right) \\ E_h(z) &= -E_0 \sqrt{\frac{\chi_h}{\chi_{\bar{h}}}} \exp\left(z \frac{k\chi_0}{2i \cos(\theta)}\right) \sin\left(z \frac{k}{2 \cos(\theta)} C \sqrt{\chi_h \chi_{\bar{h}}}\right) \end{aligned} \quad (2.21)$$

The solution here is an exponentially dampened oscillation traveling into the crystal, with an attenuation length  $L_{\text{Att.}} = -\frac{\pi \cos(\theta)}{\lambda \text{Im}(\chi_0)}$  and an oscillation period of  $L_{\text{Pendel.}} = \frac{\lambda \cos(\theta)}{\pi C \sqrt{\chi_h \chi_{\bar{h}}}}$ . Oscillating solutions of this kind are abundant in dynamical diffraction in a lot of different geometries and when they can be observed as fringes in scattering patterns or rocking curves they are called *pendellösung fringes* due to the similarity of Eq. (2.17) with the equation of a pendulum.

### Symmetric Bragg diffraction

In Bragg diffraction the transmitted beam travels into the crystal, but the scattered beam travels out of the crystal. Symmetric means that both waves make the same angle with the surface or equivalently that the scattering vector is normal to the surface. This condition can be written:  $\mathbf{k}_0 \cdot \hat{z} = -\mathbf{k}_h \cdot \hat{z} = k \sin(\theta_0)$ . The boundary conditions this time read:  $E_0(x, y, \infty) = E_h(x, y, \infty) = 0$ .

We can again write the TT equations as a pair of coupled ODEs now with a sign change for the scattered beam:

$$\frac{d}{dz} \begin{bmatrix} E_0 \\ E_h \end{bmatrix} = \frac{k}{2i \sin(\theta)} \begin{bmatrix} \chi_0 & C\chi_{\bar{h}} \\ -C\chi_h & -\chi_0 - \beta \end{bmatrix} \begin{bmatrix} E_0 \\ E_h \end{bmatrix} \quad (2.22)$$

We can calculate the eigenvalues:

$$\lambda_{\pm} = \frac{k}{2i \sin \theta} \left( \pm \sqrt{(\chi_0 + \beta/2)^2 - C^2 \chi_{\bar{h}} \chi_h - \beta/2} \right) \quad (2.23)$$

and eigenvectors:

$$\mathbf{v}_{\pm} = \begin{bmatrix} \frac{\chi_0 + \beta/2}{\chi_h} \pm \sqrt{(\chi_0 + \beta/2)^2 - C^2 \chi_{\bar{h}} \chi_h} / \chi_h \\ -1 \end{bmatrix} \quad (2.24)$$

The boundary conditions are only satisfied by the one of these two solutions, which decays exponentially into the crystal. This is the case only for the eigenvalue with negative real part. Which one of the two eigenvalues has a negative real part changes from one

<sup>4</sup>This is the case when anomalous absorption effects can be ignored.

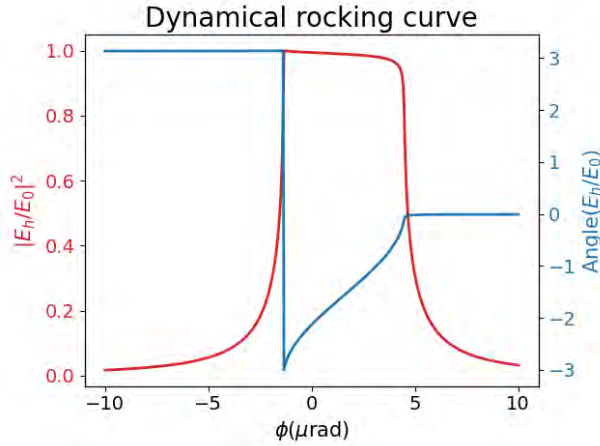


Figure 2.3: The Darwin reflectivity curve in a Bragg geometry as given in Eq. (2.24) calculated with typical parameters for diamond at 17keV for the (111) reflection.

side of the rocking curve to the other. The first component of the corresponding wave-vector gives the relative amplitude of the scattered wave to the direct wave which is the same as the reflectivity of the crystal. It is difficult to write a closed-form expression of this function but numerical computation is straight forward. A plot of this function is shown in Fig 2.3. The reflectivity curve has a characteristic width called the Darwin width and falls off sharply on either side of this plateau. The reflectivity curve is shifted by a small angle from  $\mu = 0$  due to refraction.

At  $\beta = \chi_0 = 0$  and  $\chi_{\bar{h}}\chi_h$  real, the solution has the shape:

$$\begin{aligned} E_0(z) &= E_0 \exp\left(-z \frac{kC\chi_h}{2 \sin(\theta)}\right) \\ E_h(z) &= E_0 \exp\left(-z \frac{kC\chi_h}{2 \sin(\theta)}\right) \end{aligned} \quad (2.25)$$

This solution shows an exponential decay of intensity into the crystal with characteristic length:  $L_{EX.} = \frac{\lambda \sin(\theta)}{\pi |C\chi_h|}$ . This phenomenon is known as *extinction*<sup>5</sup> and for hard x-rays is typically much faster than the attenuation characterized by the attenuation length  $L_{Att.}$ . This ensures that x-rays close to the Bragg condition only penetrate a short distance into a perfect crystal in the Bragg-geometry.

## 2.2.2 Deformed crystals

Takagi[72] extended the dynamical diffraction theory to deformed crystals. For deformed crystals, the Fourier series representation of equation (2.8) does not hold exactly. Rather we introduce the spatially varying susceptibility functions, called scattering functions:

$$\chi'_h(\mathbf{r}) = \chi_h \exp(i\mathbf{u}(\mathbf{r}) \cdot \mathbf{h}) \exp(i\mathbf{r} \cdot \Delta\mathbf{Q}) \quad (2.26)$$

<sup>5</sup>Sometimes *secondary extinction* or *dynamical extinction*.

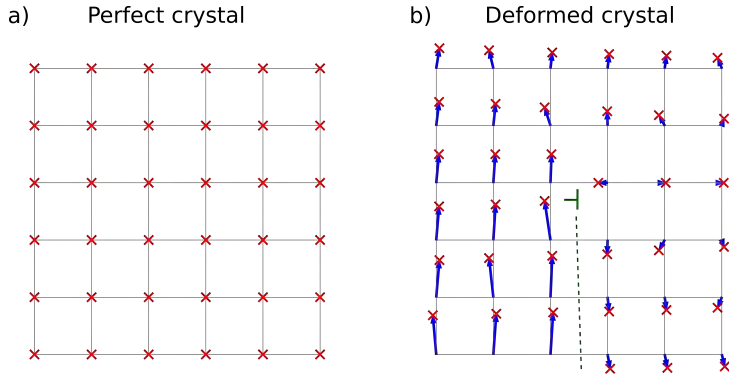


Figure 2.4: Drawing of a) a perfect and b) a deformed crystal. The red crosses mark the positions of atoms, the blue arrows are the  $\mathbf{u}_n$  vectors. The green T marks a dislocation and the dashed line marks an apparent discontinuity in the displacement field.

Where  $\mathbf{u}(\mathbf{r})$  is the displacement field from continuum mechanics. We assume that a given distorted crystal may be described as a deformed version of an initially perfect crystal where the atoms have been moved from their ideal positions. In an atomistic view, a given atom,  $n$  sat at a position in the initial perfect crystal,  $\mathbf{r}_n^{(i)}$ . After the deformation that same atom has been moved to a new position  $\mathbf{r}_n^{(f)}$ . The displacement of every atom is then the distance between these two points  $\mathbf{u}_n = \mathbf{r}_n^{(f)} - \mathbf{r}_n^{(i)}$ . In transitioning to a continuum model, we assume that atoms close to each other are displaced by similar vectors and as such we can define a continuous field  $\mathbf{u}(\mathbf{r}) \in \mathbb{R}^3 \rightarrow \mathbb{R}^3$  where:

$$\mathbf{u}_n = \mathbf{u}(\mathbf{r}_n^{(i)}) \quad (2.27)$$

A sketch of this situations is drawn in Fig. 2.4.

Of central interest are the partial derivatives of the displacement field, that can be collected into a tensor:

$$\nabla \mathbf{u} = \begin{bmatrix} \nabla \mathbf{u}_{11} & \nabla \mathbf{u}_{12} & \nabla \mathbf{u}_{13} \\ \nabla \mathbf{u}_{21} & \nabla \mathbf{u}_{22} & \nabla \mathbf{u}_{23} \\ \nabla \mathbf{u}_{31} & \nabla \mathbf{u}_{32} & \nabla \mathbf{u}_{33} \end{bmatrix} = \begin{bmatrix} \frac{\partial \mathbf{u}_1}{\partial x} & \frac{\partial \mathbf{u}_1}{\partial y} & \frac{\partial \mathbf{u}_1}{\partial z} \\ \frac{\partial \mathbf{u}_2}{\partial x} & \frac{\partial \mathbf{u}_2}{\partial y} & \frac{\partial \mathbf{u}_2}{\partial z} \\ \frac{\partial \mathbf{u}_3}{\partial x} & \frac{\partial \mathbf{u}_3}{\partial y} & \frac{\partial \mathbf{u}_3}{\partial z} \end{bmatrix} \quad (2.28)$$

where  $\mathbf{u}_{1,2,3}$  refer to the  $x$ ,  $y$ , and  $z$  components of the displacement field.

A complication arises here when the deformed crystal contains dislocations. In this case the displacement field will contain a discontinuity along an infinite half-plane where the derivative is then not defined. It turns out however, that the gradient approaches the same value from both sides of the discontinuity, so we can define a smooth gradient function that only has a divergence along the dislocation core.

Also, we note that the discontinuities that appear in the displacement field due to dislocations will always have the magnitude of a lattice vector. Therefore the dot product of this discontinuity with  $\mathbf{h}$ , as it appears in Eq. 2.26, gives an integer times  $2\pi$  and does not give a discontinuity in the scattering functions except a phase-vortex at the dislocation core.

The second factor in Eq. (2.26) describes small rotations of the crystal where  $\Delta\mathbf{Q} = R\mathbf{Q} - \mathbf{Q}$  and  $R$  is the rotation matrix describing the rotation of the crystal. Rotations of the crystal can also be handled by the  $\beta$  factor of the previous subsections or by a modification of the initial condition. We will prefer to use the  $\beta$  parameter for numerical calculations in the later chapters.

The introduction of the displacement field complicates the derivation of the TT equations significantly and changes the approximations needed to reach them, but does ultimately not change the final shape of the equations. We skip the derivation here and refer to the original papers.[74, 73]

### 2.2.3 Perfect crystal propagators

Scattering by a perfect crystal of any incident light can be handled by a method similar to the one shown in Section 2.2.1 for plane-wave illumination. Utilizing the continuous Fourier transform, any incident monochromatic wave-field can be decomposed into plane waves of different angle of incidence. The scattered and transmitted light can thus be found by first Fourier transforming the incident wave field and then solving a 2-by-2 eigenvalue problem for each component to find the complex reflectivity and transmittivity for each plane wave component. Finally we inverse Fourier transform the reflectivity and transmittivity times the Fourier coefficients of the incident light to find the profile of the scattered and transmitted beams.

The final result will have the shape of a Fourier convolution and is conceptually similar to a family of operators – called propagators – used to calculate the propagation of light through a vacuum. We therefore call this a *perfect crystal propagator*. Such a method has been described and implemented in the computer-program, SRW[71] which however only treats Bragg-geometry so we give a derivation for Laue geometries here.

We focus on an infinite slab-shaped (with two parallel infinite surfaces) crystals of finite thickness,  $t$ . We define an orthogonal grid with the three orthonormal unit-vectors  $\hat{\mathbf{x}}$ ,  $\hat{\mathbf{y}}$ , and  $\hat{\mathbf{z}}$ . As for the Ewald-Laue theory we require that  $\hat{\mathbf{z}}$  is parallel to the normal vector of the surface where the beams exit the crystal. We are interested in a Laue-geometry which is to say:

$$\mathbf{k}_0 \cdot \hat{\mathbf{z}} = \mathbf{k}_{0,\perp} > 0 \quad \text{and} \quad \mathbf{k}_h \cdot \hat{\mathbf{z}} = \mathbf{k}_{h,\perp} > 0, \quad (2.29)$$

such that the  $z$ -axis takes the role of a quasi-optical axis. We can treat  $z$  as the dynamical variable and  $x$  and  $y$  as transverse variables. To this end, we decompose the vectors  $\mathbf{k}_0$  and  $\mathbf{k}_h$  into their  $z$ -components and their projection onto the  $x - y$  plane, i.e.  $\mathbf{k}_0 = k_{0,z}\hat{\mathbf{z}} + \mathbf{k}_{0,\perp}$  and  $\mathbf{k}_h = k_{h,z}\hat{\mathbf{z}} + \mathbf{k}_{h,\perp}$ . We can now re-write Equations (2.15) as:

$$\begin{aligned} 2k_{0,z} \frac{\partial}{\partial z} E_0(\mathbf{r}) &= -ik^2 \chi_0 E_0(\mathbf{r}) - 2(\mathbf{k}_{0,\perp} \cdot \nabla_{\perp}) E_0(\mathbf{r}), -ik^2 \chi'_h(\mathbf{r}) E_h(\mathbf{r}), \\ 2k_{h,z} \frac{\partial}{\partial z} E_h(\mathbf{r}) &= -ik^2 (\chi_0 + \beta) E_h(\mathbf{r}) - 2(\mathbf{k}_{h,\perp} \cdot \nabla_{\perp}) E_h(\mathbf{r}) - ik^2 \chi'_h(\mathbf{r}) E_0(\mathbf{r}), \end{aligned} \quad (2.30)$$

where  $\nabla_{\perp} = [\partial/\partial x, \partial/\partial y, 0]$ .

Using the definition of the continuous Fourier transform given in Appendix A.2, we Fourier-

transform the Equations (2.30):

$$\begin{aligned}
\frac{\partial}{\partial z} \tilde{E}_0(s_x, s_y, z) &= \left[ \frac{-ik^2}{2k_{0,z}} \chi_0 - \frac{i2\pi}{k_{0,z}} \mathbf{s} \cdot \mathbf{k}_{0,\perp} \right] \tilde{E}_0(s_x, s_y, z) \\
&\quad - \frac{ik^2}{2k_{0,z}} F_{\perp} \{ \chi'_h(x, y, z) E_h(x, y, z) \} \\
\frac{\partial}{\partial z} \tilde{E}_h(s_x, s_y, z) &= \left[ \frac{-ik^2}{2k_{h,z}} (\chi_0 + \beta) - \frac{i2\pi}{k_{h,z}} \mathbf{s} \cdot \mathbf{k}_{0,\perp} \right] \tilde{E}_h(s_x, s_y, z) \\
&\quad - \frac{ik^2}{2k_{h,z}} F_{\perp} \{ \chi'_h(x, y, z) E_0(x, y, z) \}
\end{aligned} \tag{2.31}$$

where  $\mathbf{s} = [s_x, s_y, 0]$  are the full-period spatial frequencies. Here we have assumed that  $\chi_0$  is constant. We introduce the angles,  $\alpha_0$  and  $\alpha_h$  given by  $\mathbf{k}_0 \cdot \hat{\mathbf{z}} = |\mathbf{k}_0| \cos(\alpha_0)$  and  $\mathbf{k}_h \cdot \hat{\mathbf{z}} = |\mathbf{k}_h| \cos(\alpha_h)$  to give:

$$\begin{aligned}
\frac{\partial}{\partial z} \tilde{E}_0(s_x, s_y, z) &= \left[ \frac{-ik}{2 \cos(\alpha_0)} \chi_0 - \frac{i2\pi}{\cos(\alpha_0)} s_{0,\perp} \right] \tilde{E}_0(s_x, s_y, z) \\
&\quad - \frac{ik}{2 \cos(\alpha_0)} \mathcal{F}_{\perp} \{ \chi'_h(x, y, z) E_h(x, y, z) \} \\
\frac{\partial}{\partial z} \tilde{E}_h(s_x, s_y, z) &= \left[ \frac{-ik}{2 \cos(\alpha_h)} (\chi_0 + \beta) - \frac{i2\pi}{\cos(\alpha_h)} s_{h,\perp} \right] \tilde{E}_h(s_x, s_y, z) \\
&\quad - \frac{ik}{2 \cos(\alpha_h)} \mathcal{F}_{\perp} \{ \chi'_h(x, y, z) E_0(x, y, z) \}
\end{aligned} \tag{2.32}$$

where  $s_{0,\perp} = \mathbf{s} \cdot \mathbf{k}_{0,\perp} / k$  and  $s_{h,\perp} = \mathbf{s} \cdot \mathbf{k}_{h,\perp} / k$ .

For a perfect crystal, the functions  $\chi'_h$  and  $\chi''_h$  are constants, so the convolution terms become simple products giving a final simplification:

$$\begin{aligned}
&\frac{\partial}{\partial z} \begin{bmatrix} \tilde{E}_0(s_x, s_y, z) \\ \tilde{E}_h(s_x, s_y, z) \end{bmatrix} \\
&= \begin{bmatrix} \frac{-ik}{2 \cos(\alpha_0)} \chi_0 - \frac{i2\pi}{\cos(\alpha_0)} s_{0,\perp} & -\frac{ik}{2 \cos(\alpha_0)} \chi_h \\ -\frac{ik}{2 \cos(\alpha_h)} \chi_h & \frac{-ik}{2 \cos(\alpha_h)} (\chi_0 + \beta) - \frac{i2\pi}{\cos(\alpha_h)} s_{h,\perp} \end{bmatrix} \begin{bmatrix} \tilde{E}_0(s_x, s_y, z) \\ \tilde{E}_h(s_x, s_y, z) \end{bmatrix} \\
&= \begin{bmatrix} A_{00}(s_x, s_y) & A_{0h}(s_x, s_y) \\ A_{h0}(s_x, s_y) & A_{hh}(s_x, s_y) \end{bmatrix} \begin{bmatrix} \tilde{E}_0(s_x, s_y, z) \\ \tilde{E}_h(s_x, s_y, z) \end{bmatrix} \tag{2.33}
\end{aligned}$$

For any given frequency component, we have a system of 2 coupled linear homogeneous first order differential equations. The solution is found by first solving the eigenvalue problem and matching the initial condition. A numerical implementation of this, as well as the (finite and infinite) Bragg cases is given in

[https://github.com/Multiscale-imaging/dynamical\\_diffraction](https://github.com/Multiscale-imaging/dynamical_diffraction).

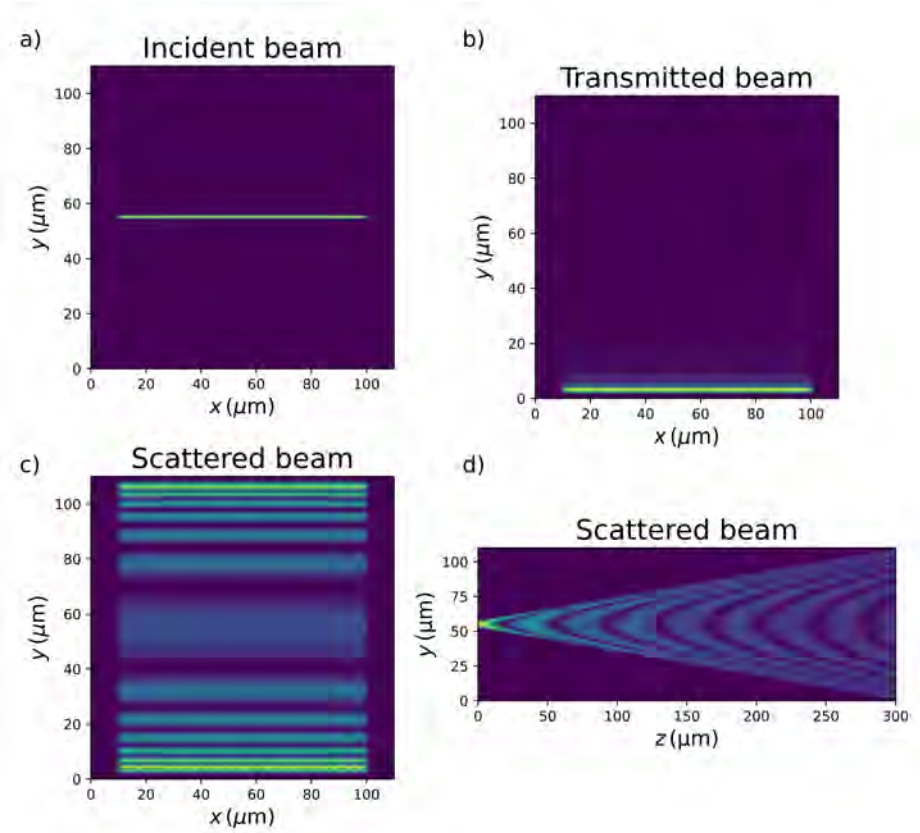


Figure 2.5: Line focused beam with a Gaussian profile propagated through a perfect crystal. a) Line focused beam on the entrance surface of the crystal. b) Transmitted beam on the exit surface of the crystal, c) Scattered beam on the exit surface. d) Depth profile of the scattered beam at  $x = 50 \mu\text{m}$ .

Figure 2.5 shows a simulation of a *section topography*[47] type experiment where a line-focused beam is incident on a perfect crystal using this propagator. The transmitted and scattered beams contain horizontal pendellösung fringes that are typical of section topography and DFXM of near-perfect crystals.

## 2.3 Kinematical scattering & geometric optics

For small crystals, and for very imperfect crystals, scattering can be treated in the kinematical approximation where we ignore refraction, absorption, and the back-scattering from the scattered wave into the direct wave. In this approximation the scattered beam is given by a simple integral over the volume of the crystal. Also, we can derive a relation between the direction of the scattered beam and the components of the displacement-gradient tensor. Usually the equations of kinematical diffraction are stated for the far-field diffraction patterns where the results can be written up in a short form using the three-dimensional continuous Fourier transform. Here we are interested the real space, near field diffraction pattern instead.

In the formalism of the Takagi-Taupin equations (eq. (2.15)), we can arrive at the kinematical equations by setting  $\chi_0 = 0$  and  $\chi_{\bar{h}} = 0$ :

$$\begin{aligned}
2i(\mathbf{k}_0 \cdot \nabla) E_0 &= 0 \\
2i(\mathbf{k}_h \cdot \nabla) E_h &= k^2 \beta E_h + k^2 C \chi'_h E_0
\end{aligned}
\tag{2.34}$$

The solution of the first equation is an interpolation of the boundary condition along the direction of  $\mathbf{k}_0$ . If the incident field is given on some plane  $\mathbf{k}_0 \cdot \mathbf{r} = 0$  may write for  $E_0$ :

$$E_0(\mathbf{r}) = E_{\text{init}}(\mathbf{r} - \hat{\mathbf{k}}_0 \cdot \mathbf{r}) \tag{2.35}$$

By introducing a coordinate,  $s_h$ , parallel to  $\mathbf{k}_h$ , we re-write the second equation as a ODE by inserting the solution of the first:

$$\frac{\partial}{\partial s_h} E_h = -ik/2\beta E_h - kC/2\chi'_h(\mathbf{r})E_0(\mathbf{r}) \tag{2.36}$$

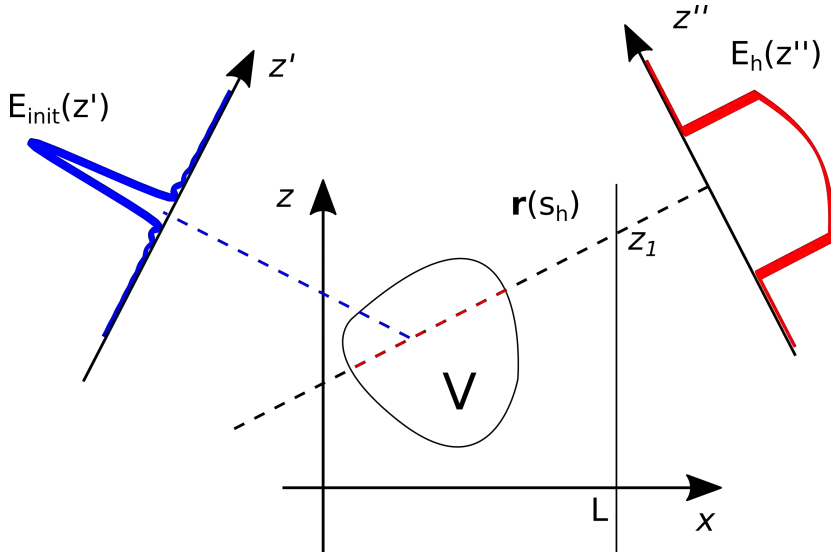


Figure 2.6: Geometry used in the derivations in section 2.3. The scattered amplitude at the point  $P$  depends only on an integral along the red part of the line  $\mathbf{r}(s_h)$ .

We now introduce a coordinate system with the  $z$ -axis parallel to the scattering vector and the scattering plane coinciding with the  $x$ - $z$  plane. We assume that the scattering crystal is confined to some finite volume,  $V$ , and we are interested in finding the scattered field at some point downstream of the sample  $P_1 = [L, y_1, z_1]^T$ . The scattered field at this point depends only on the scattering function a along the line:

$$\mathbf{r}(s_h) = s_h \begin{bmatrix} \cos \theta \\ 0 \\ \sin \theta \end{bmatrix} + \begin{bmatrix} 0 \\ y_1 \\ z_1 - L \tan \theta \end{bmatrix} \tag{2.37}$$

The incident field is everywhere equal to:

$$E_0(x, y, z) = E_{\text{init}}(\cos \theta z + \sin \theta x, y) \quad (2.38)$$

which gives us the expression for the scattered field:

$$\begin{aligned} E_h(x_1, y_1, L) &= E_{\text{exit}}(\cos \theta x_1 - \sin \theta L, y_1) \\ &= -ik/2\beta e^{ik\beta L/2} \int_{\mathbf{r}(s_h) \in V} e^{-ik\beta s_h/2} \chi'_h(\mathbf{r}(s_h)) E_0(\mathbf{r}(s_h)) d s_h \end{aligned} \quad (2.39)$$

where  $E_{\text{exit}}(x'', y'')$  is the scattered field downstream of the sample given on a pair of coordinates orthogonal to  $\mathbf{k}_h$ . The integral is only over the part of the line that falls within the sample.

We will go one step further and look at the contribution to this integral from a small sub volume of the sample  $\delta V$  of length  $a$  centered on the point  $P_1 = \mathbf{r}(s_h = b)$ .

In this small volume we approximate the value of the scattering function with its 1st order Taylor expansion:

$$\chi'_h(\mathbf{r}) = \chi_h e^{iQ(\nabla u_{31}x + \nabla u_{32}y + \nabla u_{33}z)} \quad (2.40)$$

where  $Q = |\mathbf{h}|$  and  $\nabla u_{3j}$  for  $j = 1, 2, 3$  is the gradient of  $\mathbf{u}(\mathbf{r}) \cdot \hat{\mathbf{z}}$ . For the incident field we write:

$$E_{\text{init}}(x', y') = |E_0| e^{ik(\zeta_v x' + \zeta_h y')} \quad (2.41)$$

where  $\zeta_x$  and  $\zeta_y$  are related to the phase gradient of the incident wave front and can be regarded as divergence angles in the  $x$  and  $y$  direction respectively.

We write out the integral, ignoring constant phase factors and get:

$$\begin{aligned} E_h(P_1) &\propto e^{iz_1(Q\nabla u_{33} + k \cos \theta \zeta_v)} e^{iy_1(Q\nabla u_{32} + k \zeta_h)} \\ &\times \int_{b-a/2}^{b+a/2} e^{is_h(-k\beta/2 + Q \cos \theta \nabla u_{31} + Q \sin \theta \nabla u_{33} + k \sin 2\theta \zeta_v)} d s_h \end{aligned} \quad (2.42)$$

If we choose the same form for the scattered wavefront as we did for the incident:

$$E_{\text{exit}}(x'', y'') = |E_h| e^{ik(\Delta 2\theta x'' + \psi y'')} \quad (2.43)$$

we can equate the three variables  $|E_h|$ ,  $\Delta 2\theta$ , and  $\psi$  with quantities from Eq. (2.42):

$$\begin{aligned} \Delta 2\theta &= 2 \tan \theta \nabla u_{33} + \zeta_v \\ \psi &= \zeta_h + 2 \sin \theta \nabla u_{32} \\ |E_h| &= \left| \int_{b-a/2}^{b+a/2} e^{is_h(-k\beta/2 + Q \cos \theta \nabla u_{31} + Q \sin \theta \nabla u_{33} + k \sin 2\theta \zeta_v)} d s_h \right| \end{aligned} \quad (2.44)$$

where we have substituted in  $Q = 2 \sin \theta k$  and applied some trigonometric identities. In the limit of  $a \rightarrow \infty$ , the integral on the last line will only be non-zero when the argument of the exponential function is zero. Writing out this condition yields:

$$\mu = \nabla u_{31} + \zeta_v + \tan \theta \nabla u_{33} \quad (2.45)$$

where we have substituted in the expression for  $\beta$ . The linear system of three equations given by the first two equations of (2.44) and Eq. (2.45) taken together relate the divergence angles of the incident and scattered light with the rocking angle of the sample and components of the strain tensor. These equations are of central importance for interpreting DFXM data. They are the same set of equations as the ones arrived at by Poulsen et al.[59] (repeated as Eq. 3.21 of this thesis) using geometric optics in the case of  $\delta E = 0$  and  $\chi = 0$ .

The purpose of this derivation is to establish the relationships between the phase gradients of the scattered beam ( $\Delta 2\theta$  and  $\psi$ ) and the strain of the sample crystal that are used when we interpret the phase-data from the experiments in Chapter 7. Secondly, it shows that the wave optics theory of Bragg scattering pursued in this chapter reaches the same conclusions as the traditional ray-optics treatment.

The derivation here also illustrates under what conditions the ray-optics treatment is appropriate. We first introduce a small sub-volume of the sample, where we assume that the strain and orientation of the lattice is constant. Second, we impose the rules of Bragg-scattering by an infinite lattice, by taking the limit  $a \rightarrow \infty$ , on this small volume. We interpret this as follows: there are two very different length scales in the system. One small, on the order of many unit cells of the crystal lattice, where diffraction takes place. And a long length scale, suitably much larger than the other, on where the structure of the sample varies. It is clear that this separation of length scales does not hold at the edges of a crystal and close to cores of crystal defects, where the structure varies on the scale of a few unit cells.

The last approximation we need to make to arrive at geometric optics is that the scattering from all these sub-volumes does not give rise to interference, but adds together incoherently. Typically, this behavior is ensured by a small coherence length of the incident illumination. But in the case of a DFXM, the small volume from which scattered light can interfere is also guaranteed by the small finite point-spread of the microscope optics.



# 3 Dark-Field X-ray Microscopy with twinned crystals

Dark-field x-ray microscopy[66, 59] is an x-ray scattering-imaging method in the vein of x-ray topography[7, 47] characterized by the use of an x-ray objective lens placed in the Bragg-scattered beam of a sample crystal to create a real-space image on an x-ray detector. The objective lens brings with it a number of advantages compared to conventional x-ray topographic imaging:

- The optical magnification of the sample – x-ray lens– detector configuration allows better resolution better than the point spread of the detector. (In the experiments presented here typically around  $\times 15$ )
- In topography, the necessary finite distance between sample and detector means that x-rays scattered in different directions will diffuse before they reach the detector. This problem is avoided by measuring exactly in the image plane, which allows one to study more disordered crystals than what is possible with x-ray topography.
- The small angular acceptance of the objective lens means that x-rays scattered from parts of the sample that are not on the optical axis of the objective lens do not reach the detector. This allows one to study single grains inside poly-crystals without overlapping intensity scattered from other grains.
- The long working distance of the applied lenses leave a lot of room for sample environments. ( $\approx 1$  m for the condenser- and  $\approx 30$  cm for the objective lens)
- The direction of the scattered beam, and therefore the strain-rotation field of the sample crystal, can be measured directly thanks to the small numerical aperture of the objective lens.

DFXM has clear similarities with dark-field transmission electron microscopy (DF-TEM) which also generates real space images of Bragg-reflected radiation. The parallel however has certain limitations. In DF-TEM images are generated using many simultaneous reflections. In DFXM images, only a single reflection is measured at one time and measuring several reflections from the same sample requires essentially a separate experiment to be carried out for each reflection. This difference owes to the much higher  $k$ -space resolution of x-ray scattering compared to electron scattering in usual experimental settings.

In this chapter we derive the usual theory of DFXM based on geometric optics and show how this quantitative theory can be used to analyze experimental data from crystals with pseudomerohedral twinning. The experimental geometry and typical length-scales given here correspond to the ID06-HXM instrument at the ESRF where the experiments for this thesis were carried out.

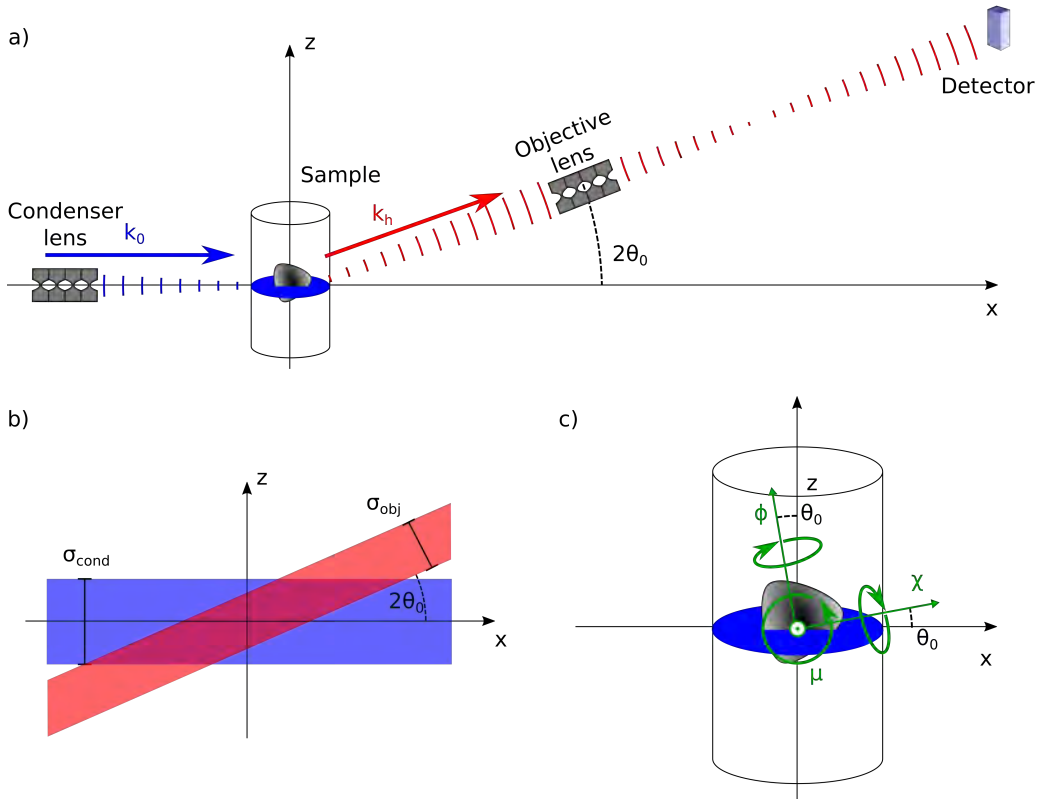


Figure 3.1: a) Sketch of the experimental geometry of the DFXM instrument as ID06-HXM at the ESRF in laboratory coordinates. b) Sketch of the imaging point-spread. c) Designation of the three assumed rotations used in this chapter. The laboratory  $y$ -axis points into the paper.

### 3.1 The geometry of a DFXM instrument

Figure 3.1 a) shows the experimental geometry of a DFXM instrument with the most important components and with directions denoted in laboratory coordinates. A monochromatic and collimated x-ray beam is incident from the left hand side parallel to the laboratory  $x$ -axis.  $z$  is the vertical direction. We operate in a geometry where the scattering plane is vertical, coinciding with the  $x$ - $z$  plane in laboratory coordinates. The four most important components are:

- **The condenser lens:** A 1D focusing lens used to shape the incident light into a flat sheet beam of a small thickness  $\sigma_{\text{cond}}$  in the  $z$  direction and a large extent in the  $y$  direction. The condenser lens is optional and is only used when doing experiments in the *slicing* mode.
- **The sample crystal:** The sample is mounted on a number of rotations stages called  $\mu$ ,  $\chi$ , and  $\phi$ . The sample is oriented such that the lattice (or the lattice of the grain of interest) is aligned to the Bragg condition with scattering in a vertical plane when all rotation stages are set to zero. In practice this alignment is done using these same rotation stages, so their position is not exactly zero and their axes of rotation are not exactly those drawn in Fig. 3.1 c), but we will use these symbols to denote small rotations equivalent to those plotted here. The  $\mu$  rotations, which is the same as the  $\mu$  used in the previous chapter, is called the rocking rotation.  $\chi$  is called the rolling rotation.
- **The objective lens:** A 2D imaging lens placed on the center of the scattered beam at a distance from both the sample and the detector such that a magnified image of the sample is created on the detector.
- **The detector:** A 2D image detector with a small pixel size. In our experiments the detector is mounted vertically as drawn on the figure and not orthogonal to the scattered beam. The combined effect of the lens and the detector gives an effective incoherent point spread of width  $\sigma_{\text{obj}}$ .

We define a number of vectors and write them in the laboratory coordinates:

$$\mathbf{k}_0 = k \begin{bmatrix} 1 \\ 0 \\ 0 \end{bmatrix} \text{ and } \mathbf{k}_h = k \begin{bmatrix} \cos(2\theta_0) \\ 0 \\ \sin(2\theta_0) \end{bmatrix} \text{ and } \mathbf{Q}_0 = 2 \sin(\theta_0)k \begin{bmatrix} -\sin(\theta_0) \\ 0 \\ \cos(\theta_0) \end{bmatrix} \quad (3.1)$$

where  $\theta_0$  is chosen such that  $\mathbf{Q}_0$  is exactly a reciprocal lattice vector of the sample crystal.  $\mathbf{Q}_0 = \mathbf{h}$  The line connecting the center of the sample (which we choose to be the origin of the coordinate system) with the objective lens and the detector is called the optical axis and is parallel to the vector  $\mathbf{k}_h$ .

DFXM operates both in a *projection*- and a *slicing*- mode depending on whether or not a 1D condenser lens is inserted in the beam. In the projection mode, without the condenser lens, the image on the detector is a projection of the sample along the direction of  $\mathbf{k}_h$ . In the slicing mode, only a thin slice of the sample centered on  $z = 0$  is illuminated. This means that the signal on a single detector pixel stems only from a small 3D volume inside the bulk of the sample with a size determined only by the performance of the optical components and the detector. Figure 3.1b) shows the point-spread of this configuration.

The condenser lens focuses the incident light onto a slice of width  $\sigma_{\text{cond}}$ . The point spread of the combination of x-ray optics and the detector defines a cylinder parallel to the optical axis. The intersection of these two volumes defines the point-spread of a given pixel. Typically the point spread of the condenser lens is larger than that of the imaging optics and the scattering angle  $2\theta_0$  is close to  $20^\circ$ . This means the microscope has better spatial resolution in the two directions normal to the scattered beam than in the parallel direction.

### 3.1.1 Sample alignment – the U matrix

The DFXM experiment is in essence a single-crystal diffraction experiment. Even if the sample may be a poly-crystal, only a single crystalline grain is studied at one time. As in any other single-crystal diffraction experiment the first step is to determine the orientation of the crystal lattice. The three basis vectors of the crystal lattice,  $\mathbf{a}$ ,  $\mathbf{b}$ ,  $\mathbf{c}$ , can be written in the laboratory coordinates and are stacked together into a matrix:

$$UA = [\mathbf{a}, \mathbf{b}, \mathbf{c}] \quad (3.2)$$

called the lattice matrix. This is a non-singular real 3-by-3 matrix. In general this matrix will not have any obvious symmetric structure (e.g. it will not be diagonal for a cubic lattice). The symmetric structure only appears when we write up the lattice matrix in a special coordinate system, where the axes of the coordinate system are aligned with high-symmetry directions of the lattice. We call this matrix the reference lattice matrix,  $A$ . It is related to the laboratory lattice matrix by the rotation that carries this special coordinate system into the laboratory system, which is the rotation given by the matrix  $U$ , a real rotation matrix.

A rotation matrix has three degrees of freedom that must be determined. In a DFXM experiment we always know the orientation of the measured scattering vector and its corresponding  $hkl$  indexes, which gives two constraints. This leaves one last degree of freedom to be determined – the rotation of the lattice about  $\mathbf{Q}$  – before we can uniquely specify  $U$ . In single-crystal diffraction experiments, you would typically measure one other reflection of the crystal lattice which gives two more constraints and leaves the problem over-determined. But due to the short travel range of some of the motors and due to the small detectors used in DFXM, a measurement of a second Bragg-reflection is not always easy.

When measuring single crystals, we often use a polished surface of the sample as the second direction to determine the orientation. This has to be done already in the mounting of the sample by the following procedure:

1. The sample is mounted on the goniometer head with the flat surface orthogonal to the incident beam ( $\mathbf{n} \parallel \mathbf{x}$ ) and the reciprocal lattice vector of interest somewhere in the  $x$ - $z$  plane. An alignment error of up to a few degrees of the sample crystal should be expected.
2. The sample is rotated using two orthogonal rotations  $\mu$  and  $\phi$  to make the surface horizontal to a high precision. This is achieved by inspecting the transmission image of the sample in the nearfield detector.
3. The sample is rotated again using only the  $\mu$  rotation to bring the  $\mathbf{Q}$  vector into the Bragg condition, such that a scattered beam is seen on a near-field detector. As  $\mu$  is the lowest of the rotation stages this keeps the surface normal in the  $x$ - $z$  plane.

4. The diffraction peak is brought into the vertical direction ( $\mathbf{Q} \cdot \hat{\mathbf{y}} = 0$ ) using small movements of  $\mu$  and the third orthogonal rotation,  $\chi$ .

After this procedure, both the vectors  $\mathbf{Q}$  and  $\mathbf{n}$  can be determined. The surface normal was vertical after Step 2 in the alignment procedure, so the orientation of the surface normal is given by the difference in the goniometer orientation between Step 2 and the final alignment:

$$\hat{\mathbf{n}} = \mathbf{R}_4 \mathbf{R}_2^T \hat{\mathbf{z}} \quad (3.3)$$

where  $\mathbf{R}_4$  and  $\mathbf{R}_2$  are the rotation matrices describing the goniometer setting after step 2 and step 4 respectively.

If the sample was mounted exactly and there is no mis-cut orientation of the polished surface, then we wouldn't have to use the  $\chi$  and  $\phi$  rotations for the final alignment step and we would be sure that  $\hat{\mathbf{n}}$  still lies within the  $(x, z)$  plane in the final orientation. In that case,  $\hat{\mathbf{n}}$  can be determined purely from the relative angle between  $\mathbf{Q}_0$  and  $\hat{\mathbf{n}}$  which can be calculated from their  $hkl$  indices. This assumption is used in the experiments presented here in this chapter.

Under this approximation, and if the probed reciprocal lattice vector is orthogonal to the polished surface (symmetric Laue geometry), the real rotation motors of the instrument correspond to the rotations drawn in Fig. 3.1c). If the sample was aligned by another procedure, we should not expect the rotation axes of the motors to be aligned with any specific direction and we fall back to using rotation matrices.

When the two vectors  $\mathbf{Q}_0$  and  $\hat{\mathbf{n}}$  and their  $hkl$  indices  $\mathbf{Q}_{hkl}$  and  $\mathbf{n}_{hkl}$  are known, the  $U$  matrix is build in the following way: [10]

1. Calculate the normalized  $\mathbf{Q}$  in both frames:  $\hat{\mathbf{Q}} = \mathbf{Q}/|\mathbf{Q}|$ , and  $\hat{\mathbf{Q}}_{\text{ref}} = \mathbf{B}\mathbf{Q}_{hkl}/|\mathbf{B}\mathbf{Q}_{hkl}|$
2. Calculate and normalize the component of  $\mathbf{n}$  that is normal to  $\mathbf{Q}$  in both frames:  $\mathbf{n}_{\perp} = \hat{\mathbf{n}} - (\hat{\mathbf{n}} \cdot \hat{\mathbf{Q}})\hat{\mathbf{Q}}$ ,  $\hat{\mathbf{n}}_{\perp} = \mathbf{n}_{\perp}/|\mathbf{n}_{\perp}|$  and similar for  $\mathbf{n}_{\text{ref}} = \mathbf{B}\mathbf{n}_{hkl}$ .
3. A third orthogonal direction is constructed as  $\hat{\mathbf{o}} = \hat{\mathbf{Q}} \times \hat{\mathbf{n}}_{\perp}$  in both frames.
4.  $U$  is calculated as:  $U = [\hat{\mathbf{Q}}, \hat{\mathbf{n}}_{\perp}, \hat{\mathbf{o}}][\hat{\mathbf{Q}}_{\text{ref}}, \hat{\mathbf{n}}_{\perp, \text{ref}}, \hat{\mathbf{o}}_{\text{ref}}]^T$

Where "×" denotes the cross-product of 3-vectors and  $\mathbf{B} = 2\pi\mathbf{A}^{-T}$ .

### 3.1.2 Reciprocal space map measurements

During a DFXM experiment, we typically also perform a traditional far-field diffraction measurement which we call a reciprocal space map (RSM). The purpose of this measurement is to characterize the mosaic spread of the crystal or grain of interest prior to performing the DFXM measurements.

Thanks to the long sample-to-detector distance, the small pixel-size of the available microscopy detectors, and the highly coherent x-ray source, this measurement has extremely high resolution in reciprocal space.<sup>1</sup> For the RSM measurement, the sample is placed in the direct beam. The extent of the beam is limited by a slit upstream of the sample. Typical dimensions are 200  $\mu\text{m}$  in the vertical direction and 500  $\mu\text{m}$  in the horizontal.

<sup>1</sup>Probably limited by the energy bandwidth in one direction and – since the EBS upgrade – by mechanical instability of the sample in the two orthogonal directions.

We could also choose to use the condenser lens while measuring the diffraction peak. In that case, we would illuminate the same volume as in the DFXM experiment but this however blurs out the diffraction features in the  $x$  direction. Furthermore, the RSM can be seen as a pre-characterization of the whole sample before microscopy both to identify the extent of the scattering in reciprocal space to be sure that the DFXM measurements cover the whole mosaic spread, but also to make sure that the region chosen for microscopy is representative of the sample as a whole. Therefore, we usually omit the condenser lens for RSM measurements.

Typically, the spatial extent of the sample is small compared to the width of the scattered beam at 5 m distance.<sup>2</sup> In this case we can treat each detector pixel as a point-measurement in reciprocal space. For a given pixel, we know its physical position in space  $\mathbf{P}(x, y) = [x_{\text{det}}, y, z]^T$ , where  $x_{\text{det}}$  is the position of the detector along the laboratory  $x$  axis and the origin is the position of the sample. The wave vector of the scattered beam is parallel to  $\mathbf{P}$  and has magnitude  $k$  so the scattering vector probed by this pixel,  $\mathbf{Q}(z, y)$ , is given by:

$$\mathbf{Q}(z, y) = \mathbf{k}'_h(z, y) - \mathbf{k}_0 = k(\mathbf{P}(z, y)/|\mathbf{P}(z, y)| - \hat{\mathbf{x}}) \quad (3.4)$$

The detector-coordinates  $y$  and  $z$  thus map out a section of a sphere in reciprocal space. To access different parts of reciprocal space, we rotate the sample around the laboratory  $y$  axis using the  $\mu$  rotation stage by a small angle,  $-\mu$ . We choose to artificially view this small rotation as a rotation of the entire experiment about a fixed sample in the opposite sense. In this picture, the scattering vector for each measured point becomes:

$$\mathbf{Q}(z, y, \mu) = k\mathbf{R}_y(\mu)(\mathbf{P}(z, y)/|\mathbf{P}(z, y)| - \hat{\mathbf{x}}) \quad (3.5)$$

where  $\mathbf{R}_y(\mu)$  is a rotation by the angle  $\mu$  about the laboratory  $y$  axis. In practice we measure at a number of different  $\mu$  values, using a 2D image detector, to get a 3D grid of data points in  $(z, y, \mu)$ -space. This corresponds to a curved grid in  $Q$  space, but to a good approximation, we can linearize Eq. (3.5) around the central point,  $(z, y, \mu) = (z_{\text{det}}, 0, 0)$ , where  $z_{\text{det}}$  is the coordinate of the center of the detector:

$$\begin{aligned} \mathbf{Q}(z, y, \mu) = \mathbf{Q}_0 + k \cos 2\theta_0 \begin{bmatrix} -\sin 2\theta_0 \\ 0 \\ \cos 2\theta_0 \end{bmatrix} (z - z_{\text{det}})/|P_0| + k \begin{bmatrix} 0 \\ 1 \\ 0 \end{bmatrix} y/|P_0| \\ + 2 \sin \theta_0 k \begin{bmatrix} \cos \theta_0 \\ 0 \\ \sin \theta_0 \end{bmatrix} \mu \quad (3.6) \end{aligned}$$

where  $|P_0| = \sqrt{x_{\text{det}}^2 + z_{\text{det}}^2}$  and  $z' = z - z_{\text{det}}$ . The quantities  $(z - z_{\text{det}})/|P_0|$  and  $(z - z_{\text{det}})/|P_0|$  can be thought of as small deflection angles of the scattered beam, equivalent to  $\Delta 2\theta$  and  $\psi$  of Eq. (2.43).

In this linear approximation, the three measured variables  $(z, y, \mu)$  map out a regular grid in  $\mathbf{Q}$ -space. But, as noted in [59], the three directions that define this grid (given by the three column vectors in Eq. (3.6)) are non-orthogonal. In the data-analysis presented

<sup>2</sup>For near-perfect single crystals this is not the case and the analysis here should be used with caution.

here, we fall back to the non-linear relations in Eq. (3.5) and use a 3D histogram approach to transform the data set into an orthogonal grid in reciprocal space.

### 3.1.3 Coordinate systems for reciprocal space information

The laboratory coordinate system is not ideal for plotting RSM data because the directions along the scattering vector is not one of the axes of the coordinate system. Rather,  $\mathbf{Q}_0$  is parallel to  $[-\sin\theta_0, 0, \cos\theta_0]^T$ . (See Fig. 3.1) The normal choice in the DFXM literature[59, 57, 58] is therefore to plot reciprocal space data in a different coordinate-system which is rotated by  $\theta_0$  about the  $y$ -axis relative to the laboratory coordinate system.<sup>3</sup> Furthermore, the measured  $\mathbf{Q}$  is normalized by  $|\mathbf{Q}_0|$  to yield dimensionless coordinates that are directly equivalent to angles measured in radians and to components of the displacement-gradient tensor. The three directions in reciprocal space in this coordinate system are given special names: The coordinate along the scattering vector is called *q-parallel* ( $q_{||}$ ), the component perpendicular to the scattering plane is called either *q-perpendicular* or *q-roll* ( $q_{\perp}$  or  $q_{roll}$ ) and the third orthogonal direction is called *q-rock* ( $q_{rock}$ )

$$\begin{bmatrix} q_{rock} \\ q_{\perp} \\ q_{||} \end{bmatrix} = R_y(\theta_0) \frac{\mathbf{Q} - \mathbf{Q}_0}{\mathbf{Q}_0} \quad (3.7)$$

For some phenomena such as twinning, it is convenient to represent the reciprocal space information in the  $hkl$ -basis of the crystal lattice.[33] The  $\mathbf{Q}$ -vector corresponding to a given  $(hkl)$  is given by  $\mathbf{Q} = \mathbf{UB}[h, k, \ell]^T$ , where  $\mathbf{UB} = 2\pi(\mathbf{UA})^{-T}$ . This implies the opposite relation between a measured  $\mathbf{Q}$  and a set of non-integer  $hkl$  values:

$$\begin{bmatrix} h \\ k \\ \ell \end{bmatrix} = (\mathbf{UB})^{-1} \mathbf{Q} \quad (3.8)$$

Finally, it is also quite common[66, 2, 68] to plot reciprocal space information as a function of the measured angles:

$$\begin{bmatrix} 2\theta = \arctan\left(\sqrt{z^2 + y^2}/x_{det}\right) \\ \mu \\ \eta = \arctan(y/z) \end{bmatrix} \quad (3.9)$$

which as shown before corresponds to a non-orthogonal frame in reciprocal space.

### 3.1.4 Reciprocal space geometry of DFXM

In a DFXM experiment, the probed volume of reciprocal space is given by the position of the objective lens and the orientation of the sample. We operate with two sample rotations: The rocking rotation,  $\mu$ , and the rolling rotation,  $\chi$ .

The small finite aperture ( $\approx 0.2$  mm) of the objective lens acts as a filter in reciprocal space so that we only sample a small part of the angular spectrum of the scattered beam. The position of the objective lens is given by the vector  $[\text{obx}, 0, \text{obz}]^T$ . In the slicing mode of DFXM we measure a real-space image of a slice of the sample near the  $(x, y, 0)$ -plane.

<sup>3</sup>This only holds in the *vertical* geometry where the scattering plane is orthogonal to the laboratory  $y$ . The existing literature is more thorough and also handles the *oblique* case.[59]

We find the  $\mathbf{Q}$  vector of a given pixel in the sample plane by looking at the vector that connects said pixel to the center of the objective lens:

$$\mathbf{D}(\Delta 2\theta; x, y) = \begin{bmatrix} \text{obx}(\Delta 2\theta) - x \\ y \\ \text{obz}(\Delta 2\theta) \end{bmatrix} \quad (3.10)$$

We write the distance vector  $\mathbf{D}$  as a function of  $\Delta 2\theta$  because  $2\theta$  scans are implemented by moving the objective lens along a direction orthogonal to  $\mathbf{D}$ , such that:

$$\text{obx} = \text{obx}_0 - \sin 2\theta_0 |\mathbf{D}_0| \Delta 2\theta \quad (3.11)$$

and

$$\text{obz} = \text{obz}_0 + \cos 2\theta_0 |\mathbf{D}_0| \Delta 2\theta \quad (3.12)$$

where  $\text{obx}_0$  and  $\text{obz}_0$  denote the reference position where the lens is centered on the scattered beam and  $\mathbf{D}_0 = \mathbf{D}(0; 0, 0)$ . In practice the objective lens is also rotated by the angle  $\Delta 2\theta$  and the detector is translated to follow the image, but this is not important for the calculations here.

The  $\mathbf{Q}$ -vector corresponding to the ray passing through the center of the objective lens is then

$$\mathbf{Q}(\Delta 2\theta; x, y) = k \left( \frac{\mathbf{D}(\Delta 2\theta; x, y)}{|\mathbf{D}(\Delta 2\theta; x, y)|} - \hat{\mathbf{x}} \right) \quad (3.13)$$

When we rotate the crystal, we treat that as the opposite rotation of the entire experiment around a fixed sample and write:

$$\mathbf{Q}(\mu, \chi, \Delta 2\theta; x, y) = k \mathbf{R}_y(\mu) \mathbf{R}_{\text{roll}}(-\chi) \left( \frac{\mathbf{D}(2\theta; x, y)}{|\mathbf{D}(2\theta; x, y)|} - \hat{\mathbf{x}} \right) \quad (3.14)$$

where again  $\mathbf{R}_y(\mu)$  is a rotation about the  $y$  axis by the angle  $\phi$  and  $\mathbf{R}_{\text{roll}}(-\chi)$  about the direction  $[\cos \theta, 0, \sin \theta]^T$ . The  $(x, y)$ -dependence in the above expression gives a coupling between the real space coordinates and the reciprocal space information. For near-perfect crystals this geometric effect is important and data analysis uses this expression for calculations. Going forward in this chapter, we omit this geometric effect and only consider the center pixel,  $(x, y) = (0, 0)$ .

We observe that by varying the two angles  $\mu$  and  $\chi$  we can map out a section of a sphere centered on zero in reciprocal space and  $\Delta 2\theta$  changes the radius of this sphere. For practical purposes we can linearize Eq. (3.14) and will by doing so (Eq. (3.21)) find that the direction mapped out by  $\Delta 2\theta$  is not orthogonal to the one mapped by  $\mu$ .

### 3.1.5 The resolution function

The aperture of the objective lens is small ( $\text{NA} \approx 10^{-3}$ ) but still the lens accepts rays scattered in more than just a single direction, and we can no longer treat each measurement as a point measurement in reciprocal space. Rather, we are integrating over a small 3D volume of reciprocal space and we would like to determine the size and shape of this volume. To do so, we model the incident beam as a continuum of rays that each have a wave vector close to  $\mathbf{k}_0$ , parameterized by two divergence angles and an energy offset:

$$\mathbf{k}'_0 = R(\zeta_v, \zeta_h)\mathbf{k}_0(1 + \delta E/E) \quad (3.15)$$

where  $\delta E/E$  is the deviation of photon energy of a given ray relative to the average photon energy.  $R(\zeta_v, \zeta_h)$  is a rotation matrix about a small divergence angle where  $\zeta_v$  is the angle in the scattering plane and  $\zeta_h$  is the angle out of plane. In free-space, the rays propagate along a straight line and the intensity of x-rays in any given point is proportional to an integral over the distribution of rays,  $p(\zeta_v, \zeta_h, \delta E/E)$  times a delta-function constraining the integral to only rays that pass through the point of interest.

The real crystal lattice is a deformed version of the reference lattice. The deformation is characterized by the displacement field,  $\mathbf{u}(\mathbf{r})$ . If the displacement gradient is slowly varying, the sample will locally have approximate translational symmetries with a local lattice matrix:  $\mathbf{U}\mathbf{A} = (\mathcal{I} + \nabla\mathbf{u})\mathbf{U}\mathbf{A}_0$ , where  $\mathcal{I}$  is the 3-by-3 identity matrix.

This linear transformation of the real lattice implies a transformation of the reciprocal lattice by the inverse transpose of the same transformation matrix. By writing the inverse as a Neumann series and only keeping linear terms, we get an expression for the transformation on the reciprocal lattice:

$$(\mathcal{I} + \nabla\mathbf{u})^{-1} = \sum_{k=0}^{\infty} (-\nabla\mathbf{u})^k \approx \mathcal{I} - \nabla\mathbf{u} \quad (3.16)$$

Furthermore we may rotate the sample by the *rocking* and *rolling* rotations described in the previous subsection. This finally gives us an expression for the local scattering vector of the deformed lattice:

$$\mathbf{Q}'_h = R(\mu, \chi)(\mathcal{I} - \nabla\mathbf{u}^T)\mathbf{Q}_h \quad (3.17)$$

Following the rules of ray-tracing: if we consider some local region of the deformed crystal, then a given ray with wave vector  $\mathbf{k}'_0$  gives rise to a scattered ray of wave vector  $\mathbf{k}'_h$  if and only if the Bragg condition of the local deformed lattice is **exactly** fulfilled. That is to say:

$$|\mathbf{k}'_h| = |\mathbf{k}'_0 + \mathbf{Q}'_h| = |\mathbf{k}'_0| = k(1 + \Delta E/E) \quad (3.18)$$

We parameterize  $\mathbf{k}'_h$  in a similar way to  $\mathbf{k}'_0$  and fix its energy to that of the incident beam to ensure energy conservation:

$$\mathbf{k}'_h = R(\Delta 2\theta, \psi)\mathbf{k}_h(1 + \delta E/E) \quad (3.19)$$

where  $\Delta 2\theta$  is a rotation in the scattering plane and  $\psi$  is a rotation out of plane.

To proceed, we write up this vectorial equation in the coordinates implied by Eq. (3.7). These are the coordinates along the  $q_{\text{rock}}$ ,  $q_{\perp}$ , and  $q_{\parallel}$  directions in fig. 3.2. We include only linear terms in the rotation angles and the relative energy.

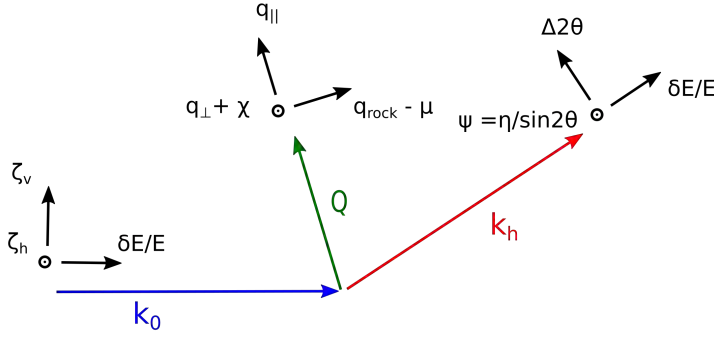


Figure 3.2: Reciprocal space geometry and parameters used in deriving expression for the resolution function.

$$\begin{aligned}
 k \begin{bmatrix} \cos \theta + \cos \theta \delta E/E + \sin \theta \zeta_v \\ \zeta_h \\ -\sin \theta - \sin \theta \delta E/E + \cos \theta \zeta_v \end{bmatrix} \\
 = |\mathbf{Q}| \begin{bmatrix} -(\nabla \mathbf{u})_{3,1} - \mu \\ -(\nabla \mathbf{u})_{3,2} - \chi \\ 1 - (\nabla \mathbf{u})_{3,3} \end{bmatrix} + k \begin{bmatrix} \cos \theta + \cos \theta \delta E/E + \sin \theta \Delta 2\theta \\ \psi \\ \sin \theta + \sin \theta \delta E/E + \cos \theta \Delta 2\theta \end{bmatrix} \quad (3.20)
 \end{aligned}$$

We simplify the above equations and introduce the angle  $\eta = \psi \sin 2\theta$ , which is the azimuthal angle of the scattered beam relative to the  $x-z$  plane, an angle which is commonly used in the existing literature.

$$\begin{aligned}
 -(\nabla \mathbf{u})_{3,1} &= \mu + \zeta_v/2 + \Delta 2\theta/2 \\
 -(\nabla \mathbf{u})_{3,2} &= -\chi - \cos \theta \eta + \zeta_h/(2 \sin \theta) \\
 -(\nabla \mathbf{u})_{3,3} &= \delta E/E + \cot \theta (-\zeta_v/2 + \Delta 2\theta/2)
 \end{aligned} \quad (3.21)$$

We identify that the three resolved components of the displacement gradient here are the components of the  $\mathbf{q}$ -vector of equation (3.7):  $q_{\text{rock}} = -(\nabla \mathbf{u})_{3,1}$ ,  $q_{\perp} = -(\nabla \mathbf{u})_{3,2}$  and  $q_{\parallel} = -(\nabla \mathbf{u})_{3,3}$ .

These equations relate the energy and divergence angle of a given incident ray to the angles of the scattered ray. For a specific ray (which means a fixed choice of  $\zeta_v$ ,  $\zeta_h$ , and  $\delta E/E$ ) and fixed sample angles this is a linear system of 3 equations with 2 variables ( $\Delta 2\theta$  and  $\eta$ ). The  $y$  equation is decoupled from the rest, so this means that for a given energy, only one specific vertical divergence angle will give rise to a scattered ray and vice versa. Eliminating  $\Delta 2\theta$  from the first and the last equation yields:

$$\delta E/E(\zeta_v) = \cot \theta (\zeta_v + q_{\text{rock}} - \phi) - q_{\parallel} \quad (3.22)$$

The divergence angles of the scattered rays can be written as:

$$\eta(\zeta_h) = \sec \theta (q_{\perp} + \chi + \zeta_h/(2 \sin \theta)) \quad (3.23)$$

and

$$\Delta 2\theta(\zeta_v) = 2\phi - 2q_{\text{rock}} - \zeta_v \quad (3.24)$$

We are now interested in predicting the intensity on the detector in a DFXM experiment stemming from the point  $\mathbf{r} = [0, 0, 0]^T$  in the sample. This intensity is proportional to an integral of the phase-space distribution of incident rays multiplied by a 1D Dirac delta function enforcing the Bragg-law and multiplied by the transmission of the imaging optics at the particular divergence angle of the corresponding scattered ray. The delta function is used to raise the energy integral, which yields:

$$I \propto \int \int p(\zeta_v, \zeta_h, \delta E/E(\zeta_v)) T(\Delta 2\theta(\zeta_v), \eta(\zeta_h)) d\zeta_v d\zeta_h \quad (3.25)$$

where  $p(\zeta_v, \zeta_h, \delta E/E)$  is phase space distribution function of the incident beam and  $T(\Delta 2\theta, \eta)$  is the transmission coefficient of the imaging optics at the given angle of the scattered ray, and  $\delta(\cdot)$  represents the Dirac-delta function.

The expression on the RHS of the Eq. (3.25) depends parametrically on the vector  $\mathbf{q}$ . Choosing to view it as a function of  $\mathbf{q}$  instead, we call this the resolution function:  $\text{Res}_q(\mathbf{q})$ . This function tells us what values of the local deformation tensor will give rise to a signal on the detector and how strongly. The position of this function in reciprocal space can be shifted by rotating the sample or by displacing the objective lens but its shape and size is unaffected in the small-angle approximation.

The evaluation of this function is only straight-forward for certain choices of  $p$  and  $T$  and therefore the evaluation has typically been done by numerical MC-integration.[57, 58] For this demonstration, we choose a pair of functions where the two integrals factorize and perform a simple 1D numerical integral for the  $x$ -integral and find an analytical solution for the  $y$ -integral. In Fig. 3.3 we compare two calculated resolution functions with measurements of single crystals and see that the theory agrees well with the measurements.

With these parameters (that should be applicable for most experiments performed at ID06-HXM) we find that the  $q_{\parallel}$  and  $q_{\perp}$  resolution is set by the NA of the objective lens, the  $q_{\text{rock}}$  resolution is given by the NA of the condenser lens. The bandwidth is small compared to the numerical apertures and only contributes a small blurring of the edges of the resolution function. In some other experiments, a set of slits is inserted in the beam before the condenser in which case the opening of this slit replaces the condenser lens aperture as the determining factor for the resolution in the  $q_{\text{rock}}$  direction.

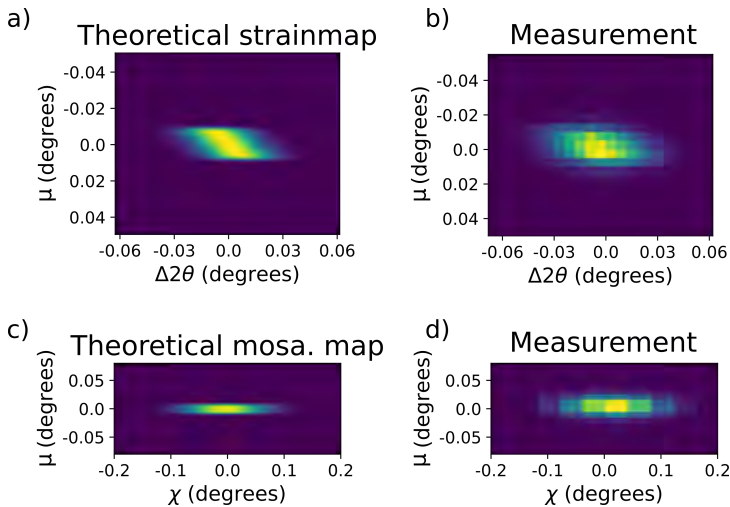


Figure 3.3: Calculated resolution functions compared with measurements of near-perfect single crystals. a) Calculated resolution function plotted as a function of  $\mu$  and  $\Delta 2\theta$ . b) Measured intensity in a DFXM experiment using a near-perfect single crystal. c) Calculated resolution function plotted as a function of  $\mu$  and  $\chi$ . d) Measured intensity in a DFXM experiment using a near-perfect single crystal.

### 3.1.6 Types of measurements

Often, it will be too time consuming to map out the diffraction pattern completely in 3D by scanning all three angles,  $(\mu, \chi, \Delta 2\theta)$  in a 3D grid. Instead we only measure on a 2D grid. The two most common measurements are:

1. **Mosaicity map:** When a sample has a relatively small amount of uniaxial strain, we can assume that the aperture of the lens always captures the diffracted peak in the  $q_{||}$ -direction. In that case we only need to vary the sample angles  $(\mu, \chi)$  to cover the entire diffraction peak. This measurement measures only the tilt of the lattice planes, not the  $d$ -spacing.
2. **Strain map:** The resolution function is wider in the  $\chi$  direction (equivalent to  $q_{\perp}$ ) than in the two other directions. It may therefore be appropriate in some cases to assume that the entire diffraction peak is covered in the  $q_{\perp}$ -direction. In this case, we vary only  $(\mu, \Delta 2\theta)$ . This measurement resolves the  $d$ -spacing (or equivalently the uniaxial strain) and the lattice plane orientation in the in-plane direction but not in the out-of-plane direction.

The mosaicity map is the easiest and most flexible of the two measurements as it is often the case that the diffraction peak has larger extent in the two transverse direction  $q_{rock}$  and  $q_{\perp}$  than in the parallel direction. The drawback is that the  $q_{||}$  direction is not resolved. This direction is special because it uniquely tells us about the strain in the sample and not pure rotations of the lattice. The strain map is more difficult to measure because it involves moving the objective lens which requires careful calibration of the geometric parameters and computational corrections in the data treatment to avoid registration errors in the measurements.

## 3.2 Twinned crystals

DFXM typically has an anisotropic spatial resolution of  $0.1 - 0.5 \mu\text{m}$  and reciprocal space resolution of around  $10^{-4}\text{rad}$ . DFXM is therefore particularly well suited studying crystalline materials containing structural twins of the kind commonly observed in ferroelectric materials as these contain variation on those length-scales. In this section we will introduce the concept of twinning and describe how twins affect the scattering pattern of twinned crystals and finally demonstrate how to analyze DFXM data from such crystals. We focus here on ferroelectrics, but the formalism is applicable to a wider range of twinned crystals.

We consider a ferroelectric crystal that stems from a cubic parent phase with lattice:

$$\mathbf{A}_c = \begin{bmatrix} a_c & 0 & 0 \\ 0 & a_c & 0 \\ 0 & 0 & a_c \end{bmatrix} \quad (3.26)$$

The ferroelectric crystal can be regarded as a strained version of the parent phase. The lattice matrix of the the ferroelectric phase can be written as:

$$\mathbf{A}_0 = (\mathcal{I} + \epsilon)\mathbf{A}_c \quad (3.27)$$

The strain tensor,  $\epsilon$ , has a lower symmetry than the cubic parent phase and there exists a number of symmetries, represented by matrices,  $\mathbf{P}_n$  for  $n = 1, 2, \dots$ , that are symmetries of the cubic phase but not of the ferroelectric. We can therefore generate a number of different *variants* of the ferroelectric phase, by applying the broken symmetries to the strain tensor:

$$\mathbf{A}_n = (\mathcal{I} + \mathbf{P}_n \epsilon \mathbf{P}_n^T) \mathbf{A}_c = \mathbf{P}_n \mathbf{A}_0 \mathbf{G}_n^T \quad (3.28)$$

where  $\mathbf{G}_n = \mathbf{A}_c^T \mathbf{P}_n \mathbf{A}_c^{-T}$ .<sup>4</sup>

These broken symmetries can be any of the  $90^\circ$  and  $120^\circ$  rotations that can also be written as (column-)permutations of the cubic lattice matrix. Since we are only interested in the lattice, we can ignore inversion and mirror symmetries. The number of different variants is the difference in order of the two symmetry groups.

In ferroelectrics, the symmetry breaking strain is also associated with a spontaneous polarization that breaks inversion symmetry. The inversion operation does not change the strain-tensor so two domains related by an inversion symmetry have opposite polarization but have the same lattice. The domain walls that connect such two domains are not governed by a rule of the type presented in this section and can form from a mechanical-compatibility point of view along any lattice orientation but electrical interactions favor a domain wall parallel to the spontaneous polarization. We say that such a domain wall is non-elastic and call it a  $180^\circ$  domain wall. In this chapter, we will only deal with elastic domains where the lattices are different.

<sup>4</sup>This expression also holds when the parent-phase is non-cubic. For cubic materials specifically we have  $\mathbf{G}_n = \mathbf{P}_n$ .

Two lattice matrices describe different variants, if their respective metric tensors ( $T = A^T A$ ) are different. The metric tensor is invariant to rotations of the lattice and two lattice matrices with the same metric tensor can always be rotated into each other.<sup>5</sup>

When a large crystal goes through a cubic to ferroelectric phase transition, the crystal doesn't choose one of these symmetry-equivalent lattices globally but rather different parts of the macroscopic crystal choose different lattice variants and the crystal becomes separated into domains with different lattices. The relative orientation of the lattices in adjacent domains is governed by *twin laws*. The macroscopic crystal is called a twinned crystal and the individual domains are called twins. The interfaces between domains are called domain boundaries or domain walls and typically form along planes parallel to specific crystallographic directions.[11]

The diffraction pattern of a twinned crystal consists of the overlapping diffraction patterns of the individual domains. For a given set of integers  $hkl$  there will now be a number of separated peaks, where the relative distance of separation  $\Delta \mathbf{Q}/|\mathbf{Q}|$  is of the same order of magnitude as the symmetry breaking strain. In powder-diffraction experiments, one only measures the magnitude of the scattering vector, not the direction. We can therefore determine the number of sub-peaks of a given reflection with the indices  $h, k, \ell$  using the equation:

$$|\mathbf{Q}_n| = \left| \mathbf{B}_n[h, k, \ell]^T \right| = 1/2\pi \left| \mathbf{A}_n^{-T}[h, k, \ell]^T \right| \quad (3.29)$$

for every  $n$ . The number of different values found are equal to the number of peaks observed in a powder-diffraction experiment (if the experiment has high enough resolution to resolve them). While a powder-diffraction experiment only measures the splitting in the  $q_{||}$ -direction, DFXM also measure the splitting in the two perpendicular directions. The peak splitting in the  $q_{\perp}$  and  $q_{rock}$  directions, is more complicated to calculate as it also requires the knowledge of the relative orientation of the lattices in different domains.

### 3.2.1 Elastically compatible domain walls

When the crystal undergoes the transition from cubic to ferroelectric, the single crystal is split in a number of domains: regions with different lattice variants and different orientation of the lattices. The interfaces between these domains form along straight planes that correspond to special crystallographic planes.

By requiring that the lattices of both domains are connected along the domain wall, we can write equations that allow us determine the specific planes where domain walls can form. Doing so we will find that the lattices are slightly rotated from one side of the domain wall to the other. As a result of this, there can be more differently oriented domains in a twinned crystal than the number of symmetry related domain variants.

The combination of the symmetry lowering strain and the rotation associated with a given domain wall,  $w$ , can be written as a single linear transformation:  $S_w$ . If the domain wall connects two adjacent domains (a) and (b), we can write:

$$[\mathbf{a}_{(b)}, \mathbf{b}_{(b)}, \mathbf{c}_{(b)}] = S_w [\mathbf{a}_{(a)}, \mathbf{b}_{(a)}, \mathbf{c}_{(a)}] \quad (3.30)$$

---

<sup>5</sup> $A_1 = (A_1 A_2^{-1}) A_2$  and  $(A_1 A_2^{-1})$  is unitary because  $(A_1 A_2^{-1}) (A_1 A_2^{-1})^T = A_1 T_2^{-1} A_1^T = A_1^{-T} T_1 T_2^{-1} A_1^T = \mathcal{I}$

where the subscripts refer to specific domains and not to the domain variant. This further implies a transformation of the reciprocal lattices by the matrix  $\mathbf{S}_w^{-T}$  according a scaling property of the Fourier transform. We can use these transformation matrices to calculate the splitting of a given reciprocal lattice vector. In  $hkl$ -space we can write this splitting as:

$$\Delta \mathbf{h}_w = (\mathbf{S}_w^{-T} - \mathcal{I}) [h, k, \ell]^T$$

An important general rule is that the splitting of a diffraction peak  $\Delta \mathbf{h}_w$  associated with a given domain wall is parallel to the domain wall normal  $\mathbf{n}_w$ . [33] The calculation of these transformation matrices and of the domain wall normals is the subject of an extensive literature. [29, 62, 24, 33]

The domain walls are found by requiring that the lattices of two adjacent domains are connected along the domain wall. This means that for any two points on the domain wall, the vector that connects these two points,  $\mathbf{r}$ , is simultaneously a lattice vector of both the two lattices with the same lattice coordinates  $\xi$ . As a consequence of this, the vector must have the same length, whether it is given by one lattice or the other, which we can write as an equation:

$$\xi \mathbf{T}_{(a)} \xi^T = \xi \mathbf{T}_{(b)} \xi^T \quad (3.31)$$

for any  $\xi$  on the domain wall. In order for this to be true we must have:

$$\xi (\mathbf{T}_{(a)} - \mathbf{T}_{(b)}) \xi^T = \xi \Delta \mathbf{T} \xi^T = 0 \quad (3.32)$$

for all points on the domain wall. It turns out, that by solving the eigenvalue problem of  $\Delta \mathbf{T}$  and re-writing the above equation in a special coordinate system, the result will be the equation of a plane only under certain circumstances.

For any pair of two domain variants, we will find either 0, 1, or 2 allowed domain walls. The literature distinguishes between two types of domain walls:  $W$ -domain walls that form along specific high-symmetry directions of the lattice with integer  $hkl$  indices guaranteed by a symmetry of the low-symmetry phase [62] and  $S$ -domain walls that form along a general direction of the lattice determined by the magnitude of the symmetry-breaking strain.

We use a numerical implementation of the algorithm outlined in [33] to calculate domain walls and transformation matrices. To illustrate the method we will go through the simplest case, that of a tetragonal distortion of a cubic lattice in the subsection below.

### The tetragonal ferroelectric

A tetragonal distortion is given by the strain-tensor:

$$\epsilon = \begin{bmatrix} \frac{a}{a_c} - 1 & 0 & 0 \\ 0 & \frac{a}{a_c} - 1 & 0 \\ 0 & 0 & \frac{c}{a_c} - 1 \end{bmatrix} \quad (3.33)$$

and

$$\mathbf{A}_0 = \begin{bmatrix} a & 0 & 0 \\ 0 & a & 0 \\ 0 & 0 & c \end{bmatrix} \quad (3.34)$$

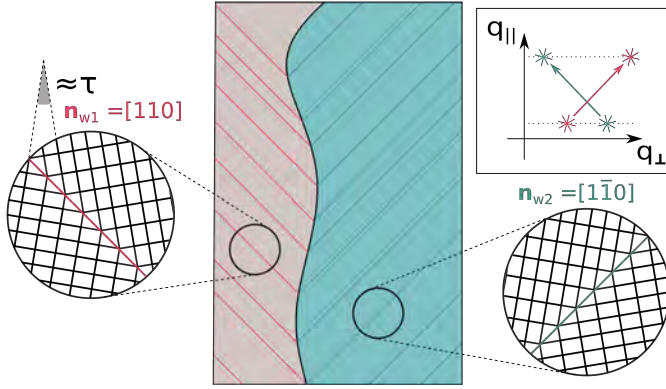


Figure 3.4: Sketch of a 2D view of a twinned tetragonal crystal with exaggerated symmetry breaking. The crystal is split in two super-domains, that each show stripes of domains separated by repeating domain walls of the same kind. The insert in the top right shows the splitting of a representative Bragg-peak.

The broken symmetries are any rotation that involves the 'c' axis. We only need to consider two, e.g:

$$P_1 = \begin{bmatrix} 0 & 0 & -1 \\ 0 & 1 & 0 \\ 1 & 0 & 0 \end{bmatrix} \text{ and } P_2 = \begin{bmatrix} 1 & 0 & 0 \\ 0 & 0 & -1 \\ 0 & 1 & 0 \end{bmatrix} \quad (3.35)$$

that generate the two other domain variants:

$$A_1 = \begin{bmatrix} c & 0 & 0 \\ 0 & a & 0 \\ 0 & 0 & a \end{bmatrix} \text{ and } A_2 = \begin{bmatrix} a & 0 & 0 \\ 0 & c & 0 \\ 0 & 0 & a \end{bmatrix} \quad (3.36)$$

applying the other permutations will give one of these three variants.

We now want to find the possible domain walls between the two domains  $A_1$  and  $A_2$ . Performing the calculation described in [33, 29] gives two compatible domain walls,  $w_1$  and  $w_2$  that form along the (110) and (1 $\bar{1}$ 0) directions respectively.

The linear transformations, that connect the lattices are:[33]

$$S_{w_1} = \begin{bmatrix} 1 & 0 & 0 \\ 0 & 1 - \tau & -\tau \\ 0 & \tau & 1 + \tau \end{bmatrix} \text{ and } S_{w_2} = \begin{bmatrix} 1 & 0 & 0 \\ 0 & 1 - \tau & \tau \\ 0 & -\tau & 1 + \tau \end{bmatrix} \quad (3.37)$$

where  $\tau = (c^2 - a^2)/(c^2 + a^2)$ . The transformation can be decomposed into an axial strain part and a small rotation by an angle of  $\arcsin(\tau)$ , commonly called 'the clapping angle'.

In many ferroelectrics, the domains form hierarchical structures of domains and super-domains. The simplest super-domain structure is the stripe domain, where large regions of the crystal consists of regular lamellar of flat domains connected by a single type of domain wall as is sketched in Fig. 3.4 and observed experimentally in Fig. 3.6. The relative orientation of such super-domains are governed by a higher order theory of elastic

compatibility which we will not pursue here.[77] The total number of sub-peaks in a split Bragg peak can be more than the number of domain-variants present in the crystal as is exemplified in the figure where only domains of two types are present, but they are rotated compared to each other to cause a shift of the scattering peak along the  $q_{\perp}$  direction resulting in four separate sub-peaks.

### 3.3 Experimental demonstration

In this section we demonstrate typical DFXM experiments with a focus on the quantitative analysis of coherent twin-walls. We will find that the quantitative theory outlined in this chapter gives good agreement with the experiments.

#### 3.3.1 Potassium Niobate (KNbO<sub>3</sub>)

##### Experimental information

The sample is a single-crystal of potassium niobate which is a ferroelectric in the pre-ovskite crystal structure that has an orthorhombic lattice at room temperature. The sample was made by top seeded solution growth, purchased from FEE GmbH (Devision of EOT, Idar Oberstein, Germany).

A square of size 4 mm × 4 mm was cut out along the  $[101]_{\text{p.c.}}$  and  $[10\bar{1}]_{\text{p.c.}}$  directions and polished down to a thickness of 300 μm. The polished surface is of orientation  $n = [010]_{\text{p.c.}}$ . The scattering experiments were carried out at the ID06-HXM instrument at the ESRF in June 2021.

##### RSM

In orthorhombic KNbO<sub>3</sub>, the conventional crystallographic unit cell is not a slightly deformed version of the cubic unit cell. Rather, a larger, orthorhombic unit cell, that contains two times the atoms of the cubic unit, is chosen. The orthorhombic unit cell that can be found in the literature[41] is:

$$\mathbf{A}_{\text{ortho}} = \begin{bmatrix} 5.697 & 0 & 0 \\ 0 & 3.971 & 0 \\ 0 & 0 & 5.721 \end{bmatrix} \text{ \AA} \quad (3.38)$$

The *pseudo cubic* unit cell is often chosen instead. The pseudocubic lattice vectors are  $\mathbf{a}_{\text{p.c.}} = \mathbf{U}\mathbf{A}_{\text{ortho}}[1/2, 0, 1/2]^T$ ,  $\mathbf{b}_{\text{p.c.}} = \mathbf{U}\mathbf{A}_{\text{ortho}}[0, 1, 0]^T$ , and  $\mathbf{c}_{\text{p.c.}} = \mathbf{U}\mathbf{A}_{\text{ortho}}[-1/2, 0, 1/2]^T$ . The standard, upper triangular, form of the pseudo cubic lattice can be found by calculating the QR-decomposition of the resulting lattice matrix and is:

$$\mathbf{A}_0 = \begin{bmatrix} 4.0369 & 0 & -0.01697 \\ 0 & 3.971 & 0 \\ 0 & 0 & 4.0368 \end{bmatrix} \text{ \AA} \quad (3.39)$$

This has the form of a monoclinic lattice, but it has two extra symmetries. We can also write the lattice matrix on a symmetric form where the symmetries are more evident:

$$\mathbf{A}_{0,\text{sym}} = \begin{bmatrix} a \cos \gamma & 0 & a \sin \gamma \\ 0 & b & 0 \\ a \sin \gamma & 0 & a \cos \gamma \end{bmatrix} \quad (3.40)$$

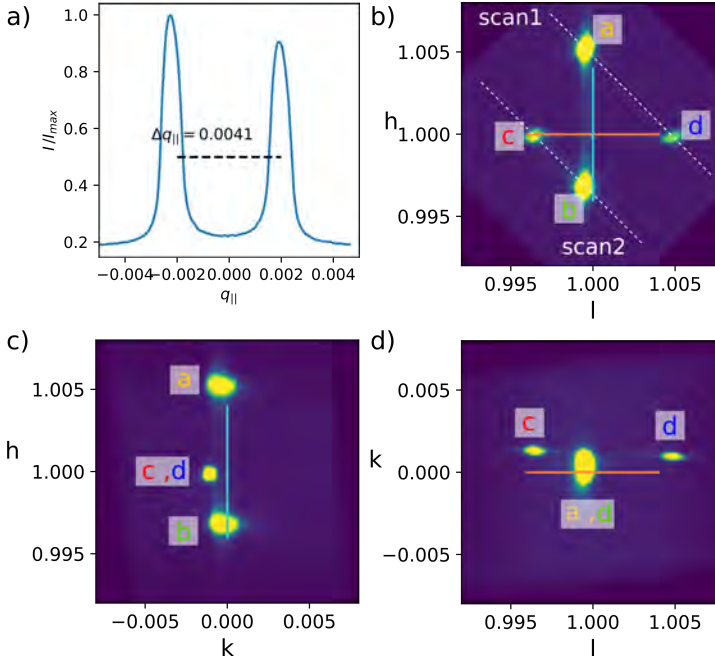


Figure 3.5: a) Integrated rocking curve as a function of  $q_{||}$  b-d) Three orthogonal projections of an RSM of  $\text{KNbO}_3$   $(101)_{pc}$  in the units of Eq (3.8). The cyan and orange lines mark the two calculated twin-laws. The white dashed lines mark planes of constant  $q_{||}$ . Because the splitting is along one of the primary directions of the lattice, each pair of peaks a,c and b,d appear as a single peak in one of the three projections.

with  $a = 4.037 \text{ \AA}$ ,  $b = 3.971 \text{ \AA}$  and  $\gamma = \pm 0.120^\circ$ .

This corresponds to a spontaneous strain of:

$$\epsilon = \begin{bmatrix} \frac{a}{a_c} \cos \gamma - 1 & 0 & \frac{a}{a_c} \sin \gamma \\ 0 & \frac{b}{a_c} - 1 & 0 \\ \frac{a}{a_c} \sin \gamma & 0 & \frac{a}{a_c} \cos \gamma - 1 \end{bmatrix} \quad (3.41)$$

This lattice retains only four rotational symmetries of the cubic lattice but loses the rest, so we find six (a fourth of the 24 rotational symmetries in the octahedral group) twin-variants.<sup>6</sup> With up to two domain walls per domain-variant pair, this gives an enormous number (up to 30) of possible domain walls. However in the sample at hand, we only observe two domain variants and two domain walls of the same type but different orientation.

We investigate the  $(101)_{p.c.}$  reflection and observe four separate sub-peaks that fall on two different  $2\theta$  shells in reciprocal space. We integrate the diffraction peak over the  $q_{\perp}$  and  $q_{rock}$  directions and look at the splitting along the  $q_{||}$ -direction in figure 3.5 a). The observed distance of 0.004 between these two peaks is only compatible with one pair of domain variants, namely the ones with unit cells given by:

<sup>6</sup>In the symmetric version: first pick the  $b$  axis out of three options and then choose the sign of the  $\gamma$  angle gives  $3 \times 2$  different versions.

$$\mathbf{A}_{0,\text{sym}} = \begin{bmatrix} 4.037 & 0 & -0.00849 \\ 0 & 3.971 & 0 \\ -0.00849 & 0 & 4.037 \end{bmatrix} \text{ \AA}$$

$$\text{and } \mathbf{A}_{1,\text{sym}} = \begin{bmatrix} 4.037 & 0 & 0.00849 \\ 0 & 3.971 & 0 \\ 0.00849 & 0 & 4.037 \end{bmatrix} \text{ \AA} \quad (3.42)$$

related to each other by the broken 4-fold rotational symmetry about the  $[010]_{\text{ortho}} = [010]_{\text{p.c.}}$  axis. This pair of domains therefore allows two domain walls with normals orthogonal to the axis of this rotation.[29] By performing the calculation described in [33] we find  $\mathbf{n}_{w_1} = (100)_{\text{p.c.}}$  and  $\mathbf{n}_{w_2} = (001)_{\text{p.c.}}$  respectively. These are consistent with the domain wall orientations found in tables.[62, 24] The transformation matrices are:

$$\mathbf{S}_{w_1} = \begin{bmatrix} 1 & 0 & 2 \sin 2\gamma \\ 0 & 1 & 0 \\ 0 & 0 & 1 \end{bmatrix} \text{ and } \mathbf{S}_{w_2} = \begin{bmatrix} 1 & 0 & 0 \\ 0 & 1 & 0 \\ 2 \sin 2\gamma & 0 & 1 \end{bmatrix} \quad (3.43)$$

The splittings of the  $[101]_{\text{p.c.}}$  are

$$\Delta \mathbf{h}_{w_1} = [0.0084, 0, 0] \text{ and } \Delta \mathbf{h}_{w_2} = [0, 0, 0.0084] \quad (3.44)$$

These are the distances marked with cyan and orange lines in figure 3.5 b-d) which corresponds well with the measured peak splitting.

The RSM in Fig. 3.5 shows weak streaks of intensity between the sub-peaks that are connected by domain walls. These streaks also extend to the other side of the individual peaks and appear to be symmetric around the peaks. This is expected for an infinitely sharp domain wall where the sharp cut-off would lead to  $1/q^2$ -intensity streaks<sup>7</sup> similar to the well-known truncation-rods in the scattering signals from thin crystals and crystal surfaces.

### DFXM

In a single image in a DFXM measurement, we only measure a small volume of reciprocal space, on the order of  $5 \cdot 10^{-4}$  along the narrowest directions, around one twentieth of the extent of the whole diffraction peak seen in Fig. 3.5. Therefore, covering the entire diffraction peak by a 3D grid scan would require more than about  $20^3$  scan points. However, we see that the sample only has prominent features in two distinct *shells* or reciprocal space. Therefore, we can cover the full diffraction peak by doing two mosaicity scans (called **scan1** and **scan2**) centered at each of the  $2\theta$  sub-peaks respectively with only  $2 \times 20^2$  images. In each scan we observe two separate peaks in  $(\phi, \chi)$ -space. Figure 3.6 shows the integrated intensity of each of these sub peaks in different colors corresponding to the color of the labels in Fig. 3.5 b). We see that the imaged region of the sample is separated into two super domains, respectively in the top and bottom of the displayed region separated by a straight line.

The observed stripe features are individual elastic domains bounded by parallel planar domain walls. What we see is the intersection of these structures with the transmitted line-beam in the plane  $z = 0$ . This trace is calculated as:

<sup>7</sup>The Fourier transform of a step-function falls off as  $1/q$ .

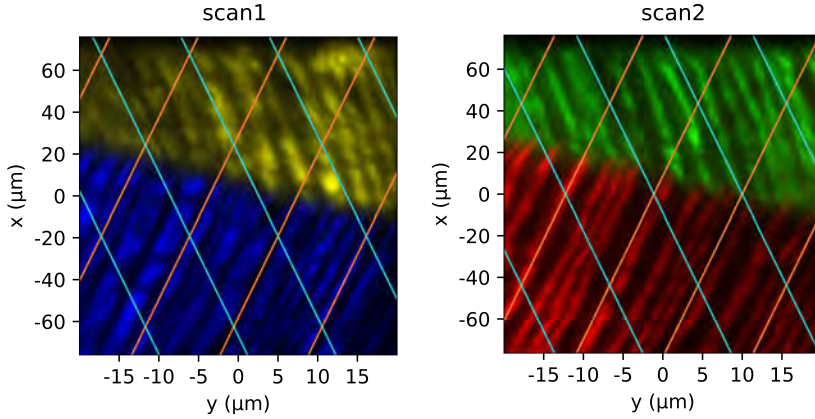


Figure 3.6: DFXM measurements of  $\text{KNbO}_3 (101)_{\text{p.c.}}$ . The plotted quantity is the integrated intensity of the four sub-peaks displayed in Fig. 3.5. The lines represent the traces of the theoretical domain walls on the  $z = 0$  plane. The colors of the lines match those in Fig. 3.5 b-d).

$$\mathbf{t} = \begin{bmatrix} 1 & 0 & 0 \\ 0 & 1 & 0 \end{bmatrix} \hat{\mathbf{z}} \times \mathbf{U} \mathbf{A}_0 \mathbf{n}_w \quad (3.45)$$

where the matrix on the RHS is a projection onto the  $(x, y)$ -plane. The lines of this orientation are plotted on top of the intensity images in Fig. 3.6 using the same colors as the peak splitting in Fig. 3.5. The directions correspond well to the observed stripe features, which gives us further confidence in our interpretation of the micro-structure: the sample contains two large stripe super-domains. One in the top of the displayed region of interest, containing stripes of the  $w_1$  domain wall and one in the bottom containing the  $w_2$  domain wall.

In theory, the stripes observed here should perfectly fill in the gaps left by the other domains. In certain areas one can find especially broad stripes that correspond to broad gaps in the other image, but the picture is somewhat distorted and irregular features appear inside the domains. These distortions are likely due to multiple scattering effects. The narrow diffraction peaks in the RSM (Fig. 3.5) suggests that the crystal is highly perfect and we only see a few dislocations in the imaged FOV.

The theory of elastically compatible twinning does not allow for any domain wall that can explain the line separating the two super-domains. The splitting of the diffraction peaks from domains separated by this boundary also do not fall along a high-symmetry direction of the lattice. A theory for compatible higher order domain structures exists but will not be pursued here.[28, 77]

The study here demonstrates that auto-correlations in the RSM along certain directions that can be predicted by the theory of elastically compatible twinning are indicators of the presence of a given domain wall, as was also demonstrated in a recent paper using only farfield diffraction data.[33] Furthermore, we give further experimental verification of the conclusions made in that paper by also imaging the domain walls in real space. We have shown that DFXM, thanks to the high resolution in reciprocal space, is able to resolve twinning relationships of this kind and that the precision of the measured reciprocal-space

information is high enough to be quantitatively compared to twin relationships, that can be calculated solely from the unit cell lattice constants.

### 3.3.2 Large-grained barium titanate ( $\text{BaTiO}_3$ ) ceramic

The study presented in the last subsection is in some sense the best case of a DFXM data-set. All features of the sample are well resolved in both real- and reciprocal space. With many samples, we will not be so lucky and the sample may contain real-space structures or strains that are too small to be resolved. To show how DFXM can be used in this case, we look at a data set from a large-grained ceramic sample of  $\text{BaTiO}_3$ , where we expect to see small ( $\approx 1 \mu\text{m}$ ) elastic domains.

$\text{BaTiO}_3$  is a perovskite ferroelectric. The structure is tetragonal with  $\tau \approx 0.01$ . The sample was prepared by sintering a commercially bought powder (99.5%  $>2\mu\text{m}$  particle size, Sigma Aldrich). The experiment was carried out at ID06-HXM in April 2015 and data from this study has previously been published in a paper that focused on the presence of small strains not related to coherent twinning.[68] Here we focus on identifying coherent twinning relationships.

#### RSM

Figure 3.7 shows the RSM of a grain in the  $\text{BaTiO}_3$  sample imaged in the  $(200)_{\text{p.c.}}$  reflection. As predicted by the theory, the peaks are separated into two distinct  $2\theta$  shells of constant  $q_{\parallel}$  marked by dotted white lines.

Since the sample at hand is a polycrystal, we don't have a surface of known crystallographic orientation to constrain the orientation by the method of Section 3.1.1. Therefore, there is one degree of freedom in the determination of the U matrix: the rotation about **Q**. We refine this last degree of freedom by identifying coherent-twin relationships in the RSM shown in figure 3.7. There are two distinct features in the RSM that can be recognized in both the high- $2\theta$  and low- $2\theta$  shells, but at different positions. The distance between these features matches the theoretical splitting given by the 110-type domain walls. If we assume that these features are related by coherent-twin relationships, we can use this information to fully determine U down to an ambiguity of the cubic symmetries. In later stages of the analysis we will see even stronger evidence that this assignment of the U matrix is correct.

The reciprocal space map shown in Fig. 3.7 does not split into a few well-defined sub-peaks as was seen for the  $\text{KNbO}_3$  single crystals. This tells us that the grain is less ordered than the single crystal, possibly due to inelastic-deformation, that was already present in the cubic parent phase such as low angle grain boundaries as is commonly observed in grains of poly-crystals[2] or possibly due to lattice rotations caused by super-domain boundaries.[77]

The RSM separates into two flat shells, one for each  $2\theta$  value. The fact that these planes are narrow shows us that there is little uniaxial strain in the  $Q$ -direction. This agrees well with the common understanding that the grain adopts a domain-configuration that minimizes the elastic strain that can be caused by interactions with neighboring grains.[5]

### 3.3.3 DFXM

The data set contains two separate 2D mosaicity scans centered on the high- and low- $2\theta$  values respectively (marked with white lines in Fig. 3.7). These two scans allow us to cover the whole peak, and therefore measure all the diffracting elements present in the sample. Because we only measure on fixed values of  $2\theta$ , we are not sensitive to small uniaxial strains that could be resolved by a different scanning approach. Also, to keep

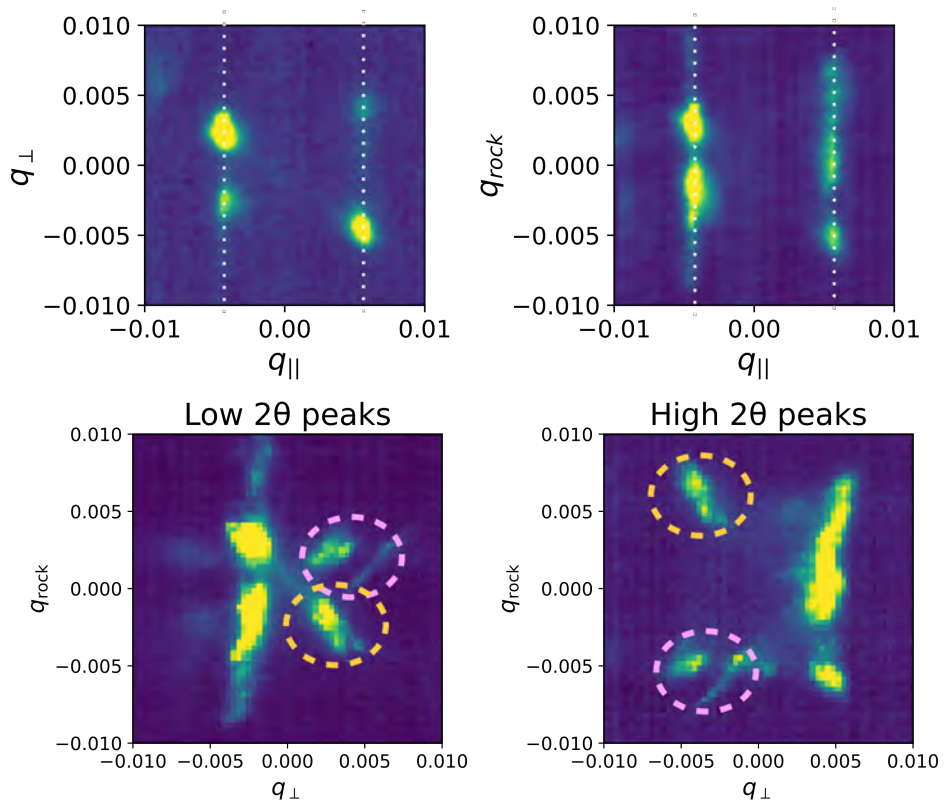


Figure 3.7: Two orthogonal projections of an RSM of BTO  $(200)_{pc}$  in the units of Eq (3.7). The white lines mark the positions of the two  $2\theta$ -planes. The high- c) and low d)  $2\theta$  regions of the RSM respectively (marked by dotted white lines in Fig. 3.7). The dashed circles mark features that can be recognized in both sub-regions.

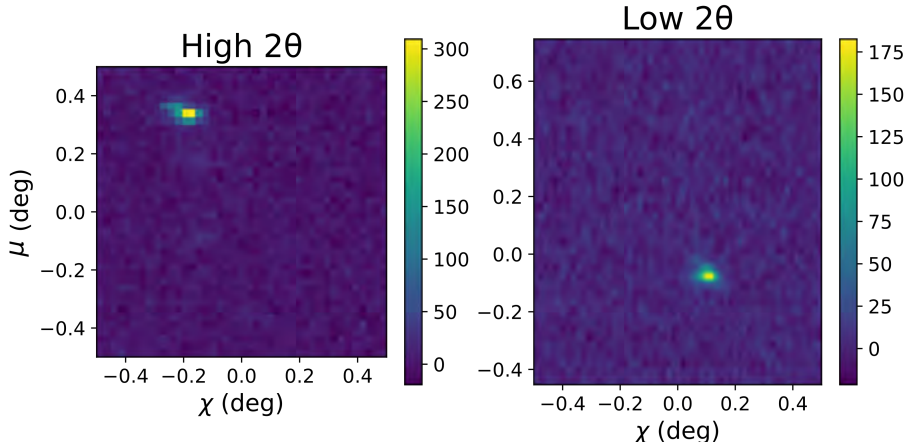


Figure 3.8: Intensity in a single pixel in the DFXM scans of the a) high  $2\theta$  and b) low  $2\theta$  sub-peaks respectively. The position of the pixel is marked with a red cross in Fig. 3.9.

measurement time short, the experiment used relatively large steps in  $\mu$  and  $\chi$ , similar to the size of the resolution function, so we also do not resolve very fine tilts of the lattice.

In these scans we identify areas where we see an isolated peak in both the high- and low- $2\theta$  scans (Fig. 3.8 shows the RSM from one such pixel) and regions where we only see a signal above a threshold value in the high- $2\theta$  peak. The regions are identified by first thresholding an image of the maximum-value recorded in each pixel, after background subtraction to create a mask. Isolated pixels are then removed from the masks and the edges of the masks are smoothed.

In the pixels where we identify a signal in both scans, we identify the peak position by the point with the highest intensity and compute the corresponding  $\mathbf{q}$ -vector for each sub-peak using the equations (3.14) and (3.8) and calculate the difference between these two vectors,  $\Delta\mathbf{q}$ , for each pixel. In Fig. 3.9 b) we plot a 2D histogram of the  $k$  and  $l$  components of these computed splitting vectors. The  $h$  component of all these vector are  $\Delta h = 0.014$ , due to the geometry of the scans. We see that the pixels preferentially fall within four peaks in the histogram that correspond well to the computed peak splitting values of  $\Delta\mathbf{h} = [0.0014, \pm 0.0014, 0]^T$  for the domain walls with normal  $\mathbf{n}_w = \mathbf{U}[1, \pm 1, 0]^T$  and  $\Delta\mathbf{h} = [0.0014, 0, \pm 0.0014]^T$  for the domain walls with normal  $\mathbf{n}_w = \mathbf{U}[1, 0, \pm 1]^T$ . This supports that our assignment of the U matrix is correct, since otherwise the histogram would be rotated. There is nothing in the analysis that forces the points to organize into these four peaks. The only tuneable parameters in this analysis are the one free angle in the determination of U and the threshold level and smoothing parameters used to generate the masks, as well as a shift correction used to align the two scans with each other. This alignment is done to compensate for shift-errors that appear when the lens is translated.

In Fig. 3.9a), we plot the angle of the individual vectors as a color-plot in real space and see that the crystal is separated into regions where the  $\Delta\mathbf{q}$  vector falls on an angle of either  $0^\circ$ ,  $90^\circ$ ,  $180^\circ$ , or  $270^\circ$ . We interpret this to be stripe-superdomains that are characterized by the presence of only a single type of domain wall where the individual stripes are not resolved in real space. The voids in the image are pixels where there is a signal in the high- $2\theta$  scan but none in the low- $2\theta$  scan. We interpret these areas to

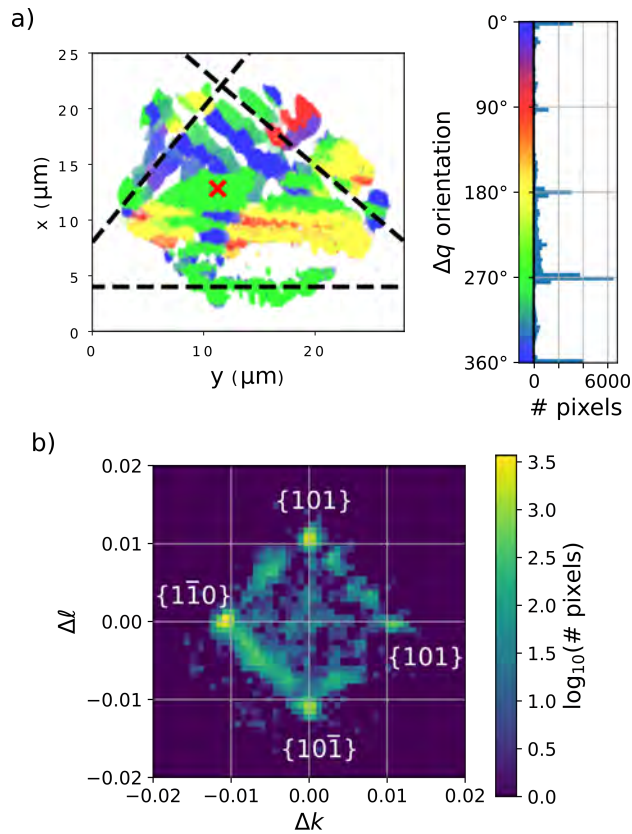


Figure 3.9: a) Pixel-wise orientation of the  $\Delta\mathbf{q}$  vector. The voids in the image are pixels where there is no signal in the low- $2\theta$  scan. Dashed lines mark the traces of the three  $\{100\}$ -planes. The red cross marks the position of the measurement shows in Fig. 3.8. b) 2D-histogram of the  $\Delta\mathbf{q}$  vectors from the same image as a).

be super-domains dominated by domain walls of orientation either  $(011)$  or  $(01\bar{1})$ , both of which do not cause a splitting of the probed  $(200)$  peak.

In the real space-images, we see that the features have interfaces that form along 3 specific directions. In our interpretation of the data these are the interfaces where stripe-domains of different domain wall orientation meet. We observe that these three directions correspond well to the three  $\{100\}$  planes (the traces of these are marked by dashed lines in Fig. 3.9a ). In the existing literature, domain super-structure in BTO polycrystals has primarily been studied on the surfaces of polished ceramics[35] or in thinned samples of sub-micron thickness.[17] In these studies, the connecting lines between stripe super-domains are commonly found to be traces of the  $\{110\}$  planes[5], which is inconsistent with our observations here. In this study, we only measure one slice through the grain so we can't fully determine the orientation of the features. This could in a future experiment be resolved by capturing data at several, closely spaced, planes by translating the sample and thereby building a 3D model of the superdomain structure.

In some pixels we see more than one peak in each scan. The existence of multiple peaks can be explained by the fact that two different super-domains fall within the point spread of a given pixel. An alternative interpretation is that some areas consist of higher-order

laminations with more than one ferroelastic domain wall.[77] These pixels contribute to the streaks between the coherent-twin peaks in Fig. 3.9b). In this paper we do not try to account for multiple peaks in each mosaicity map, but only use the max intensity measurement. A more advanced analysis that takes into account multiple peaks has been described in [32, 64].

It appears that super-domains of the type  $\{101\}$  are connected with superdomains of type  $\{011\}$  and  $\{0\bar{1}1\}$  but not  $\{\bar{1}01\}$  and a similar rules for the permutations. (in the color code of Fig 3.9 we see that blue and yellow domains are not connected and red and green domains are not connected) This is also suggested by a lack of streaks connecting the opposite peak in Fig. 3.9b) similar to the streaks connecting neighboring peaks. There are a few points in the image that appear to break these rules.



# 4 Paraxial Fourier optics and coherent phase contrast microscopy

The geometric optics description presented in the preceding chapter is convenient for understanding DFXM and interpreting experimental data. But for all its merits it fails to describe some aspects of the experiments. As was already described in Chapter 2, the geometric model is based on kinematical scattering and does not capture multiple scattering effects. Furthermore, diffraction effects were omitted in the model. For this reason, the geometrical model cannot predict the spatial resolution of the microscope and it does not correctly describe a certain type of contrast in the microscope, called *phase contrast*, which is critical to understand contrast from certain sample features.

To understand these effects, we need a different model called *wave optics*. In this approach, rather than describing the beam as an ensemble of rays, the beam is modeled by a scalar wave field (the same quantity as the envelope functions  $\mathbf{E}_n(\mathbf{r})$ , introduced in Eq. (2.7)). This is, once again, only an approximation to the time-dependent problem given by the Maxwell's equations and relies on the beam being monochromatic and transversely coherent. We will take a closer look at the validity of these approximations in Chapter 7.

In this chapter, we first introduce the basics of wave-optics: the free space propagator, the projection approximation, and the coherent microscope. Then we describe how to perform numerical calculations using discrete Fourier transforms. Finally we introduce two approaches to analyze data from a coherent microscope: *differential phase contrast* and *Fourier ptychography*.

## 4.1 Free-space propagation

Starting from Eq. 2.6, we introduce the monochromatic modulated plane wave:

$$\mathbf{E}(\mathbf{r}, t) = E(\mathbf{r})e^{-i\omega t + i\mathbf{k}\cdot\mathbf{r}}\hat{\mathbf{p}} \quad (4.1)$$

where  $\hat{\mathbf{p}}$  is the polarization vector and  $\mathbf{k}$  is an average wave-vector and  $E(\mathbf{r})$  is a slowly varying envelope function. Plugging this into Eq. 2.6 we get the scalar Helmholtz equation for the envelope function:

$$\left( \nabla^2 + 2ik \frac{\partial}{\partial z} + k^2 \chi_0 \right) E = 0 \quad (4.2)$$

where we've chosen  $\mathbf{k} = \hat{\mathbf{z}}$ . We are interested in finding the complex amplitude of  $E$  at some plane  $z = z_2$  given the amplitude at some other plane  $z = z_1 < z_2$ . For this purpose it is convenient to split the Laplacian into a transverse and a longitudinal component,  $\nabla^2 = \nabla_{\perp}^2 + \frac{\partial^2}{\partial z^2}$ .

The *paraxial approximation* is to assume that the field is beam-like and therefore varies much more slowly in the direction of propagation than in the transverse directions. Therefore we can discard the second order term in  $z$ . Finally, we set  $\chi_0 = 0$  and we arrive at the paraxial Helmholtz equation in a vacuum:

$$\nabla_{\perp}^2 E = -2ik \frac{\partial E}{\partial z} \quad (4.3)$$

The equation is now first order in the dynamical variable,  $z$ . To solve it we introduce the transverse Fourier transformation, defined as:

$$\tilde{E}(s_x, s_y) = \mathcal{F}\{E(x, y)\} = \int dx dy E(x, y) e^{-2\pi i(x s_x + y s_y)} \quad (4.4)$$

where  $s_x, s_y$  are the full period spatial frequencies. A number of definitions and useful properties of the Fourier transform are given in Appendix A.2. We Fourier transform both sides of (4.3) and use the derivative theorem to re-write the partial differential equation as a first-order ordinary differential equation in  $z$ .

$$4\pi^2(s_x^2 + s_y^2)\tilde{E}(s_x, s_y, z) = -2ik \frac{\partial}{\partial z} \tilde{E}(s_x, s_y, z) \quad (4.5)$$

Which is solved by:

$$\tilde{E}(s_x, s_y, z_2) = P_{(z_2 - z_1)} \tilde{E}(s_x, s_y, z_1) \quad (4.6)$$

where we have defined the propagator function  $P_L = e^{i2\pi^2(s_x^2 + s_y^2)L/k}$ . As the Fourier transform is exactly inverted by the inverse Fourier transform, we can write the solution to the differential equation (4.3) as:

$$E(x, y, z_2) = \mathcal{F}^{-1}\{P(s_x, s_y)_{z_2 - z_1} \mathcal{F}\{E(x, y, z_1)\}\} \quad (4.7)$$

This describes a way to propagate a wave front from one plane to another and we define a linear operator, called a propagator, according to:

$$\mathcal{P}_{(L)}\{E(x, y)\} = \mathcal{F}^{-1}\left\{e^{-i\pi(s_x^2 + s_y^2)\lambda L} \mathcal{F}\{E(x, y)\}\right\} \quad (4.8)$$

This is the free space Fourier-propagator, which can be implemented in numerical calculations with the use of discrete Fourier transforms. The Fourier propagators (both the continuous and the discrete versions) are linear operators on the 2D wave fronts.

## 4.2 The projection approximation

In free space we can propagate wave fronts from one plane to another using the free space propagator, but in a medium, the problem is more difficult. There are a number of basic optical components we would like to be able to handle: apertures, lenses and samples. For all of these there is a useful approximation called the *projection approximation*, which makes the propagation through these components a simple multiplication of the wave fronts in real space by a transmission function. When the projection approximation

is appropriate for a given optical component, we say that the given component is optically *thin*.

The projection approximation is to omit the Laplacian term in the Helmholtz equation entirely. This lets us symbolically integrate the Helmholtz equation:

$$\begin{aligned}\frac{\partial E}{\partial z} &= -i\frac{k}{2}\chi_0(x, y, z)E \\ \Rightarrow E(x, y, z) &= \exp\left(ik/2 \int_{z_0}^z \chi_0(x, y, z)dz\right) E(x, y, z_0) \\ \Rightarrow E(x, y, z) &= T(x, y)E(x, y, z_0)\end{aligned}\quad (4.9)$$

where we have defined the transmission function,  $T(x, y)$ , of the thin optical component. If the component consists of a homogeneous material with varying thickness,  $h(x, y)$  and vacuum in the gaps not filled by the component, then we can write this as:  $T(x, y) = \exp(ikh(x, y)\chi_0/2)$ . If the component is also physically thin we may choose  $z \rightarrow z_0$  and treat the effect of the component as purely a multiplication by a transmission function.

The susceptibility function is related to the complex refractive index,  $n$ , by:

$$n = \sqrt{1 + \chi_0} \approx 1 + \chi_0/2 \quad (4.10)$$

Optical set-ups that consist of several lenses and apertures can be treated as a number of free-space propagators and a number of thin components.

### 4.2.1 The coherent microscope

The simplest microscope consists of 4 components: a light source, a sample, an objective lens, and a detector. These components are placed on a common axis and separated by the distances  $d_0$ ,  $d_1$ , and  $d_2$ . (see Fig. 4.1) When we say that the microscope is coherent, we mean that the source is taken to be infinitely small.<sup>1</sup> In practice, it is sufficient to require that the angular divergence of the incident light at the sample is much smaller than the numerical aperture (NA) of the objective lens where the NA is the sine of the largest angle of scattered light from the sample that is captured by the objective lens. Some authors work with a *coherence parameter*, [76]  $S$ , which is the ratio of the NA of the condenser lens to the NA of the objective lens.  $S = 1$  is a normal incoherent microscope and  $S \rightarrow 0$  is a coherent microscope.

In the following, we will assume that the source-to-sample distance is infinite, which means the sample is illuminated by a flat wave front of constants phase and intensity. We set the sample position to  $z = 0$ .

We want an expression that allows us to propagate the wave front from the sample plane at  $z = 0$  through the lens onto the image plane. We could approach this with the simple

---

<sup>1</sup> This comes from the old theory (before lasers) when all sources were assumed to be spatially incoherent. Modern synchrotrons are considered to be partially coherent sources and the distinction between coherent and incoherent is a bit more complicated.

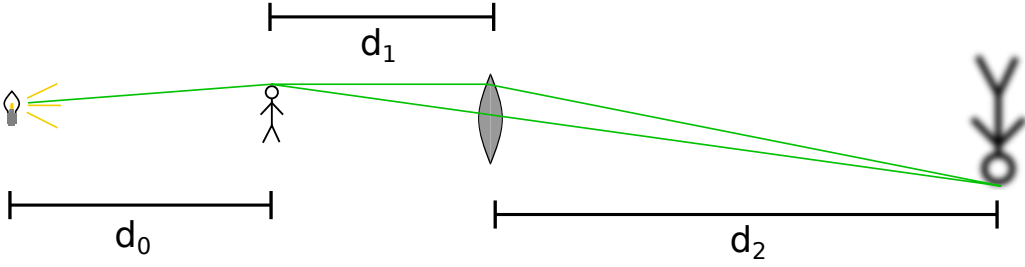


Figure 4.1: Sketch of a simple coherent microscope.

Fourier propagator from Eq. (4.8) but this would turn out to be difficult to handle numerically because of the large convergence of the light directly after the lens. Instead we start from the *Fresnel diffraction integral*, which is a solution of the paraxial Helmholtz-equation:

$$E(x', y', d_1) = \frac{\exp(i2\pi d_1/\lambda)}{(i\lambda d_1)^{1/2}} \exp\left[\frac{i\pi(x'^2 + y'^2)}{\lambda d_1}\right] \times \int \int dx dy \exp\left[\frac{-i2\pi(xx' + yy')}{\lambda d_1}\right] \times \exp\left[\frac{i\pi(x^2 + y^2)}{\lambda d_1}\right] E(x, y, 0) \quad (4.11)$$

This integral gives the field at the lens-plane ( $z = d_1$ ) by an integral over the field at the sample plane. We multiply this by the transmission function of the lens,  $T_{\text{Lens}}$ , and write up another integral giving the amplitude at the image plane by the amplitude at the sample plane:

$$E(x'', y'', d_1 + d_2) = \frac{\exp(i2\pi d_2/\lambda)}{(i\lambda d_2)^{1/2}} \exp\left[\frac{i\pi(x''^2 + y''^2)}{\lambda d_2}\right] \times \int \int dx' dy' \exp\left[\frac{-i2\pi(xx' + yy')}{\lambda d_2}\right] \times \exp\left[\frac{i\pi(x'^2 + y'^2)}{\lambda d_2}\right] T_{\text{Lens}}(x', y') E(x', y', d_1) \quad (4.12)$$

Combining equations (4.11) and (4.12) and taking the absolute square gives:

$$|E(x'', y'', d_1 + d_2)|^2 = \frac{1}{\lambda^2 d_1 d_2} \left| \int \int dx' dy' A(x', y') \exp\left[\frac{-i2\pi(x''x' + y''y')}{\lambda d_2}\right] \times \int \int dx dy \exp\left[\frac{-i2\pi(x'x + y'y)}{\lambda d_1}\right] \exp\left[\frac{i\pi(x^2 + y^2)}{\lambda d_1}\right] E(x, y, 0) \right|^2 \quad (4.13)$$

where the aperture function,  $A(x, y)$ , is:

$$A(x, y) = \exp\left[\frac{i\pi(x^2 + y^2)}{\lambda d_1}\right] T_{\text{Lens}} \exp\left[\frac{i\pi(x^2 + y^2)}{\lambda d_2}\right] \quad (4.14)$$

We want to rewrite this expression using a pair of Fourier transforms. In order to bring the integrals to match the definition of the Fourier transform and its inverse, we introduce the scaled integration variables  $s_x = \frac{x'}{\lambda d_1}$  and  $s_y = \frac{y'}{\lambda d_1}$  and the magnification factor:

$$M = -\frac{d_2}{d_1} \quad (4.15)$$

Using this we re-write Eq. (4.13):

$$\begin{aligned} & |E(Mx, My, d_1 + d_2)|^2 \\ &= \frac{d_1}{d_2} \left| \mathcal{F}^{-1} \left\{ A(-s_x \lambda d_1, -s_y \lambda d_1) \mathcal{F} \left\{ \exp \left[ \frac{i\pi(x^2 + y^2)}{\lambda d_1} \right] E(x, y, 0) \right\} \right\} \right|^2 \end{aligned} \quad (4.16)$$

A special case of this expression comes when we assume that the lens is a perfect lens which is a thin optical component with the transmission function:

$$T_{Lens} = \exp \left( -i\pi \frac{x^2 + y^2}{\lambda f} \right) \quad (4.17)$$

where  $f$  is a real constant called the focal length. With this particular transmission function, the aperture function  $A$  simplifies to:

$$A(x, y) = \exp \left[ \frac{i\pi(x^2 + y^2)}{\lambda} \left( \frac{1}{d_1} + \frac{1}{d_2} - \frac{1}{f} \right) \right] \quad (4.18)$$

$A(x, y)$  becomes everywhere equal to one, when the following equation is fulfilled:

$$\frac{1}{f} = \frac{1}{d_1} + \frac{1}{d_2} \quad (4.19)$$

which is the *thin-lens equation*.

When the thin lens equation is fulfilled, the two Fourier transforms cancel each other out and the intensity at  $z = d_1 + d_2$  is an exact – magnified and inverted – image of the intensity at  $z = 0$ . Any deviation of the aperture function from unity is thus a deviation of the lens from a perfect lens and will introduce errors in the image.

Necessarily, the lens is of a limited size. For a circular lens we have  $A(x', y') = 0$  outside of some radius  $x'^2 + y'^2 > R_A^2$ . This cut-off sets a maximum spatial frequency,  $s_{\max} = \frac{R_A}{\lambda d_1}$  that can be captured by the lens, which in turn sets an approximate resolution limit on the imaging system: The Abbe-diffraction limit

$$d_{Abbe} = \frac{1}{2s_{\max}} = \frac{\lambda R_A}{2d_1} = \frac{\lambda}{2NA} \quad (4.20)$$

where NA is the numerical aperture of the microscope.  $d_{Abbe}$  is the smallest spacing between parallel straight lines in a sample, where the individual lines can still be distinguished in the image and sets an upper limit on the resolution of the microscope.

The quadratic phase factor remaining in equation (4.16) is called the *near field phase factor*. It determines how light stemming from different points on the sample plane strike the lens at different points. It becomes significant when the size of the sample is of a similar size to or larger than the aperture of the lens, and can only be safely ignored when

$$R_A \gg L_x \quad (4.21)$$

where  $L_x$  is the linear size of the sample.

This is not immediately obvious from the equations but it can be motivated by seeing that the near field term can locally be approximated by a harmonic function  $e^{i2\pi/\lambda d_1 x_0}$  at a point in the sample plane  $(x_0, 0, 0)$ . From the Fourier shift theorem (Eq. A.14), we see that the role of this term is to shift the Fourier spectrum by a spatial frequency,  $x_0/\lambda d_1$ . Comparing this to the characteristic scale in reciprocal space,  $s_{\max}$ , we see that the near field term can be ignored when  $x_0 \ll R_A$ . This argument doesn't hold when there are other significant length-scales in the aperture function, which will be the case for aberrated lenses. In this case, the near-field terms will be responsible for creating a de-focused image of the lens aberrations on the image-plane. For the types of x ray microscopy investigated in this thesis, the size of the FOV is limited by the NA of the lens, so we will always have to include the near field phases.

Aside from the aperture, the value of the lens transmission function may deviate from that of an ideal lens in several other ways. We call these deviations *aberrations*.

Equation (4.16) can be seen as a propagator that includes both the propagation and the effect of the lens in a single Fourier convolution. It can be implemented with discrete Fourier transforms in a way similar to the paraxial propagator of Eq (4.8).

### 4.3 Discetization & numerical calculations

In the preceding section, we derived a number of equations describing how to relate the amplitudes of coherent wave fronts in one plane to the amplitudes in a different plane using continuous Fourier transforms. In this section we deal with the numerical representation of these wave fronts and the implementation of propagators.

When doing numerical calculations, both for simulation and data-analysis, we will represent the coherent wave fronts by 2D arrays containing values of the complex envelope functions,  $E(x_j, y_k; z_0)$ , sampled at discrete points  $(x_j, y_k) = (a_x j_x, a_y j_y)$ , where  $j = 0, 1, \dots, N_x - 1$  and  $j = 0, 1, \dots, N_y - 1$ . When working with experimental data, these grids will be defined by the pixels of the image-detectors.

The discrete 2D Fourier transforms (DFT) of these arrays are proportional to the continuous 2D Fourier transform evaluated on a grid of points in  $(s_x, s_y)$ -space:  $(s'_{x,l}, s'_{y,m}) = (\Delta s_x l, \Delta s_y m)$  where  $l = 0, 1, \dots, N_x - 1$  and  $m = 0, 1, \dots, N_y - 1$  and  $\Delta s_x = 1/(N_x a_x)$  and  $\Delta s_y = 1/(N_y a_y)$ . This may be shown from Eq. (4.4), by approximating the integral by a sum:

$$\tilde{E}(s_x, s_y) = \int \mathbf{d}x \mathbf{d}y E(x, y) e^{-2\pi i(x s_x + y s_y)} \approx a_x a_y \sum_{j,k=0}^{N_x-1, N_y-1} E(x_j, y_k) e^{-2\pi i(x_j s_x + y_k s_y)} \quad (4.22)$$

which, apart from a constant pre-factor, matches the definition of the DFT in exactly these points. It is clear that this can only be a good approximation if the function  $E(x, y; z_0)$  is close to zero outside the range covered by the sum  $x \in [0, (N_x - 1)a_x], y \in [0, (N_y - 1)a_y]$ .

Because of aliasing, the points in the higher half of the frequency spectrum are equivalent to points at small negative frequencies. Therefore we can make a new grid, where the higher half is shifted down in frequency so that the grid covers a rectangle in  $(s_x, s_y)$ -space centered on zero. We refer to the points of this shifted grid with the coordinates  $(s_{x,l}, s_{y,m})$ .

By the same argument we used to require that  $E(x, y)$  is close to zero outside the grid in  $(x, y)$ -space, we also need to require that  $\tilde{E}(s_x, s_y)$  is non zero outside the grid in  $(s_x, s_y)$ -space when we write up the inverse Fourier transform. The highest frequency in this box is called the *Nyquist frequency* and is given by  $s_{Ny,x} = 1/2a_x$ . When this requirement holds, we say that the function is well-sampled.

This suggests an implementation of the propagator (Eq. 4.8) using DFTs to approximate the Fourier transforms. In expressions like this, where a direct and an inverse Fourier transform appear as a pair, the pre-factors cancel out and we can write:

$$\mathcal{P}_L \{E(x_j, y_k)\} \approx \text{DFT}^{-1} \left\{ e^{-i\pi(s_{x,l}^2 + s_{y,m}^2)\lambda L} \text{DFT} \{E(x_j, y_k)\} \right\} \quad (4.23)$$

this is a good approximation only when the chirp-function in this expression is well sampled by the grid in  $q$ -space. At the edge of the reciprocal space grid the chirp function does a full phase wrap in a distance  $a_x/(L\lambda)$ . Requiring that this distance is more than twice the step-size of the grid:  $L < a_x^2 N_x / 2\lambda$ , sets an upper limit on the length over which we can use this propagator.

One can show that this discrete propagator is in fact the exact solution for the paraxial propagation of an infinite, **periodic** wave-front, where the grid covers one periodic unit. DFT methods implicitly assume periodic boundary conditions of the fields. This has the consequence that intensity that would diffuse out of the edge of the grid appears back at the other side of the grid. To avoid errors caused by this effect, simulations of confined beams should be set up with a some margin in the 2D arrays on all sides of the wave-front filled with zeros called the *padding*.

### 4.3.1 The coherent microscope

As was done in the last subsection, we can straightforwardly write up the discrete version of Eq. 4.16 by replacing the continuous Fourier transforms by DFTs:

$$\begin{aligned} & |E(Mx_j, My_k, d_1 + d_2)|^2 \\ &= \frac{d_1}{d_2} \left| \text{DFT}^{-1} \left\{ A(-s_{x,l}\lambda d_1, -s_{y,m}\lambda d_1) \text{DFT} \left\{ \exp \left[ \frac{i\pi(x_j^2 + y_k^2)}{\lambda d_1} \right] E(x_j, y_k, 0) \right\} \right\} \right|^2 \end{aligned} \quad (4.24)$$

In contrast to the free-space propagator, the intensities we calculate with this equation are not given on the same grid as the input. The output grid is scaled by a factor of  $M$ , the magnification of the microscope.

For this model to work, we have to require that both the aperture function and the near field phase factors are well sampled. The requirement for the near field factors read  $(2\lambda d_1)/L_x > 2a_x$ . For the aperture function, the reciprocal space grid corresponds to a real-space grid on the lens plane with step-size  $\Delta x_{lens} = \lambda d_1 \Delta s_x = \lambda d_1 / (N_x a_x)$ .

We can re-write the double Fourier transformations, in both this expression and the continuous version, as a convolution of the phase-corrected sample plane field by a coherent point spread function (cPSF) by applying the convolution theorem.

$$|E(Mx, My, d_1 + d_2)|^2 = \frac{d_1}{d_2} \left| \text{cPSF}(x, y) \otimes \left[ \exp\left(\frac{i\pi(x^2 + y^2)}{\lambda d_1}\right) E(x, y, 0) \right] \right|^2 \quad (4.25)$$

where

$$\text{cPSF}(x, y) = \mathcal{F}^{-1} \{A(-s_x \lambda d_1, -s_y \lambda d_1)\} \quad (4.26)$$

The complex amplitude of the cPSF describes how the image of a point-like field in the sample plane is broadened in the image plane. For a good microscope this is a narrow real positive function centered on zero, but aberrations in the aperture function tend to broaden the cPSF and therefore degrade the resolution of the microscope.

## 4.4 Differential phase contrast (DPC)

With an ideal lens, the simple coherent microscope presented Section 4.2.1 generates an image in the image plane, which is an exact magnified copy of the **intensity** of the field in the sample plane. The measured image is thus independent of the phase of the wavefront. By introducing any deviation from this ideal microscope, however, one changes the image in a way that depends not only on the intensity in the sample plane but also on the **phase**. [86] By designing specific deviations from an ideal lens or by systematically varying specific parameters of the microscope geometry, one can maximize the contrast due to the phase, or even construct measurement schemes that allows one to recover the phase of the wave front in the sample plane. Such methods are called *phase contrast microscopy*. In this and the following section we will describe two of these methods that we have implemented in an x-ray microscopes.

Differential phase contrast (DPC) is a family of such microscopy techniques that image the phase-delay imparted by a sample, by either illuminating the sample obliquely [86, 76] or by measuring the deflection angle of the transmitted light with optical components downstream of the sample. [81, 82] Typically DPC is done in incoherent microscopes, but a similar technique can be performed in a coherent microscope by shifting the position of the lens. Starting from Eq. (4.16), we introduce a shifted lens with transmission function:

$$T_\sigma(x, y) = A(x - \sigma_x, y - \sigma_y) \exp\left(-i\pi \frac{(x - \sigma_x)^2 + (y - \sigma_y)^2}{\lambda f}\right) \quad (4.27)$$

Where  $\sigma_x$  and  $\sigma_y$  parameterize the shift of the lens. Applying the Fourier shift theorem and moving around some terms we will find that the shifted lens produces an image,

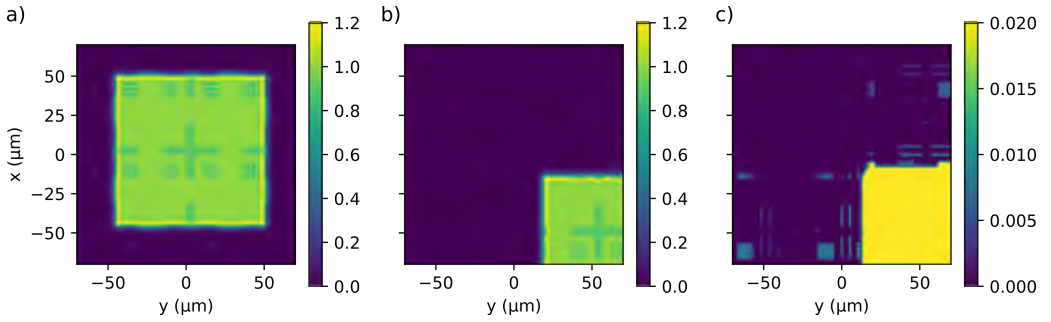


Figure 4.2: a) Simulated image using Eq. (4.28) with  $\sigma = 0$ , b)  $\sigma = [50 \mu\text{m}, 50 \mu\text{m}]$  and c)  $\sigma = [50 \mu\text{m}, 50 \mu\text{m}]$  with an adjusted colormap to make the weak intensity visible.

shifted by a distance  $(|M| + 1)\sigma$  and with the aperture function shifted in  $s$ -space by an amount  $s_\sigma = -\frac{\sigma}{\lambda d_1}$ . We write up an expression for the shifted and magnified image:

$$I(Mx - (M + 1)\sigma_x, My - (M + 1)\sigma_y; \sigma_x, \sigma_y) = \left| \mathcal{F}^{-1} \left\{ A_\sigma(-s_x \lambda d_1, -s_y \lambda d_1) \mathcal{F} \left\{ \exp \left[ \frac{i\pi(x^2 + y^2)}{\lambda d_1} \right] E(x, y, 0) \right\} \right\} \right|^2 \quad (4.28)$$

where  $A_\sigma(x, y) = A(x - \sigma_x, y - \sigma_y)$  is the shifted aperture function. Figure 4.2 shows a few simulated images calculated with this model. For this simulation the lens was taken to have a square absorbing aperture of full width 0.1 mm. In Fig. 4.2 a) the square shape of the aperture is clearly visible. We see a bright image of the part of the sample inside a certain region with the same shape as the lens. The area outside of this region appears dark. When the lens is moved, the outline of the aperture is also moved. In c) we adjust the colormap to show that the dark region does contain some intensity around sharp edges and high-frequency features of the sample. This type of contrast is typically called *dark field contrast* and on the other hand the image inside the square region is called *bright field contrast*.

We will avoid this word due to the double-meaning of **dark-field** as it is also used in the name DFXM to denote the Bragg-scattered beam rather than the transmitted beam. This can be seen as an example of the same phenomenon where the lattice of the crystal is the high-frequency feature causing contrast at a large scattering angle. In the DFXM literature sometimes the terms *weak beam* and *strong beam* is used instead.

By shifting the lens to a number of different positions,  $\sigma^{(p)}$  for  $p = 0, 1, 2, \dots, P - 1$  and sequentially measuring a stack of images, we can measure the function  $I(x, y; \sigma)$  at different shifts and use these measurements to infer information about the field in the sample plane,  $E(x, y, 0)$ . The approach to this is to consider the function for a single point in  $x$  and  $y$ , that is to say, for a single pixel on the detector, and to look at the intensity in this pixel as a function of the 2-dimensional shift variable  $\sigma$ . From this function, we calculate a number of quantities which we will refer to as the moments, equivalent to the central moments of a probability distribution:

$$I_{\text{int}}(x, y) = \sum_p I(x, y; \boldsymbol{\sigma}^{(k)}) \quad (4.29)$$

$$\text{COM}_x(x, y) = \frac{1}{I_{\text{int}}(x, y)} \sum_p I(x, y; \boldsymbol{\sigma}^{(k)}) \sigma_x^{(k)} \quad (4.30)$$

$$\text{COM}_y(x, y) = \frac{1}{I_{\text{int}}(x, y)} \sum_p I(x, y; \boldsymbol{\sigma}^{(k)}) \sigma_y^{(k)} \quad (4.31)$$

$$\text{Var}_x(x, y) = \frac{1}{I_{\text{int}}(x, y)} \sum_p I(x, y; \boldsymbol{\sigma}^{(k)}) (\sigma_x^{(k)} - \text{COM}_x(x, y))^2 \quad (4.32)$$

$$\text{Var}_y(x, y) = \frac{1}{I_{\text{int}}(x, y)} \sum_p I(x, y; \boldsymbol{\sigma}^{(k)}) (\sigma_y^{(k)} - \text{COM}_y(x, y))^2 \quad (4.33)$$

$$\begin{aligned} \text{COV}(x, y) &= \frac{1}{I_{\text{int}}(x, y)} \sum_p I(x, y; \boldsymbol{\sigma}^{(k)}) \\ &\quad \times (\sigma_y^{(k)} - \text{COM}_y(x, y)) (\sigma_x^{(k)} - \text{COM}_x(x, y)) \end{aligned} \quad (4.34)$$

The benefit of these computed quantities is that the integrated intensity,  $I_{\text{int}}$ , is an estimate of the field amplitude  $|E(x, y, 0)|^2$  and the center-of-mass (COM) functions give estimates of the gradients of the phase of the sample field. The three variances ( $\text{Var}_x$ ,  $\text{Var}_y$  and the covariance (COV)) together provide a measure of the amount and direction of unresolved high-frequency features in the sample field. Figure 4.3 shows the calculated moments from a calibration sample containing two sets of dense line-patterns close to the resolution limit of the objective lens. The images were measured at the ID06-HXM x-ray microscope by the method described in this section. The sample consists of a 650 nm thick tungsten pattern deposited on top of a flat silicon substrate. The COM signals are asymmetric around sample features. The two variances have a high signal at the vertical and horizontal stripes respectively. The co-variance shows a small negative signal for the vertical lines and a small positive signal for the horizontal lines revealing a small misalignment of the sample compared to the translations of the lens.

### Quantitative phase from COM measurements

The quantitative phase-gradients may readily be estimated from the COM measurements and can be integrated to yield an estimate of the quantitative phase of the sample field (down to a constant offset). What follows is a motivating derivation of the relation between the phase gradient and the COM.

We re-write Eq. (4.28) using the convolution theorem:

$$I(x, y; \boldsymbol{\sigma}) = \frac{d_1}{d_2} \left| \text{cPSF}_s(x, y) \otimes \exp \left[ \frac{i\pi(x^2 + y^2)}{\lambda d_1} \right] E(x, y) \right|^2 \quad (4.35)$$

The quantity:

$$\text{cPSF}_\sigma(x, y) = \mathcal{F}^{-1} \left\{ A_\sigma(-s_x \lambda d_1, -s_y \lambda d_1) \right\} = \text{cPSF}(x, y) e^{i2\pi(\sigma_x x + \sigma_y y)} \quad (4.36)$$

is the coherent point spread function of the shifted objective lens, which we have written as a product of the cPSF and a harmonic function by applying the Fourier shift theorem.

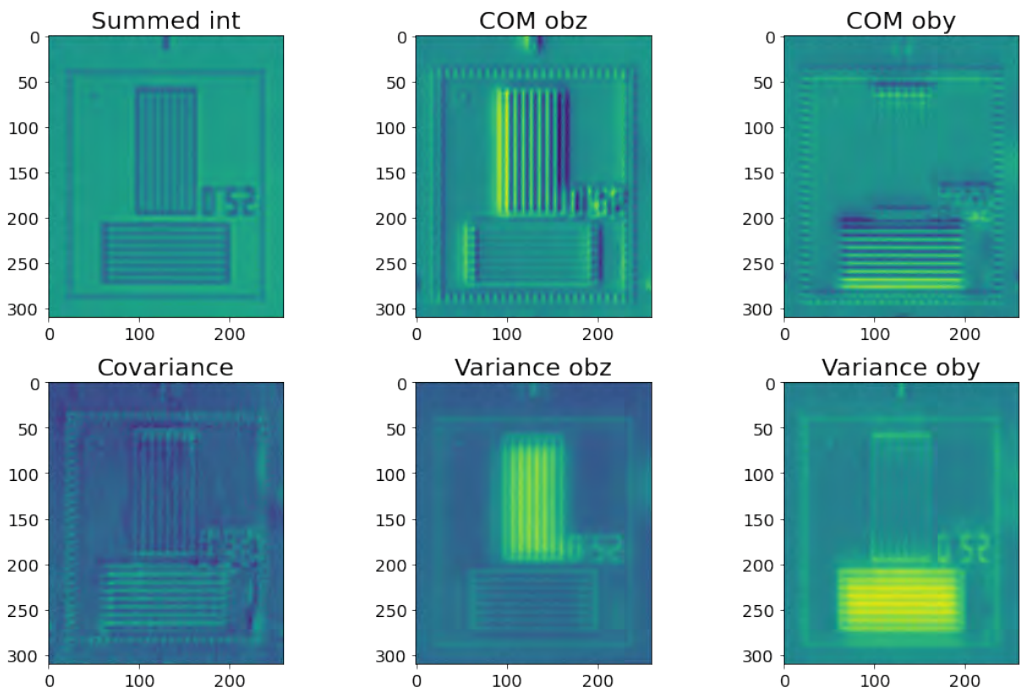


Figure 4.3: Moments calculated using the the equations (4.29) - (4.34) after correcting registration errors. The linear, geometric term in the COM images has been subtracted before plotting to make the sample features more visible.

In a good microscope, the point spread function has tight support around  $x, y = 0$ . So the intensity in a single point  $(x_0, y_0)$  only depends on the sample field in the neighborhood of that point. If we then assume that the phase of the the sample field is slowly varying in the neighborhood of this point, we may replace the phase by its 1st order Taylor expansion:

$$\exp \left[ \frac{i\pi(x^2 + y^2)}{\lambda d_1} \right] E(x, y) \approx e^{i2\pi(xx_0+yy_0)/(\lambda d_1)} |E(x, y)| e^{i\nabla_x \phi x + i\nabla_y \phi y} \quad (4.37)$$

where we have also discarded constant phase terms because it will not have any impact on the final result. We Fourier transform this expression and re-write the RHS using the Fourier shift theorem:

$$\begin{aligned} \mathcal{F} \left\{ e^{i\pi(x^2+y^2)/(\lambda d_1)} E(x, y) \right\} (s_x, s_y) \\ \approx \mathcal{F} \{ |E(x, y)| \} (s_x - \nabla_x \phi / 2\pi - x_0 / (\lambda d_1), s_y - \nabla_y \phi / 2\pi - y_0 / (\lambda d_1)) \end{aligned} \quad (4.38)$$

From this final expression we see that the role of the phase-gradient is to shift the Fourier spectrum of the sample function. Since the Fourier transform of the absolute is a symmetric function around zero, the center of the intensity distribution, which the COM is an approximation of, is given by the magnitude of this shift. We set the argument of the function on the RHS equal to zero and identify the corresponding  $s$ -values as the COM:

$$\text{COM}_x(x_0, y_0) \approx x_0 + \nabla_x \phi(x_0, y_0) \frac{\lambda d_1}{2\pi} \quad (4.39)$$

$$\text{COM}_y(x_0, y_0) \approx y_0 + \nabla_y \phi(x_0, y_0) \frac{\lambda d_1}{2\pi} \quad (4.40)$$

The choice of the point  $(x_0, y_0)$  was arbitrary to begin with, so we can generalize the result to any point  $(x, y)$ . These equations also reveal the important result that the center of the intensity distribution is shifted as a function of  $x$  and  $y$  according to a simple geometric law. This results in a large linear component to the calculated COM images, which should be subtracted to yield the phase-gradient. Fig. 4.4 shows the measured intensity distribution from the same data set but at two different positions in the Field Of View (FOV). In this experiment, the lens contained a square absorbing aperture and the intensity distribution appears to be a low-resolution image of the aperture function. This is the case when the sample field has a narrow Fourier transform compared to the aperture of the objective lens.

The phase-gradients estimated by this approach from the COM of the image stack can be integrated to yield an estimate of the quantitative phase. Fig. 4.5 shows the result of this integration. We use the least-squares cosine transform method described in [8, 39]. The phase recovered directly by this method shows clear signs of defocus, but when the quantitative phase is available we can digitally re-focus the complex amplitudes to recover the focused phase.

In DFXM the COM is often used as a way to find the centroid of the scattered intensity in reciprocal space as a function of the scan angles.[3] Therefore the DPC method that we state here is identical to one of the conventional approaches to DFXM, when it is used on a scattered x-ray beam.

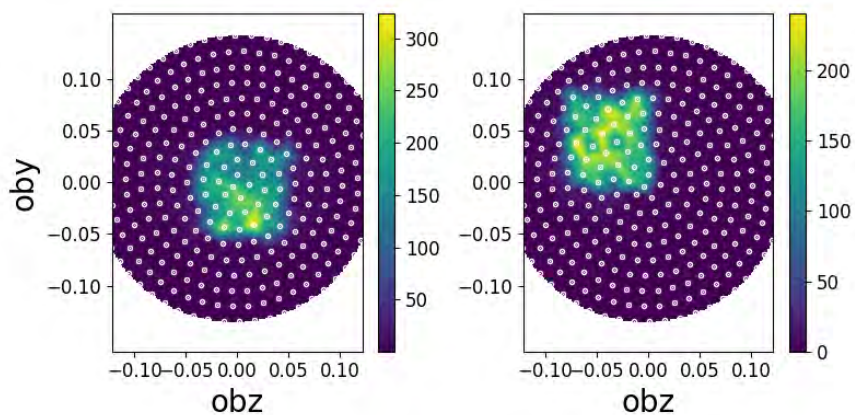


Figure 4.4: Measured single pixel intensity distributions from the same data set at two different points in the FOV.

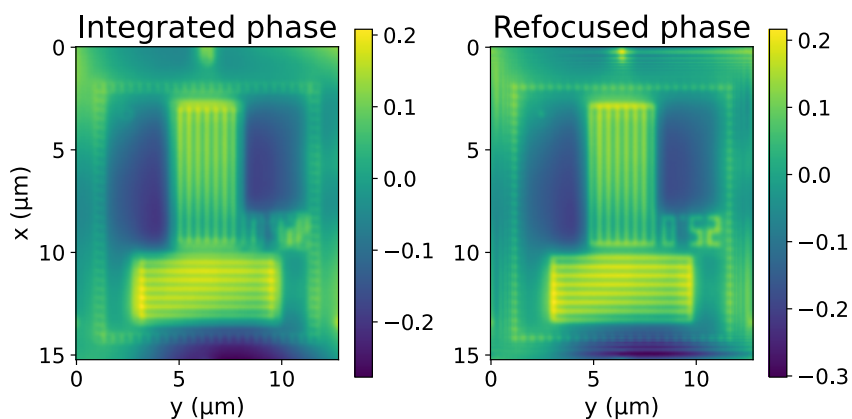


Figure 4.5: Integrated phase based on the COM phase gradients and a digitally refocused version of the same phase function.

## 4.5 Fourier ptychography (FP)

Fourier ptychography is a different approach to the treatment of the same data set as for DPC. That is to say, a set of  $P$  images,  $I_p(x_i, y_j)$ , measured at a number of different 2-dimensional misalignment positions  $\sigma_p$ .

Where the approach in DPC was to slice the data set along the  $\sigma$ -dimension to estimate the phase-gradients in each pixel individually, the approach of FP is to treat the estimation of the complex amplitudes as a global problem and to minimize the difference between the measured images and a prediction  $I_{\text{pred}}$  by optimizing the parameters of the forward model that generates the predictions.

Fourier Ptychography does not only aim to recover the quantitative phase of the sample field, but aims to reconstruct a high-resolution image of the sample that beats both the resolution limits set by the Abbe diffraction limit of the objective lens and the Nyquist frequency set by the grid of detector pixels.

### 4.5.1 Discretization

In general, the model is that of Equation (4.28) where the shifts  $\sigma_x$  and  $\sigma_y$  are known beforehand and the function  $E$  is found by optimization. The problem is closely related to the more well known problem of “normal” ptychography and the algorithms for solving one can be applied to the other. A large number of such algorithms have been investigated in the literature.[44] Some of these are presented as gradient-based optimization algorithms that aim to minimize an error function, related to the difference between the model predictions and the measured images. More commonly, the optimization strategy is formulated as a search for a common solution to a number of low-dimensional constraints.

The different methods all share the same discrete forward-model to describe the imaging-process: A number of images  $I_p \in \mathbb{R}^{N_x N_y}$  are given. The images define a  $N_x$  by  $N_y$  grid with step-sizes  $a_x, a_y$  in the respective directions, given by the demagnified spacing of the detector pixels. To this grid belongs a corresponding reciprocal-space grid with the same shape and with step sizes given by  $\Delta s_x = 1/(N_x a_x)$  and  $\Delta s_y = 1/(N_y a_y)$ . The grid is centered on zero, and thus covers the range  $s_x \in [-1/(2a_x), 1/(2a_x) - \Delta s_x]$ .<sup>2</sup>

The aperture function  $A \in \mathbb{C}^{N_x N_y}$  is given on this reciprocal-space grid. The transformed, phase-corrected, sample field,  $\tilde{E} \in \mathbb{C}^{N_x M_x N_y M_y}$  is represented on a larger grid of shape  $N_x M_x$  by  $N_y M_y$ . The larger grid in reciprocal space thus corresponds to a super-sampled grid in real space with step-sizes  $a_x/M_x$  and  $a_y/M_y$ .

Each image has an associated 2D shift-vector  $\sigma_p = (\sigma_p^{(x)}, \sigma_p^{(y)})$ . This corresponds to a reciprocal space shift parameter in pixel units:

$$\tilde{\sigma}_p = \left[ \text{round} \left( \sigma_p^{(x)} / \lambda d_1 \Delta q_x \right), \text{round} \left( \sigma_p^{(y)} / \lambda d_1 \Delta q_y \right) \right] \quad (4.41)$$

where the shifts have been rounded to the nearest integer, so that we can treat the shifting of the aperture as a matter of indexing rather than interpolation. We use these shifts to construct a binary matrix for each image (containing only zeros and ones)

$$B_p \in \mathbb{B}^{N_x N_y \times N_x M_x N_y M_y} \quad (4.42)$$

<sup>2</sup>This is valid for  $N_x$  even. When  $N_x$  is odd, the positive Nyquist frequency is also included.

$B_p$  takes the large grid Fourier spectrum  $\tilde{E}$  and returns the part corresponding to the  $p$ 'th shift. After multiplying by the aperture function, the resulting complex vector is called *the view*:  $\psi_p = A \odot (B_p \tilde{E}) \in \mathbb{C}^{N_x \times N_y}$

With all these parameters given, the model can be stated:

$$I_p = \left| U^T A \odot (B_p \tilde{E}) \right|^2 \quad (4.43)$$

where ' $\odot$ ' denotes the Hadamard (element-wise) product and where the inverse DFT has been written as the product with a unitary matrix  $U^T$ . The problem is then the determination of a pair of vectors  $A$  and  $\tilde{E}$ , that simultaneously satisfy the equation for all  $P$  images in the data set. For a single image  $p$ , the model in Eq. (4.43) is under-constrained.  $\tilde{E}$  has  $2N_x M_x N_y M_y$  degrees of freedom while  $I_p$  has only  $N_x N_y$ . The full problem of all the images is an over-determined system when the shifted aperture functions have sufficient overlap.

Figure 4.6 shows examples of some of these quantities from a FP reconstruction and the relations between them.

Here we choose to write the indexing operations and Fourier-transforms as matrix products. This is only done to make the syntax more elegant. When implementing the algorithms for a computer, the products with  $B_p$  will be implemented as an indexing statement and  $U^T$  using FFT-operations.

## 4.5.2 ePIE

One of the first algorithms suggested for solving the ptychographic problem numerically is the Ptychographic Iterative Engine (PIE).[60] Here we treat each image in the data set as a low-dimensional constraint on the higher dimensional space of possible fields. The solution is then found by iteratively projecting an initial guess of  $\tilde{E}$  onto the solution spaces set by each image in the data set until it converges to a solution.

We define an operator  $\mathcal{P}_p\{\cdot\}$  that takes an estimate at the high-resolution sample transform and returns a vector  $\mathcal{P}_p\{\tilde{E}\}$  according to:

$$\begin{aligned} \tilde{\psi}_p &= U^T A \odot (B_p \tilde{E}) \\ \mathcal{P}_p\{\tilde{E}\} &= U \tilde{\psi}_p \odot (\sqrt{I_p} / |\tilde{\psi}_p|) \end{aligned} \quad (4.44)$$

where the forwardslash denotes element-wise division. If any element of  $\tilde{\psi}_p$  is equal to zero, we replace the corresponding element of  $\mathcal{P}_p\{\tilde{E}\}$  with a zero. If we divide out the aperture array and replace the elements of  $\tilde{E}$  with the corresponding elements of  $\mathcal{P}_p\{\tilde{E}\}$ , the result will be an exact solution to Eq. (4.43) for the given image  $p$ . However, doing this for elements of  $A$  with low (or even zero) value would lead to an operation that is highly sensitive to noise in the measurements of  $I_p$ . Therefore we apply a filter that weighs the size of the update depending on the absolute value of  $A$ :

$$\tilde{E}^{(j+1)} = \tilde{E}^{(j)} + \beta B_p^T \frac{|A|}{\max(|A|)} \odot \frac{A^*}{|A|^2 + \alpha} \odot \left( \mathcal{P}_k \left\{ \tilde{E}^{(j)} \right\} - A \odot B_p \tilde{E}^{(j)} \right) \quad (4.45)$$

Here  $\beta$  is a step-size parameter,  $\alpha$  is a small positive number used to avoid divide-by-zero errors, and  $*$  denotes complex conjugation. The product with  $B_p^T$  can be implemented by

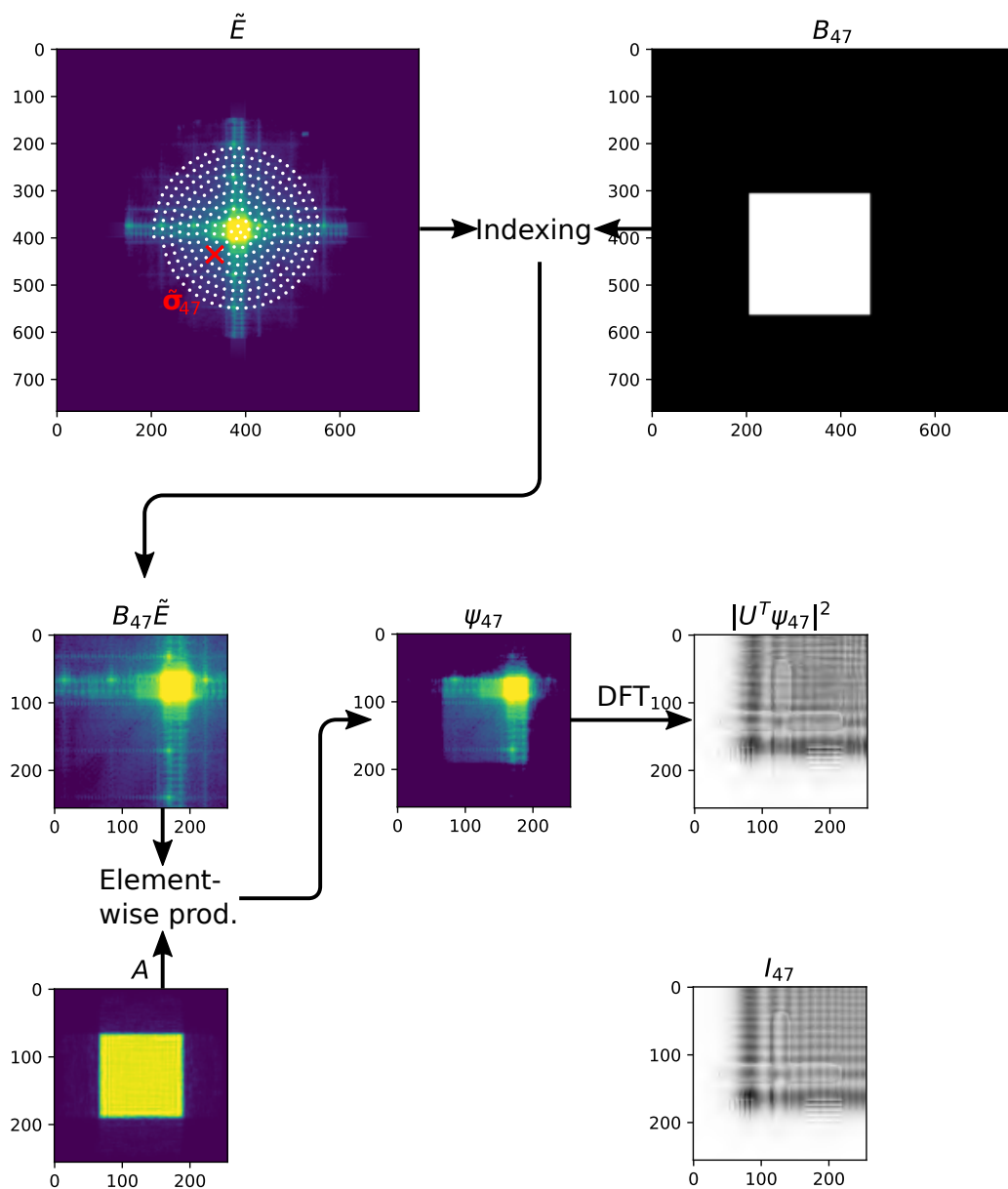


Figure 4.6: Example of different vectors used in Eq. (4.43)

Name	Symbol	Value	Unit
	$N_x$	512	
	$N_y$	512	
Upsampling x	$M_x$	2	
Upsampling y	$M_y$	2	
Working distance	$d_1$	300.0	mm
Demagnified pixel size x	$a_x$	50.0	nm
Demagnified pixel size y	$a_y$	50.0	nm
X-ray wavelength	$\lambda$	0.73	Å

Table 4.1: Table of simulation/reconstruction parameters of the ideal test case.

zero-padding. The factor  $\frac{|A|}{\max(|A|)}$  is a weight function, which ensures that the update will be smaller at points where  $|A|$  is small. This update should be repeated for every image in the data set and this should be repeated until the  $\tilde{E}$  converges to a solution.

An extended version of the algorithm, called ePIE[52], refines both the field and the aperture and the sample simultaneously. The update rule for the field is still Eq (4.45) and at each iteration the aperture is similarly updated according to:

$$A^{(j+1)} = A^{(j)} + \gamma \frac{B_p \tilde{E}^{(j)*}}{|B_p \tilde{E}^{(j)}|^2 + \alpha} \odot \left( \mathcal{P}_k \left\{ \tilde{E}^{(j)} \right\} - A \odot B_p \tilde{E}^{(j)} \right) \quad (4.46)$$

where  $\gamma$  is a step-size parameter.

## 4.6 Examples of FP reconstructions

### 4.6.1 Test case

In this section we perform a number of FP reconstructions of ideal data sets generated with the exact forward model of Equation (4.24). The parameters of the simulated test case are chosen in accordance with the transmission experiment of Section 6.3 and are given in Table 4.1.

The aperture is a square top-hat function of full width 0.1 mm with a small *spherical*-type aberration. The phantom sample is chose to have similar features to the resolution-target sample used in the experiments. It contains fields with dense line-patterns of full-period 0.5  $\mu\text{m}$ , so that the individual lines have width 0.25 $\mu\text{m}$ . The transmission function takes either the value 1 or the value  $0.79 + 0.51i$ , which simulates the contrast of a 650 nm thick layer of tungsten. Furthermore, the phantom sample is padded with zeros to avoid breaking the periodic boundary conditions that are implicitly assumed by DFT methods. Images of the phantom sample and apertures can be seen on the first column of Fig. 4.7.

Figure 4.7 shows the result of reconstructions of the test case using the three different reconstruction algorithms with 90 iterations of each. Aside from the ePIE algorithm presented in the previous subsection we also test the error reduction (ER) and hybrid input-output (HIO) algorithms as they are stated by Thibault.[75] The reconstructions of the sample function succeeds in all three cases, but both the ER and HIO reconstructions contain low-frequency artifacts in the reconstructed phase function that are less evident in the ePIE reconstruction.

Beyond the basic algorithms as they are stated in the previous section, we found that it was beneficial to use a different random ordering of the images between each iterations

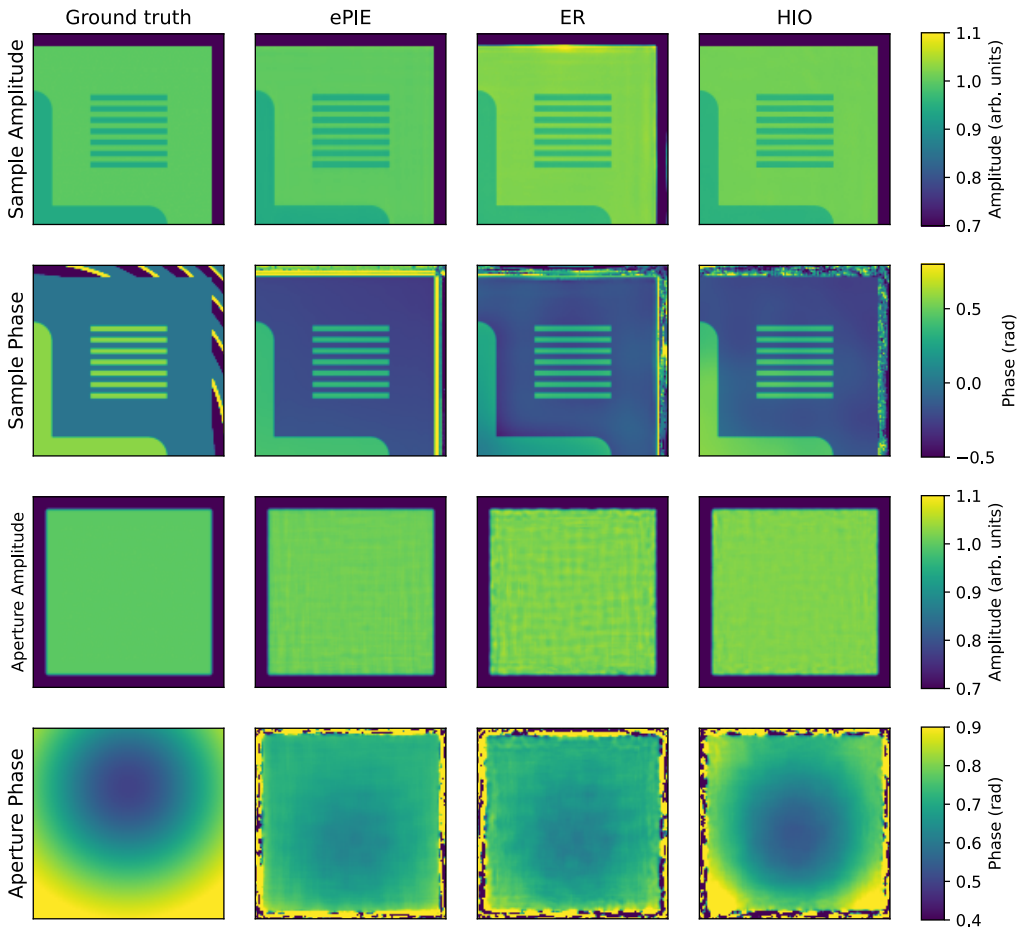


Figure 4.7: FP reconstructions of idea simulated data mirroring the transmission experiment of Section 6.3. The rows contain the amplitude of the reconstructed sample, the phase of the reconstructed sample, the amplitude of the reconstructed aperture and the phase of the reconstructed aperture. The columns contain the ground truth of the simulations, the ePIE reconstruction, the ER reconstruction, and the HIO reconstruction respectively.

in the ePIE algorithm. For the HIO algorithm we use a mask for the aperture function, that sets all values outside a certain region equal to zero as a part of the object projection. This doesn't speed up the convergence, but it prevents a certain type of high-frequency artifact from appearing in early iterations of the reconstructions.

Only the HIO reconstruction succeeds in recovering the spherical aberration in the aperture after 90 iterations. All three methods eventually recover the spherical aberration after many iterations.

### 4.6.2 Error metrics

For FP reconstructions we use a number of metrics to track the convergence of the iterative reconstruction. The first is the update error, which is given by:

$$\mathcal{E}_{\text{Update}} = \begin{cases} \sum_l \left| \tilde{E}^{(j-1)} - \tilde{E}^{(j)} \right|^2 & \text{for ePIE} \\ \sum_p \sum_l \left| \Psi^{(j-1)} - \Psi^{(j)} \right|^2 & \text{for ER and HIO} \end{cases} \quad (4.47)$$

Secondly, the prediction error:

$$\mathcal{E}_{\text{Prediction}} = \frac{1}{P} \sum_p \sum_l \left| I_p - \left| U^T A \odot (B_p \tilde{E}) \right|^2 \right| \quad (4.48)$$

Finally, and only for simulations, the reconstruction error:

$$\mathcal{E}_{\text{Reconstruction}} = \sum_l \left| \tilde{E} - \tilde{E}_{\text{gt}} \right|^2 \quad (4.49)$$

where  $\tilde{E}_{\text{gt}}$  is the "ground truth" used to simulate the images. The reconstruction error cannot be used for real data, where the ground truth is not known. It is also not ideal for simulations due to a number of degeneracies in the FP problem. For example, a shift of the sample may be compensated by a *shift* type aberration in the aperture function to give a perfect solution of the constraints with a different sample vector.

Figure 4.8 shows the convergence of the three FP algorithms measured with three different error metrics. Only the Prediction error is directly comparable between the three figures. The prediction error suggests that the ePIE method has the fastest convergence in the first few iterations but that the HIO algorithm catches up quickly and performs better through iterations 50-400 approximately. After many iterations, the ePIE reconstruction converges exponentially – faster than the two other algorithms – and beats the HIO reconstruction for the remaining iterations.

### 4.6.3 Fourier ring correlation

One of the purposes of FP is to increase the resolution of the reconstruction beyond the Abbe-limit of set by the aperture of the x-ray lens. To see if we reach this goal we want a measure of the resolution of our reconstruction. Fourier ring correlation (FRC) is the standard measure of resolution in the literature. FRC is the correlation of two images as a function of resolution. It is computed by Fourier transforming the two images, separating the spectra in a number of resolution bins based on the amplitude of the spatial frequency (which are *rings* in 2D reciprocal space) and calculating the Pearson correlation coefficient between the Fourier coefficients of the two images for every bin.

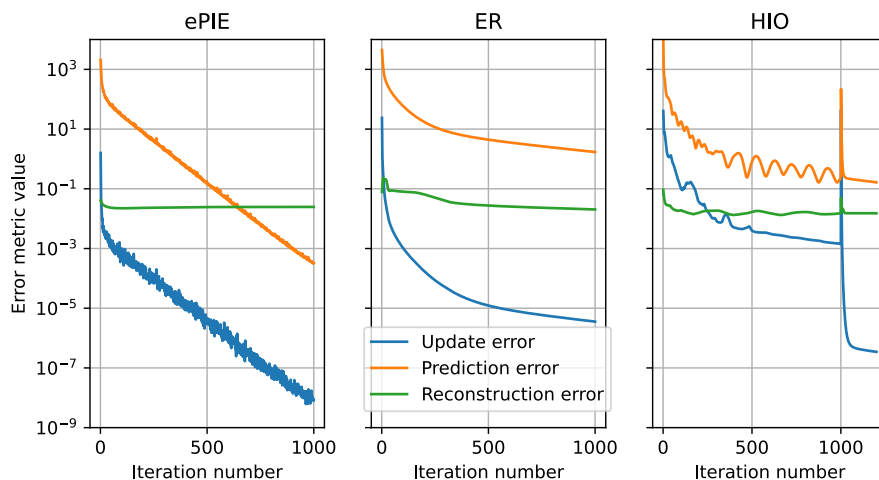


Figure 4.8: Convergence of three different FP algorithms tested on ideal simulated data. The HIO reconstruction starts with 1000 iterations of HIO and applies 200 iterations of ER in the end.

In FP reconstructions the sample array may be shifted, in real or reciprocal space, which is compensated by related modification of the aperture function. This represents a valid FP reconstruction, but the FRC calculated between such a reconstruction and the ground truth would show a low resolution. To avoid making this error, it is important that the two arrays are registered to each other before the FRC is calculated.

We have also found that it is necessary to multiply the images by a window-function in real-space. If this isn't done, the reconstruction will appear to have a higher resolution than they really have. When we calculate the FRC, we will have to decide if we divide out the quadratic phase term beforehand. The quadratic phase term effectively shifts the Fourier spectrum of the sample in points away from the optical axis. Keeping the quadratic phase term will therefore sometimes give a higher FRC value at high resolution.

Figure 4.9 show the FRC between three different reconstructions and the ground truth. We see that the FRC is close to one all the way to the resolution limit set by the range in reciprocal space covered by the scan and sharply falls off to zero outside this range.

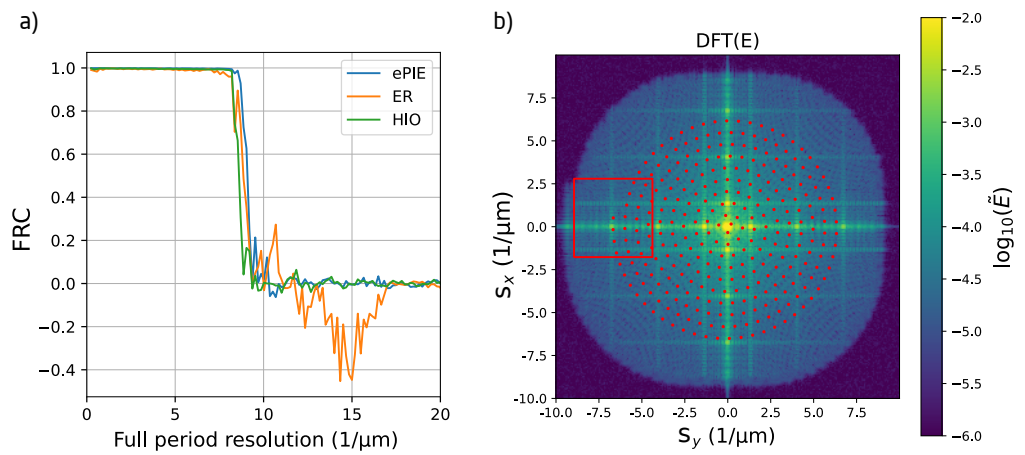


Figure 4.9: a) FRC between the ground truth and different FP reconstructions with ideal simulated data. b) Fourier transform of reconstruction with 900 iterations of ePIE after dividing out the quadratic phase term. The red dots mark the values of  $\tilde{\sigma}$  used in the simulation. The red square marks the extent of the aperture function for the last image in the data set.



# 5 Aberrated compound refractive lenses

The phase-microscopy methods introduced in the previous chapter both rely on the simple model of a coherent microscope given by Eq. (4.28). This equation uses the thin lens approximation for the objective lens. The compound refractive lenses (CRL) which is used as an objective lens in the experiments has a length of approximately 10 cm compared to a focal length of around 30 cm. It is well established in the literature [43, 67] that the thin-lens approximation makes an error on the value of the focal length of around 2 cm, but aside from this can be treated as a thin lens. [56]

These prior treatments, however do not consider errors in the individual lenses used to make the CRL. When aberrated CRLs have been investigated in the literature, [15, 51] they have typically only been considered as focusing optics and not as an objective lens. In this chapter we show how to simulate aberrated CRLs and investigate how the thick-lens behavior then impacts the images in a coherent microscope.

The chapter starts with the thin-lens approximation then we derive a theoretical framework for simulating CRLs based on the existing literature. [56, 19] Finally we simulate a CRL with parameters matching those of the experiment and investigate the impact of aberrations.

## 5.1 CRLs in the thin lens approximation

The CRL is one of a few types of lenses available at hard x-ray wavelengths. It operates on the same principle as normal visible light lenses which use the refractive properties of bulk matter to modify the wave-front of the light-field. Unlike at visible light wavelengths, the refractive index of matter at hard x-ray wavelengths is less than one, which means refractive focusing x-ray lenses have concave surfaces instead of the convex surfaces seen in visible light focusing lenses. It is conventional to introduce two real parameters,  $\delta$  and  $\beta$ , to describe the complex refractive index,  $n$ .

$$n = 1 - \delta + i\beta \quad (5.1)$$

$\delta$  is a small positive number describing the refracting properties of the material and  $\beta$  describes the absorption. They are both related to the electric susceptibility,  $\chi_0$ , through:

$$\begin{aligned} n &= \sqrt{1 + \chi_0} \\ \Rightarrow \delta &\approx -\text{Re}(\chi_0)/2 \\ \beta &\approx \text{Im}(\chi_0)/2 \end{aligned} \quad (5.2)$$

CRLs are usually constructed from light materials such as Be, Al, diamond, and plastics because these materials have the lowest absorption. At a photon energy of 17 keV, which is a typical wavelength for DFXM, beryllium has  $\delta = 1.2 \cdot 10^{-6}$  and  $\beta = 2.4 \cdot 10^{-10}$ .

We can calculate the transmission function of a biconcave parabolic x-ray lens (sketched in Fig. 5.1) in the projection approximation. For a symmetric parabola the x- and y-

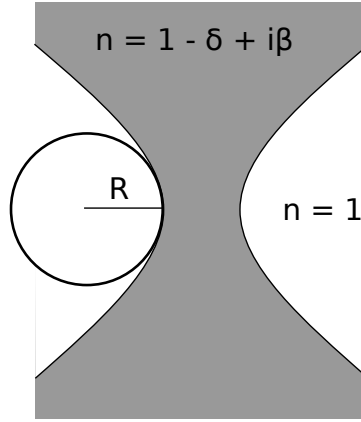


Figure 5.1: Sketch of single biconcave x-ray lens.

dependence of the transmission function simply factorizes, so we continue with only the x-dependence:

$$\begin{aligned}
 T_{\text{single lens}} &= \exp\left(i \frac{k(-\delta)x^2}{R}\right) \exp\left(i \frac{ki\beta x^2}{R}\right) \\
 &= \exp\left(-i \frac{\pi x^2}{\lambda f}\right) \exp\left(-\frac{x^2}{2\sigma_{\text{Abs}}^2}\right)
 \end{aligned} \tag{5.3}$$

The first factor is an ideal-lens term and the second factor is a Gaussian shaped absorbing aperture. In the last line, we have defined the focal length and the characteristic width of the aperture:

$$f = \frac{R}{2\delta} \quad \text{and} \quad \sigma_{\text{Abs}} = \sqrt{\frac{R\lambda}{\pi\beta}} \tag{5.4}$$

At 17 keV photon energy, a single beryllium lens with apex curvature 50 $\mu\text{m}$  has  $f \approx 20\text{m}$  and  $\sigma_{\text{Abs}} \approx 2\text{mm}$ . This focal length of 20m is too long to be practically used as an objective lens. A CRL therefore consists of many such lenses placed closely after one another on a common axis. If we treat this construction in the projection approximation we would get:

$$T_{\text{CRL}} = (T_{\text{single lens}})^N \tag{5.5}$$

where  $N$  is the number of lenses. This gives:

$$f_N = \frac{f}{N} \quad \text{and} \quad \sigma_{\text{Abs,N}} = \frac{\sigma_{\text{Abs}}}{\sqrt{N}} \tag{5.6}$$

This approximation is not sufficient for CRLs. By using this approximation we will make an error on  $f_N$  on the order of the physical length of the whole CRL. In fact there is no one number,  $f$ , that we can assign to a CRL, which would make the thin-lens focus condition Eq. (4.19) true in general. We therefore say that the CRL behaves as a *thick lens*.

## 5.2 The quadratic-phase propagator

In order to investigate the thick-lens behaviour of CRLs, we would like to treat them in a *multislice* approach where each individual lens is treated in the projection-approximation and a free-space propagator is used between each lens. If we try to do this numerically using Eq. (4.23), it will turn out that the large quadratic phase factor that is accumulated after successively propagating through all the lenses will be very quickly varying at the edges of the FOV and therefore, in order to over sample this function, we would need to use a very fine computational grid that would be impractical for numerical simulation.

Instead we use a new paraxial propagator that divides out the quadratic phases from the lenses and handles the propagation of these analytically. In order to do so we have to allow the grid, on which the complex envelope is given, to expand and contract from slice to slice in the calculation. In this section we derive this special propagator and a few analytical results, that are useful for calculating the properties of CRLs.

This new propagator has been used by a number of authors in the past.[19, 15] The *fractional Fourier transform*-approach[55] used to treat CRLs by Pedersen[56] is apparently a more general method than the propagator given by Chubar[19], but Pedersen only uses a subset of the *fractional Fourier transforms* that are easy to calculate numerically. This subset is the same as the propagators given by Chubar. Since the notation and derivations of the fractional Fourier transforms are not easy to follow, we will give a brief derivation here which is similar to the treatment by Chubar.

First we define the notation:

$$F(x; z, R, a) = \sqrt{a}E(ax; z)e^{-ix^2/(\lambda R)} \quad (5.7)$$

where we will choose  $R$  to cancel out any quadratic phase in a given the wave-front and  $a$  is a scaling parameter that will determine the expansion/contraction of the grid. We start from the Fresnel integral as it is stated in Eq. (4.11) and introduce our  $F$ -notation on the LHS to absorb one of quadratic the phase-factors:

$$F(x; R + z_0, R, 1) = \frac{\phi}{(i\lambda R)^{1/2}} \int dx' e^{-i2\pi xx'/(\lambda R)} e^{i\pi x'^2/(\lambda R)} E(x'; z_0) \quad (5.8)$$

where  $\phi$  is a constant phase factor which we ignore from here on. For another length  $(R + z)$  we also write up the Fresnel integral. This time without using the “ $F$ -notation”:

$$E(x; R + z + z_0) = \exp \left[ \frac{i\pi x^2}{\lambda(R + z)} \right] \frac{\phi}{(i\lambda(R + z))^{1/2}} \int dx' \exp \left[ \frac{-i2\pi xx'}{\lambda(R + z)} \right] \exp \left[ \frac{i\pi x'^2}{\lambda(R + z)} \right] E(x'; z_0) \quad (5.9)$$

We want to eliminate  $E(x'; z_0)$  from these two equations to get an expression, which works as a propagator between the new  $F$ -functions.

In equation (5.8) we substitute the integration variable  $s' = x'/\lambda R$ , multiply by  $\exp(i2\pi sx)$ , and integrate over  $x$ .

$$\begin{aligned} \int dx e^{i2\pi s x} F(x; R + z_0, R, 1) \\ = \frac{\phi \lambda R}{(i\lambda R)^{1/2}} \int dx e^{i2\pi s x} \int ds' e^{-i2\pi s' x} e^{i\pi s'^2 \lambda R} E(s' \lambda R; z_0) \end{aligned} \quad (5.10)$$

The integral over  $x$  on the RHS evaluates to a Dirac-delta function, which will lift the  $s'$  integral to give:

$$\begin{aligned} \int dx e^{i2\pi s x} F(x; R + z_0, R, 1) &= \frac{\phi \lambda R}{(i\lambda R)^{1/2}} e^{i\pi s^2 \lambda R} E(s \lambda R; z_0) \\ \Leftrightarrow E(s \lambda R; z_0) &= \frac{(i\lambda R)^{1/2}}{\phi \lambda R} e^{-i\pi s^2 \lambda R} \int dx e^{i2\pi s x} F(x; R + z_0, R, 1) \end{aligned} \quad (5.11)$$

Now in equation (5.9), we change the integration variable to  $s = x'/\lambda R$ :

$$\begin{aligned} E(x; R + z + z_0) &= \frac{\lambda R}{(\lambda(R + z))^{1/2}} \exp \left[ \frac{i\pi x^2}{\lambda(R + z)} \right] \\ &\times \int ds \exp \left[ -i2\pi x s \frac{R}{R + z} \right] \exp \left[ i\pi s^2 \lambda \frac{R^2}{(R + z)} \right] E(s \lambda R; z_0) \end{aligned} \quad (5.12)$$

Now plugging equation (5.11) into equation (5.12) and simplifying some fractions, we get:

$$\begin{aligned} E(x; R + z + z_0) &= \sqrt{\frac{R}{R + z}} \exp \left[ \frac{i\pi x^2}{\lambda(R + z)} \right] \int ds \exp \left[ -i2\pi x s \frac{R}{R + z} \right] \exp \left[ -i\pi s^2 \lambda \frac{Rz}{(R + z)} \right] \\ &\times \int dx' e^{i2\pi s x'} F(x'; R + z_0, R, 1) \end{aligned} \quad (5.13)$$

This has the shape of a Fourier-convolution with a chirp-function except for the inconvenient factor of  $\frac{R}{R+z}$  in the inverse Fourier transform. We get rid of this by one last scaling of a variable:  $x'' = x \frac{R}{R+z} = a^{-1}x$  after which we can write:

$$\begin{aligned} E(ax''; R + z + z_0) \\ = 1/\sqrt{a} \exp \left[ \frac{i\pi (ax'')^2}{\lambda(R + z)} \right] \mathcal{F}^{-1} \left\{ \exp \left[ \frac{i\pi s^2 \lambda R z}{(R + z)} \right] \mathcal{F} \{ F(x'; R + z_0, R, 1) \} \right\} \end{aligned} \quad (5.14)$$

Now we can introduce our  $F$  notation on the LHS and use this to absorb the pre-factors on the RHS.  $z_0$  was an arbitrary origin to begin with, so we choose  $z_0 = -R$  to make the result look nicer.

$$F\left(x; z, R+z, \frac{R+z}{R}\right) = \mathcal{F}^{-1}\left\{\exp\left[\frac{i\pi s^2 \lambda R z}{(R+z)}\right] \mathcal{F}\{F(x; 0, R, 1)\}\right\} \quad (5.15)$$

Equation (5.15) defines a new paraxial Fourier propagator that can be implemented with normal discrete Fourier transform approaches. The chirp function will, for the cases we are interested in, typically be well-sampled. In the case of  $R \rightarrow \infty$ , we recover the normal propagator from Eq. (4.8).

The benefit of these scaled functions is that we can symbolically multiply by a perfect lens term by changing the  $R$ -parameter, which means we have lifted the requirement to sample these quickly varying phases.

When the CRL consists of perfect lenses, the calculation is a series of successive convolutions with these chirp terms, which may be written instead as a single convolution of a combined chirp by making use of some properties of this chirp and its Fourier transform. Without carrying out this calculation we can simply notice that the propagator only modifies the **phases** in the Fourier-space and not the **amplitudes**. This means that the ideal CRL (one consisting of perfect lenses) will create a perfect image of the intensity in the sample plane. When the absorbing apertures of the lenses are taken into account, this treatment no longer works and we have to do one convolution per lens to calculate the resulting images.

### 5.2.1 Analytical rules for cascading lenses

As was mentioned in the last subsection, the multiplication by a perfect lens term is handled exactly by changing the  $R$  parameter according to:

$$\begin{aligned} F(x; z, R, a) \exp\left(\frac{i\pi x^2}{\lambda f}\right) &= \sqrt{a} E(ax; z) \exp\left(-i\frac{x^2}{\lambda R}\right) \exp\left(\frac{i\pi x^2}{\lambda f}\right) \\ &= F\left(x; z, \frac{Rf}{f-R}, a\right) \end{aligned} \quad (5.16)$$

which means a perfect lens term, in the calculation, is handled by changing the parameters according to the update rule:

$$\begin{aligned} R_{n+1} &= \frac{R_n f}{f - R_n} \\ a_{n+1} &= a_n \end{aligned} \quad (5.17)$$

We can also write up a rule for free-space propagation by a distance  $z$ :

$$\begin{aligned} R_{n+1} &= R_n + z \\ a_{n+1} &= a_n \frac{R_n}{R_n + z} \end{aligned} \quad (5.18)$$

This gives us an iterative approach to calculating the focus condition of the CRLs without needing to do any heavy calculations. The procedure is as follows:

1. Start at the sample-plane with  $R = 0$
2. Propagate to the first lens, changing  $R = p$  according to Eq. 5.18 and set  $a = 1$ .
3. For each lens in the CRL propagate between the lenses using Eq. (5.18) and through the lenses using (5.17)
4. After the final lens, if  $R$  is negative, there will be a focused image at the distance  $q = -R$  from the last lens. The magnification is  $M = -ap/q$  where  $a$  is the value of  $a$  at the last lens.

See fig 5.3 for a sketch of the geometry.

The iterative rules given in (5.18) and (5.17) can be used to calculate the focusing condition of a CRL for a given geometry and focal length of the individual lenses. This method unfortunately does not yield short analytical expressions but it can readily be used for numerical calculations. The algorithm outlined here allows one to quickly calculate the distance to the focus plane for any given sample-to-lens distance. More often, we are interested in finding the magnification and in-focus lens position for a fixed sample-to-detector distance. This is achieved using a root finding algorithm.

### Focusing condition of a realistic CRL

For verification, we plug in a set of typical values used in the ID06 microscope and compare with experimental values and other approximate results. (Fig 5.2) If we consider only *homogeneous* CRLs, by which we mean a CRL made up of identical lenses equally spaced through its entire length, a number of analytical results are available. An approximation given by Kohn[43] states that a homogeneous CRL consisting of  $N$  lenses at a distance  $T$  apart can be treated as a thin lens – placed at the center of the CRL – with focal length:

$$f_{\text{CRL}} = f/N + NT/6 \quad (5.19)$$

The problem of the basic homogeneous CRL was also treated in a ray-tracing setting by Simons[67] who states two different results. One exact using trigonometric functions, which gives the same result as the iterative procedure outlined in Eq.(5.17) down to numerical error and an approximate result valid in the limit of thin lenses, which is the same result as the simple thin-lens approach given by Eq. (5.6).

With the normal parameters of the ID06 microscope, the thin lens approximation overestimates the magnification by about 10% compared to the cascaded lenses result while the approximation by Kohn only overestimates the magnification by 0.2%. The experimentally measured magnification follows the expected trend, but are about 5% higher than predicted by theory. This deviation is thought to be due to production errors that increase the actual radius of curvature.

When we have the magnification of the CRL in the focusing condition in a given geometry, we can define an effective thin lens and an effective focal length. The effective thin lens is one which, if placed at the effective thin lens plane, would create an image with the same magnification as the CRL. The position and focal length of such a lens is uniquely determined by the two equations (4.15) and (4.19). Figure 5.3 sketches the geometry of the CRL in focusing condition and defines a number of distances.

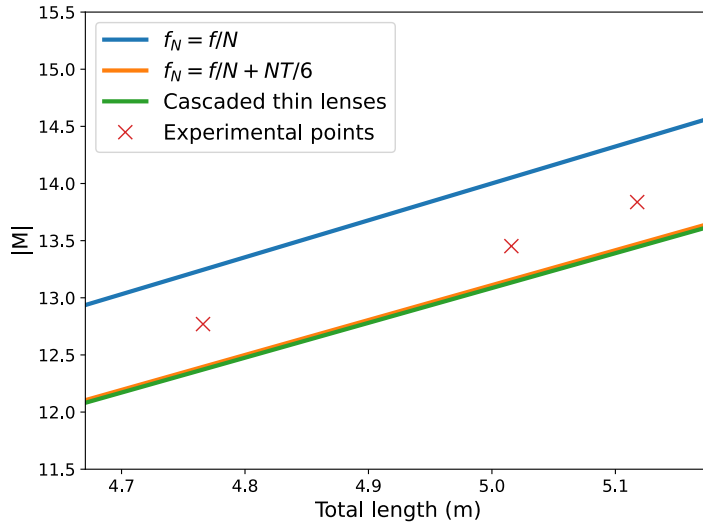


Figure 5.2: Magnification of a CRL as a function of total length along the optical axis calculated in three different approximations. Parameters used were:  $N = 68$ ,  $\lambda = 0.73\text{\AA}$ ,  $R = 0.05\text{mm}$ ,  $T = 1.6\text{mm}$ , and  $\delta = 1.18 \cdot 10^{-6}$ . The experimental magnifications were calculated as the ratio of effective pixel-sizes found by scanning the sample and detector position respectively. The experimental values were calculated from three different experiments done in the same week in February 2021 with the same horizontal sample-to-detector distance but at three different  $2\theta$  angles.

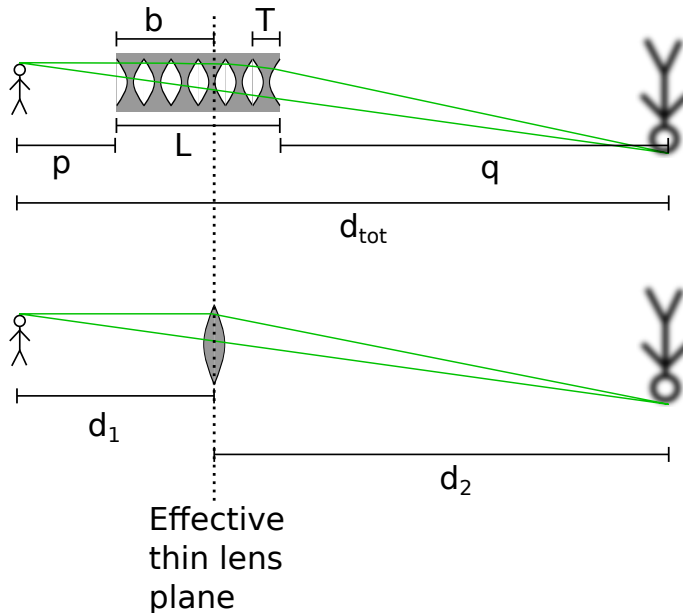


Figure 5.3: Sketch of a CRL in the focusing condition and the *effective thin lens* that gives rise to the same image in a given configuration.

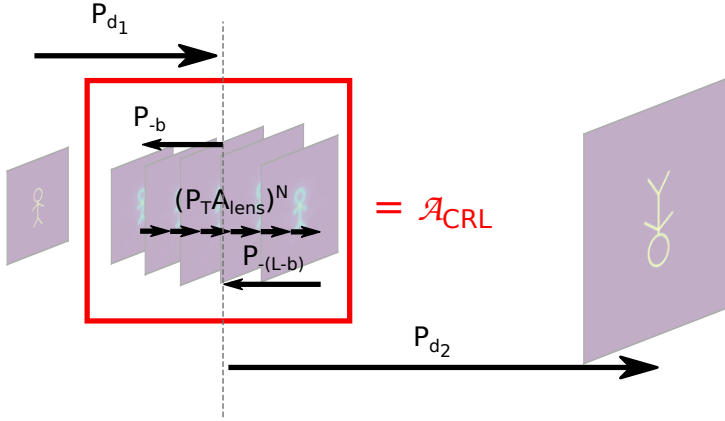


Figure 5.4: Sketch of the computational approach taken to simulate the effective aperture.

### 5.3 Effective apertures

The formulation of Fourier ptychography was based on the coherent model of a microscope defined by Eq. (4.28), where the intensity image is given by the absolute square of the convolution of a pair of complex-valued functions. The multislice model of a CRL, that we have presented in this chapter, does not have that form. Therefore one has to ask whether FP is an appropriate technique for treating images captured in a CRL-based microscope.

To investigate this, we want an approach to simulate the images in a CRL-based microscope similar to Eq.(4.28). We introduce the operator,  $\mathcal{A}_{CRL}$ , which is a combination of propagators that first back-propagates a wave-front from the effective thin lens plane to the position of the first lens, then propagates the field through the lenses one by one, and finally back propagates the field to the original plane. The approach is sketched in Fig. 5.4. With this operator, we can write the imaging-operation of the CRL-microscope as:

$$|E(Mx, My, d_1 + d_2)|^2 = \frac{d_1}{d_2} \left| \mathcal{F}^{-1} \left\{ \mathcal{A}_{CRL} \left\{ \mathcal{F} \left\{ \exp \left[ \frac{i\pi(x^2 + y^2)}{\lambda d_1} \right] E(x, y, 0) \right\} \right\} \right\} \right|^2 \quad (5.20)$$

Because all the propagators and lenses used to construct  $\mathcal{A}_{CRL}$  are represented by linear operators,  $\mathcal{A}_{CRL}$  is also a linear operator. If we find that this operator is well approximated, under certain reasonable conditions, by a simple product. That is:

$$\mathcal{A}_{CRL} \{E(x, y)\} \approx A_{CRL}(x, y)E(x, y) \quad (5.21)$$

then Eq. (5.20) reduces to Eq. (4.16) and we have found a thin-lens approximation of the CRL. To investigate this operator, we perform numerical calculations using the quadratic-phase propagator given in (5.15). For this particular choice of parameters, the successive application of the quadratic-phase propagators will lead to a total change of the  $R$  parameter from  $d_1$  in the input to  $-d_2$  at the output and the  $a$  parameter will be unchanged. This means the field is given on the same grid at the input and the output

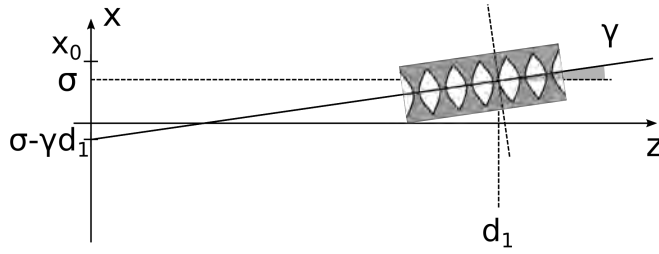


Figure 5.5: Misalignment of the CRL.  $\sigma$  is the distance from the  $z$ -axis to the center of the CRL.  $\gamma$  is the angle of CRL relative to the  $z$ -axis, and  $x_0$  is the coordinate of a given point-of-interest in the sample-plane.

and the approximate aperture function for a given input field,  $E_{\text{test}}(x, y)$ , can be calculated as:

$$A_{\text{CRL}}(x, y) = \mathcal{A}_{\text{CRL}}\{E_{\text{test}}(x, y)\} / E_{\text{test}}(x, y) \quad (5.22)$$

Where we can use the discretized components of  $E_{\text{test}}$  without the need of any interpolation. As test functions, we will use narrow Gaussians in the sample plane that have a large enough divergence to fill the aperture of the CRL. By scanning the position of this Gaussian around in the field of view, we will get different position-dependent effective apertures. These will vary systematically as a function of the position and be approximately identical within a local area, which we can then treat with a single effective aperture. The notion of a FOV dependent aberration function is often used in computational microscopy at visible light wavelengths.[88]

Moving the test function is naturally equivalent to shifting the position of the lens by the same distance in the opposite direction. Furthermore, if the lens is rotated by a small angle  $\gamma$  and if we can ignore effects that are second order and higher in the rotation angle, the rotation has the same effect as shifting the sample by a distance  $-\gamma d_1$ . (see Fig. 5.5) The FOV dependent aperture function should thus only depend on the quantity:  $x_0 - \sigma + \gamma d_1$ , which is the distance in the sample plane from the optical axis of the CRL to the point of interest in the sample.

### 5.3.1 A CRL containing an absorbing aperture

We would like to limit the aperture of our CRL-lenses to get a hard transition from the bright- to the dark field and to limit the effect of aberrations in the off-axis part of the lenses. We do this by inserting an absorbing aperture at some point in the CRL. We are then faced with a simple question with practical consequences: at what position in the lens should we place this aperture?

To answer this question we calculate the on-axis effective aperture for a series of such CRLs in a magnifying geometry and compare the resulting curves. Figure 5.6 a) shows a number of these calculated curves. We see that for a general position of the aperture, the effective aperture function does not go sharply to zero, as we want, but has tail. For the particular choice of placing the aperture after the 38th lens, the size of this tail is minimized. This position is close to, but not exactly the same as the effective thin lens plane (Fig. 5.6 b).

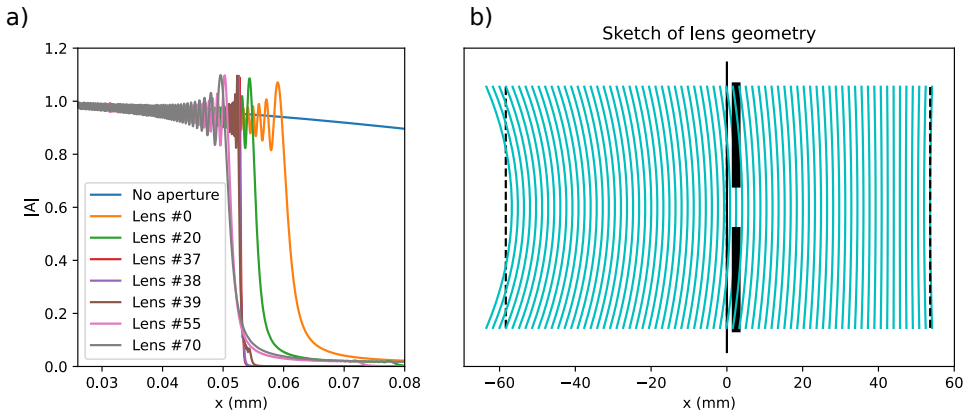


Figure 5.6: a) Calculated effective aperture functions for a CRL consisting of 70 individual Beryllium lenses with  $\lambda = 0.73\text{\AA}$ ,  $R = 0.05\text{mm}$ ,  $T = 1.6\text{mm}$ , and  $\delta = 1.18 \cdot 10^{-6}$ . The CRL is modified with a top hat absorbing aperture of full width 0.1mm. The placement of this aperture is varied between the curves and the position of the aperture is given in the legend. b) A sketch of the geometry of the CRL with an aperture placed directly after the 38th lens.

We see (Fig. 5.7) that placing the aperture at this position also leads to an effective aperture, that is less dependent on the position of the test-function relative to the optical axis than in would be for a general choice of this position. This means it behaves more like a thin lens than otherwise.

To see if the thick-lens effects are important for the stability of FP reconstructions, we simulate three FP data sets with a model of a CRL with a square aperture. One using the thin lens approximation, ie. the same forward model as used in the reconstruction. One using the cascaded lenses approach and with the aperture placed at the end of the lens-stack. And finally one with the aperture placed at the "ideal" position at the 38th lens. Figure 5.8 shows the phase of FP reconstructions made from simulated images using each of these three lens models. We see that the reconstruction using an aperture at the end of the CRL has a large low-frequency error in the reconstructed phase. Both the thin lens reconstruction and the thick lens reconstruction, with the aperture at the optimal plane make reconstructions of similar quality.

## 5.4 Aberrated lenses

In practice, we observe that the lenses in our CRLs have strong high-frequency aberrations. When the sample is coherently illuminated, these aberrations cause strong speckle-like noise in the images.

When the lenses are aberrated, we can still assign an effective aperture using Eq.(5.22) but now it is unavoidable that this effective aperture varies with the position in the FOV because the aberrations are spread out in the entire length of the CRL. There is no way to avoid inherent thick-lens behavior of the lenses.

There is a simple geometric interpretation of this issue illustrated in Fig. 5.9, where we have made a toy-model of an aberrated lens containing aberrations only at the first and last lenses with recognizable geometric shapes. The calculated effective aperture ap-

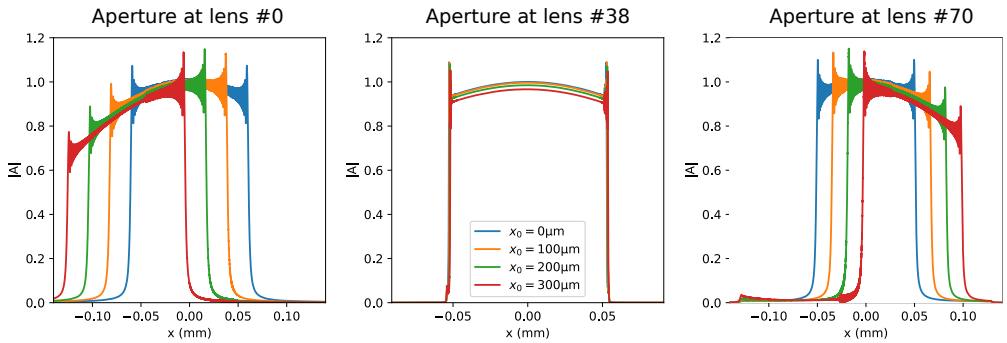


Figure 5.7: Calculated effective aperture functions for a CRL consisting of 70 individual Beryllium lenses with  $\lambda = 0.73\text{\AA}$ ,  $R = 0.05\text{mm}$ ,  $T = 1.6\text{mm}$ , and  $\delta = 1.18 \cdot 10^{-6}$ . The CRL is modified with a top hat absorbing aperture of full width 0.1mm a) placed before the first lens, b) after the 38th lens, and c) after the last lens respectively. The figure shows a number of calculated aperture functions with the a test-function placed at different distances from the optical axis.

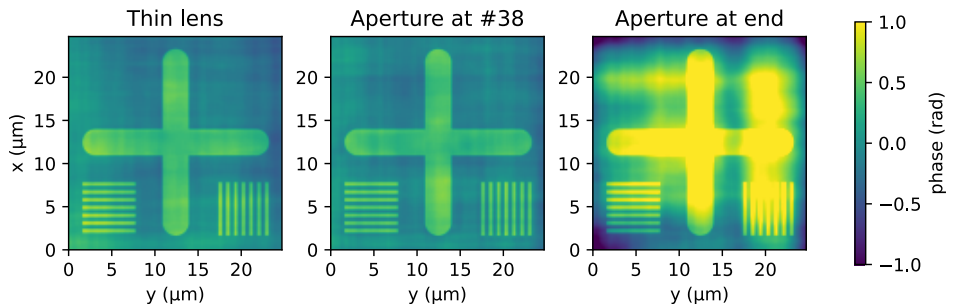


Figure 5.8: FP reconstructions of simulated data sets using 3 different models of the lens. One is the thin-lens approximation, one is a thick lens, with an aperture at the optimal position, and the last is a thick lens with the aperture at the last lens in the CRL.

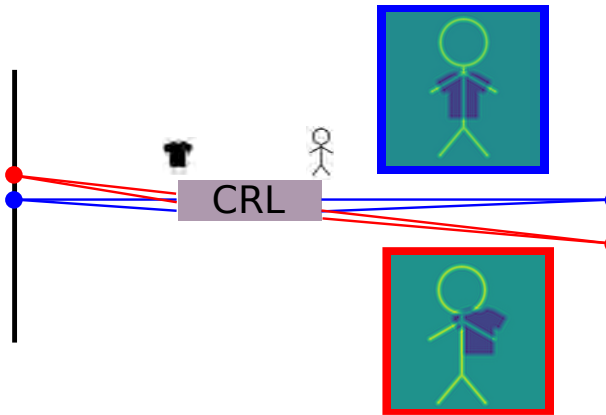


Figure 5.9: Calculated effective thin-lens apertures for two different positions in the FOV showing the importance of thick-lens effects in aberrated CRLs. The aberrations are located at the first and last lens of the CRL to highlight the geometric origin of the thick lens effects. Reconstructions were made using 50 iterations of the ePIE algorithm.

appears to be a sum of the two individual aberrations (respectively over- and underfocused) but depending on the position of the test-function, the two images are offset by some distance relative to each other which may be understood in terms of the parallax displacement.

The aperture functions that we reconstruct using FP should also re-create this shifting of features in the aperture as a function of position on the FOV. We simulate a data-set using the same toy-model of an aberrated CRL displayed in Fig. 5.9. From this data set a number of FP reconstructions were computed using different 512x512 pixel regions of the same images. In the refined aperture functions, the thick-lens behavior is clearly visible by a shift of the two different aberration-features relative to each other. The reconstructed sample arrays are of high quality and show that the reconstructions succeed up to the full resolution covered by the scan but the reconstructed aperture arrays contain strong noise.

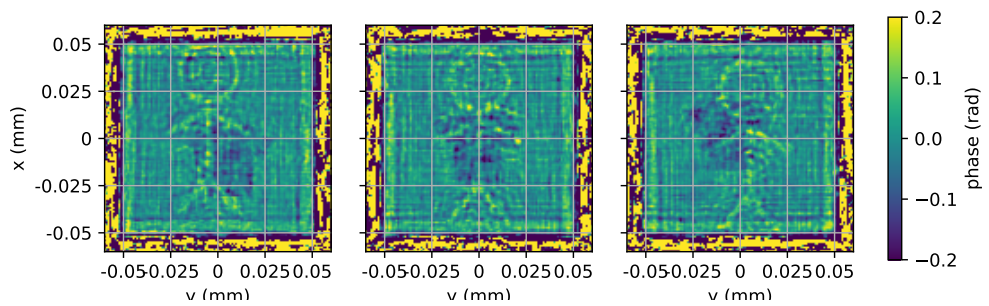


Figure 5.10: Reconstructed effective aperture function made with FP. The images were simulated using a thick CRL with aberration function placed at the position of the first and the last lens respectively. The three reconstructions were made using data from three different regions of the images. Reconstructions were made with 60 iterations of HIO and 10 iterations of error reduction.



# 6 Implementing Fourier ptychography in an X-ray microscope

Both DFXM and FP are microscopy techniques that measure a stack of band-pass filtered real-space images where the filter is displaced in reciprocal space between each image. In DFXM this is partly achieved by rotating the sample but it may also be achieved by translating the objective lens. FP is typically done with a shifting angle of illumination, but has also been demonstrated with a moving lens.[80] We therefore want to investigate whether we can apply the FP data treatment for DFXM data?

This chapter describes a number of FP experiments performed in the ID06-HXM microscope at the ESRF. First a transmission experiment meant as a test of the implementations and then a thin-film Bragg-diffraction experiment.

## 6.1 Experimental description

### 6.1.1 Instrumentation

The experiments that were performed in connection with this thesis were carried out at the ID06-Hard X-ray Microscope(ID06-HXM) at the European Synchrotron Radiation Facility (ESRF).

A hard x-ray microscope, typically operating between 15keV and 32keV, based on CRLs in a full field imaging geometry. The most unique feature of this instrument is a pair of large gantries, with range of movement of several meters and high precision, that are used to place the objective lens and detector in the path of a Bragg-reflected beam at angles away from the incident beam direction of up to 22°. This great range of movement of both the objective lens and the detector allows DFXM and transmission experiments to be carried out using the same set of lenses and detectors without re-mounting any components between experiments.[46]

The ID06-HXM uses a U18 cryogenic permanent magnet in-vacuum undulator. For the experiments presented here we use a photon energy of 17keV which is accessible with the first harmonic of the undulator.

The beam is monochromatized by a symmetric Si(111) double crystal monochromator located at 35.8 m downstream of the source. The monochromatic beam has a relative bandwidth of approximately  $\Delta E/E = 10^{-4}$

The experiments were carried out in 2020-2021, after an upgrade of the ESRF storage ring called *Extremely Brilliant Source*(EBS). After this upgrade the transverse size of the electron beam was reduced giving increased brilliance of the x-ray sources but more importantly for this work, the effective source-size of the x-ray source was decreased, which gives a more coherent beam at the microscope. [25]

Between the source and the sample we further have the option to insert a *decoherer* consisting of a spinning disc of amorphous carbon. This acts as a random diffuser and due to the fast spinning, the diffuser varies on a timescale much shorter than the exposure time of the detector, effectively making the incident light less coherent.

In the slicing mode of DFXM, we insert a 1D focusing lens called the condenser lens approximately 1 m upstream of the sample that focuses the incident radiation onto a horizontal line at the sample position. At the lower end of the energy spectrum used at the beamline, the condenser lens is a CRL consisting of 58 individual Be lenses of apex-curvature 100  $\mu\text{m}$ .

The sample goniometer consists of a number of translation and rotation stages. For the FP-experiments presented here, it is only used to place and orient the sample in the beam, not actively as a part of the scanning.

The objective lens is placed on a gantry allowing for accurate positioning of the lens in three dimension ( $\text{obx}$ ,  $\text{oby}$ ,  $\text{obz}$ ) as well as two rotation stages named  $\text{obpitch}$  and  $\text{obyaw}$  that rotate the lens around the  $y$ - and  $z$  axis respectively. The objective lens has a working distance of  $\approx 250$  cm from the sample to the nearest lens in the CRL.

The detector is positioned on a separate gantry at a fixed position in  $x = 4776$  mm but can be moved in the  $z$  and  $y$  directions by the motors  $\text{ffz}$  and  $\text{ffy}$ . The detector is an indirect scintillator detector using a 10x objective lens to reach an effective pixel-size of 0.71  $\mu\text{m}$ .

### 6.1.2 Experimental procedure

The FP scans were implemented by two coupled movements of the objective lens position, orientation and detector position effectively giving a complete rotation of the imaging optics around the position of the sample by small angles on the order of  $10^{-3}$  rad.

Initially, the lens was centered on and aligned with the beam in transmission mode by maximizing the flux through the lens as measured by an ionization chamber placed at its exit. Then the detector was brought into the center of the beam. After this the objective lens is moved along its optical axis to bring the sample into focus while the sample is moved perpendicular to the optical axis to bring the feature of interest into the center of the FOV. Finding focus position is difficult due to the coherent nature of the microscope and the fact that the sample provides stronger phase- than absorption contrast, leading to a maximum of image intensity variation at some small defocus distance.

When the sample is in focus, the effective magnification of the microscope is measured by translating the sample perpendicular to the optical axis and tracking sample features across the detector. This was done for each sample using an automated registration procedure to yield the shift in pixels between each image. When possible, the pixel size was compared with known features of the sample and typically we get an agreement between the found pixel sizes on two significant digits. As discussed earlier, the measured magnification size was typically 5% smaller than the one expected by theory. (Fig. 5.2)

We parameterize the movements of the lens and detector by the equivalent real-space shift of the thin-lens aperture function:  $\sigma_x$  and  $\sigma_y$  as in Eq. 4.27. The implementation of the  $\sigma_x$ -scan is identical to the normal implementation of  $\Delta 2\theta$ -scans in traditional DFXM. The physical movements are described by:

$$\begin{bmatrix} \Delta\text{obz} \\ \Delta\text{obpitch} \\ \Delta\text{ffz} \end{bmatrix} = \sigma_x \begin{bmatrix} 1/\text{mm} \\ 180/\pi d_1 \\ |M + 1|/\text{mm} \end{bmatrix} \quad \text{and} \quad \begin{bmatrix} \Delta\text{oby} \\ \Delta\text{obyaw} \\ \Delta\text{ffy} \end{bmatrix} = \sigma_y \begin{bmatrix} 1/\text{mm} \\ 180/\pi d_1 \\ |M + 1|/\text{mm} \end{bmatrix} \quad (6.1)$$

where  $\Delta\text{obz}$  and  $\Delta\text{oby}$  are the increments of the motors controlling the objective lens position,  $\Delta\text{obpitch}$  and  $\Delta\text{obyaw}$  are the increments of the motors controlling the objective

lens angle, and  $\Delta ffz$  and  $\Delta ffy$  are the increments of the motors controlling the detector position.

The magnification is measured as described above and  $d_1$  is calculated from  $M$  and the known sample-to-detector distance using Eq. (4.19). For the FP scans we measure on an irregular grid of  $(\sigma_x, \sigma_y)$ . This is commonplace in ptychography to avoid a certain type of artifacts that appear when a regular grid is used.

## 6.2 Registration correction

When the objective lens is moved – both in FP scans and in  $\Delta 2\theta$ -scans in traditional DFXM – the image is shifted by a distance given by the lens shift times the magnification plus one. For this reason, we translate the detector by the same distance to keep the image in the same place. Even so, we always see small errors in the positioning of both the lens and the detector that lead to registration errors in the collected images. When not accounted for, these are limiting to the resolution of the experiment. Therefore registration correction of measured images is an important part of the DFXM data analysis.

There are two distinct sources of positioning errors. First of all the values of  $d_1$  and  $M$  in Eq. (6.1) used to make the scan may be wrong. This leads to a systematic linear shift of the measured images as a function of  $\sigma$ . This is normally the dominant source of position errors, but it can be eliminated by carefully refining the values of the geometric parameters. When the systematic shift is removed, small random errors in the lens and/or detector position cause apparently random shifts of the measured images on the order of 10 pixels.

The registration correction methods used in this work are all based on phased cross-correlation methods using the `scikit-image` implementation of a super-sampling cross correlation method.[34] This function takes two pixelated images, that are assumed to be images of the same ground-truth, but are shifted with respect to each other. The output is a 2D vector giving the shift of the one image relative to the other.

We test two different approaches to correcting for registration errors. One, inspired by the literature,[80] calculates a registration correction once as a pre-processing step by starting at the center of the data set and comparing each image to its immediate neighbors. We found that this approach fails to register images in the transition from bright field to dark field images. We therefore only use the registration values from the bright-field part of the data set. For the remaining images we fit a linear trend to the calculated values and extrapolate this fit to the edges of the data set to take care of any systematic errors. We also replace outliers in the center of the data set if there are any. With this initial registration we hope to have removed the systematic shifts, but the recovered shifts typically have low accuracy and the random shifts are still present in the dark field images.

Therefore we also test an iterative approach to registration correction, where the registration values are re-calculated at several points throughout the FP reconstruction by comparing the raw data with the forward model of the reconstruction at the given point of convergence. This allows us to find registration values extending all the way to the edge of the data set.

We test the registration correction on simulated data. Figure 6.1 shows that both registration approaches perform better than no registration correction but fall short of using the ideal registration values, that were used to generate the simulated data. We note that using the ideal values does not give the same exponential convergence observed when

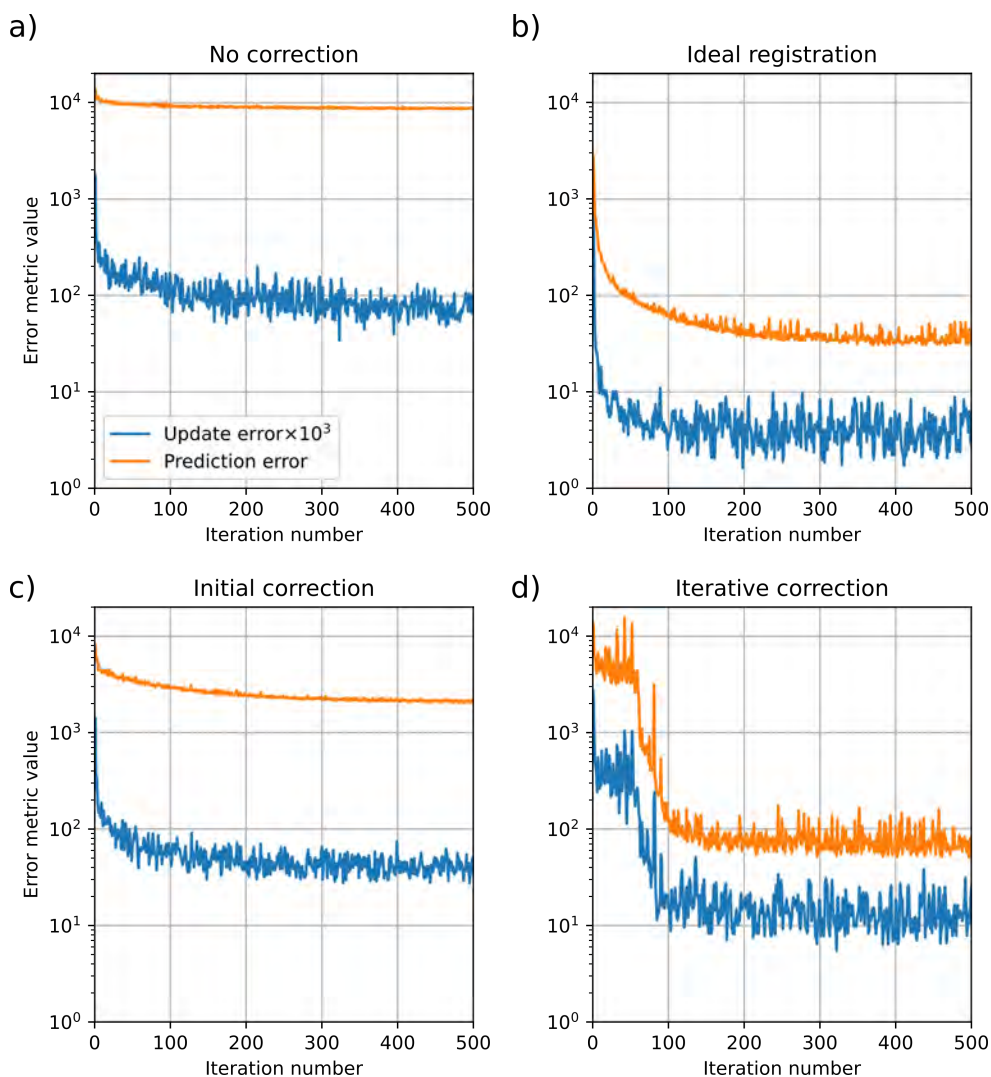


Figure 6.1: Convergence plots of four different approaches to reconstructing data with registration errors. The simulation- and reconstruction parameters are the same as in Sec. 4.6 with added random registration errors of RMS 5 pixels in both directions. a) Normal reconstruction with no registration correction. b) Reconstruction using known registration errors that were used to generate the data. c) Reconstruction using the registration correction as a pre-processing step. d) Reconstruction using iterative registration corrections as a part of the reconstruction.

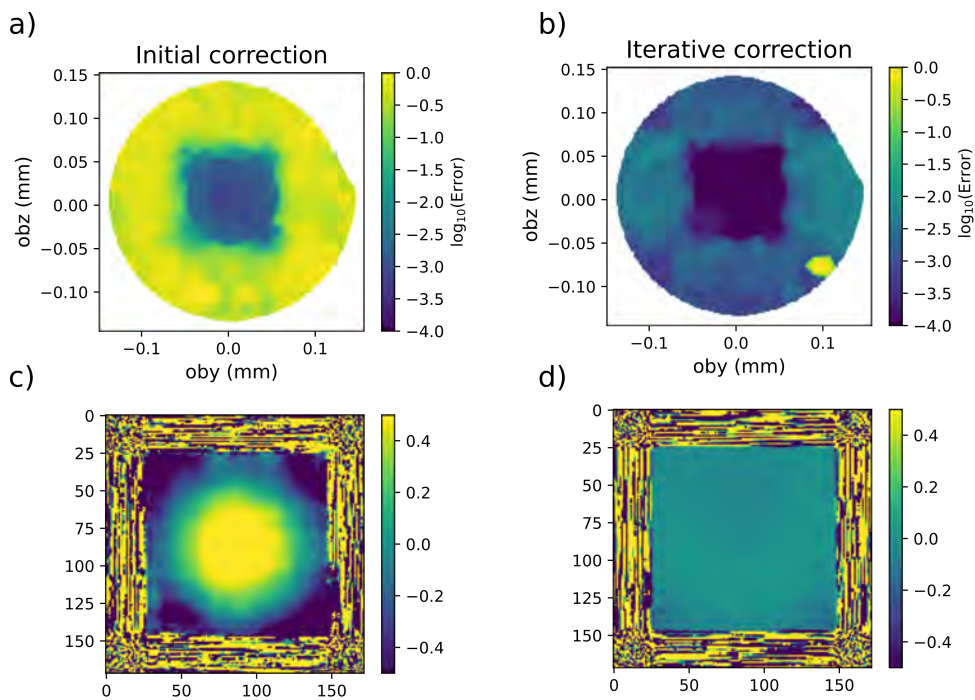


Figure 6.2: Comparison of reconstructions of simulated data using the initial (a,c) and iterative (b,d) approaches to registration correction. (a,b) shows the normalized prediction error for each image. (c,d) show the phase of the reconstructed aperture functions in radians.

using perfect data. This might be due to the slightly different methods used to shift the simulated images (Fourier interpolation) and back-shift the images in the reconstruction (quadratic spline interpolation).

In the test case used here, the iterative registration procedure sometimes falls victim to a behavior where a small number of images close to the bright-field to dark-field transition are registered incorrectly, shifting the image by exactly one period of the line-patterns used in the phantom sample. This causes a localized error in the recovered aperture function corresponding to the position of this image. This in turn affects the neighboring images and deteriorates the quality of the reconstruction for these images. This error can easily be identified from the reconstructed aperture when it appears, and we can avoid it by restricting the magnitude of the registration correction and by not refining the aperture in the initial cycles of the reconstruction. This restriction is what causes the slow convergence in the first  $\approx 50$  iterations as seen in Fig. 6.1.

From Fig. 6.2 a,b) we see that, while the initial correction approach fails at high-shift where the registration is not calculated, the iterative correction gives a good prediction of all images except in a single image, where the registration appears to have failed. Neither of the two reconstruction approaches are able to reconstruct the small spherical aberration included in the simulation data (Fig. 6.2c,d), but the initial correction approach erroneously reconstructs a much larger aberration with the opposite curvature.

Now that we have reliable values of the experimental registration errors, we use the chance to document our result to give some insight into the average size and repeatability of the positioning errors. The result of the initial registration step for the central 50 images in the data set are shown in Fig. 6.3. For this experiment we were very careful to calibrate the geometric parameters and eliminate the systematic shifts. The registration errors have a standard deviation of 4 pixels in the  $y$ -direction and 14 pixels in the  $x$ -directions. A shift of 1 pixel corresponds to either an error of the detector position of  $0.7\ \mu\text{m}$  or of the lens position of 50 nm. Both the detector and lens is mounted on a gantry, where the  $y$ -stages are mounted on top of the heavier  $z$ -stages.

It is clear from Fig. 6.3a) that the positioning errors are spatially correlated. They appear to be correlated in space rather than in time (the images were collected in a spiral pattern starting from the middle). We have also observed that they are correlated with the registration errors we observe if we repeat the same measurement several times.

We have performed individual scans of the lens- and detector positions independently, where the position of the image has been tracked using the cross-correlation. For these scans we find a much smaller deviation from the linear trend with a standard deviation of less than one pixel. The ranges of these scans are approximately half of the range of the FP scan presented in Fig. 6.3. The large shift-errors seen in the FP scan of upwards of 15 pixels is not observed in these individual scans.

## 6.3 Transmission experiments

We have carried out a number of FP experiments at the ID06-HXM. First, to test the implementation we perform a transmission-experiment. The sample is a resolution-chart with a number of structures containing dense line-patterns of known line width. We have collected a data set both with and without using the decoherer. Examples of the raw images are shown in Fig. 6.5. On the raw coherent images, we see that the detector is separated in two regions, one bright and one dark. The edges separating these two regions form a magnified image of the aperture of the objective lens, which is a  $0.1\ \text{mm}$

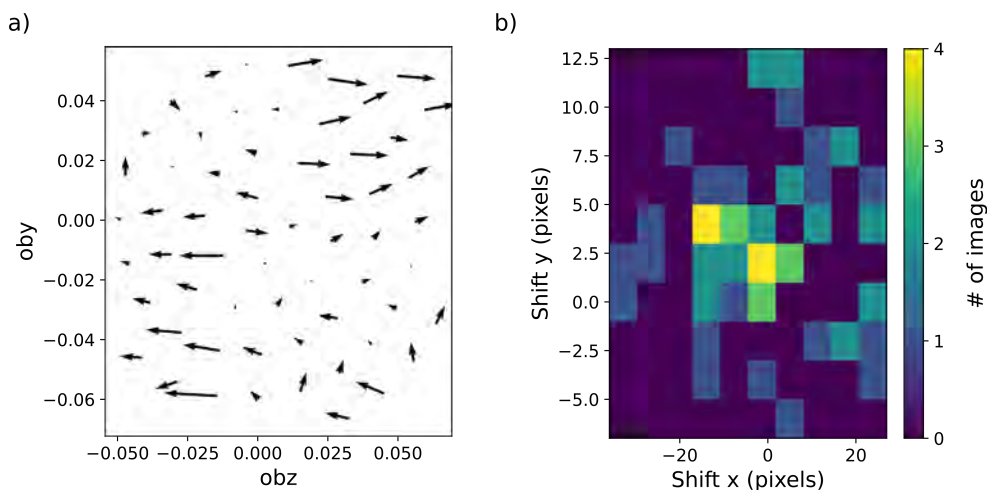


Figure 6.3: Initial registration of transmission experiment with the JIMA250 sample with decoherer. a) shows the direction of each calculated shift at the position of the image in the data set. The length of the arrows are not to scale with the separation between the arrows. b) shows a 2D histogram of the shift values from a).

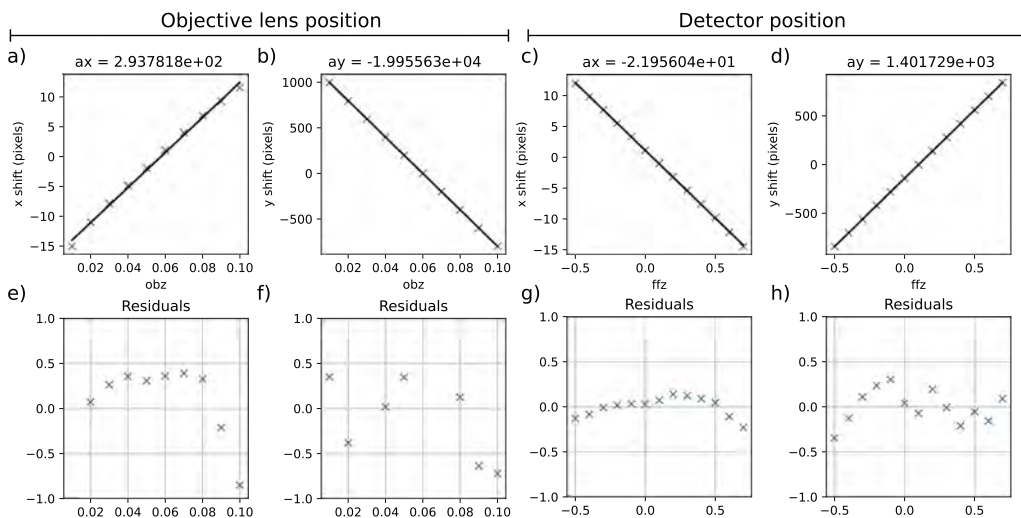


Figure 6.4: Measured image shifts as a function of objective lens position (a,b,e,f) and detector position (c,d,g,h). Figures a-d) show the calculated shift of the image and e-h) shows the deviations from a linear trend.

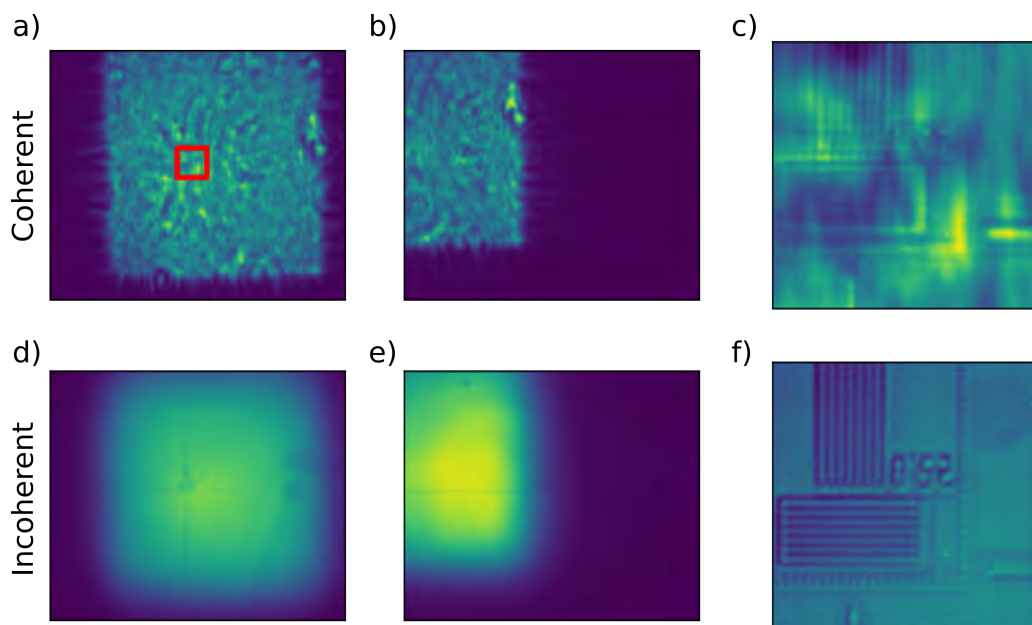


Figure 6.5: Examples of experimental images from a FP data set in transmission mode. a-c) shows a data set captured without the use of a decoherer. d-f) shows a data set captured using a decoherer. a,d) and b,e) are images of the full detector at two different positions of the objective lens. c,f) show a zoomed in region of the same images as a,d). The size and position of this region is marked by the red square in a).

by 0.1 mm square slit inserted for the purpose of this experiment. The dark-field region appears uniformly dark in these images but if the color map is adjusted, we see dark-field contrast at points where the sample has structure. Comparing the two images, we see that the bright-field region is moved when the objective lens is moved. The bright field region is not uniform, but contains *speckle-like* features due to high-frequency aberrations in the lens. In the images taken while using the decoherer (Fig. 6.5d,e), the speckle features have disappeared and the edges of the aperture are less sharp. This is consistent with the model of a less coherent incident illumination which blurs out-of-focus features like the aperture of the objective lens.

Figures 6.5 c,f) show a zoomed-in region of the detector, where we see the features of the sample. We see both a pattern of vertical and horizontal line features with full-period  $500\ \mu\text{m}$  and line-width  $250\ \mu\text{m}$  as well as the inverted text "0.25". In the coherent image we see a large number of line-features extending beyond the dense line pattern. We believe these are ringing-artifacts, common in coherent microscopes due to the top-hat type filtering imposed by the hard cut-off of the objective lens aperture. The sample contrast is superimposed on much stronger contrast due to the lens aberrations. In the incoherent image, both the ringing artifacts and the lens noise have disappeared. We can still see effects of the objective-lens aberrations, however. In the top of Fig. 6.5f) The vertical lines appear sharp and only very little overshoot can be seen on the left hand side of the pattern. On the right hand side, the overshoot is a more significant while in the bottom of the image, the sample features appear strongly defocused. This is evidence of aberrations that cause different contrast from identical features depending on their position in the FOV.

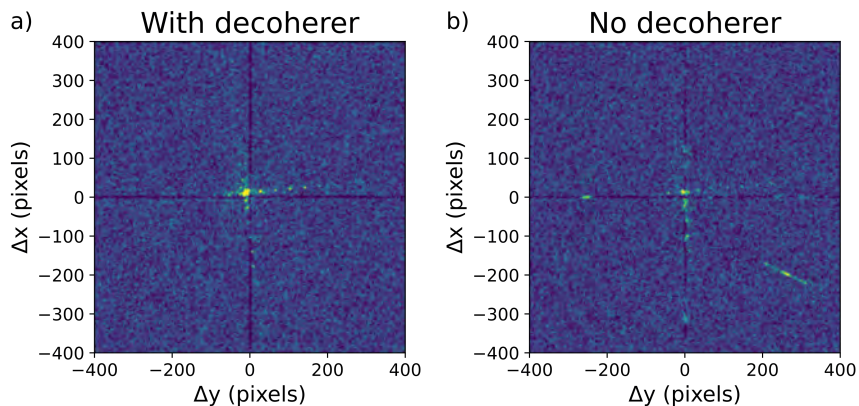


Figure 6.6: Phased cross-correlation between two adjacent images from a FP data set near the center of the data set. a) Images captured with a decoherer. b) Images captured without a decoherer.

In Fig. 6.6 we plot the phased cross-correlation between two adjacent images near the center of a FP data set respectively with and without using a decoherer. For these images the sample had been tilted by  $10^\circ$  to make features due to the straight lines of the calibration sample easily distinguishable from other features. In a) we clearly see a strong peak near 0-pixels in the center of the image with a number of satellite peaks corresponding to the period of the line-patterns in the sample. The feature is slightly offset from 0 due to the positioning error discussed in the previous section. When the decoherer is not used, another strong feature appears (lower right corner of b) ) which is due to the shifting lens-aberrations.

In the mechanical set-up of the experiment, there is an uncertainty regarding the exact position of the center of the lens relative to the center-of-rotation of the stages that rotate the lens. An error of the position would lead to an extra linear translation on top of the one required for the FP scan. Therefore, we utilize a scale parameter in the reconstruction that scales the  $\sigma$  vectors used in the forward model. To find the final value of this scale parameter we have to perform a sweep over a range of values and perform an independent reconstruction for each value. In figure 6.7 we plot the value of the prediction error at the final step of each of these reconstructions. We find that the final prediction error shows a minimum with a choice of the scale parameter around 1.3-1.35. This corresponds to a distance between the lens and the center of rotation of 10 cm. Equivalent to saying that the lens is rotating about the end of the CRL rather than the center.

### 6.3.1 Reconstructions

We perform the FP reconstruction using the ePIE algorithm of the data set collected both with and without use of the decoherer. The full data set contains 300 images covering a range of shifts up to about  $\sigma = 0.2$  mm, twice the aperture of the objective lens, however we are only able to achieve reconstruction of the low-shift part of the data set up to about the bright-field to dark-field transition. Including more images was found to give noise at high frequencies about roughly twice the NA of the objective lens. Therefore we only use first 50 images of the data set. Figure 6.8 shows the result of the reconstruction in Fourier space. We see that at approximately two times the aperture of the lens, the size of which is marked by the red square, the reconstruction fails and the reconstruction drowns in noise.

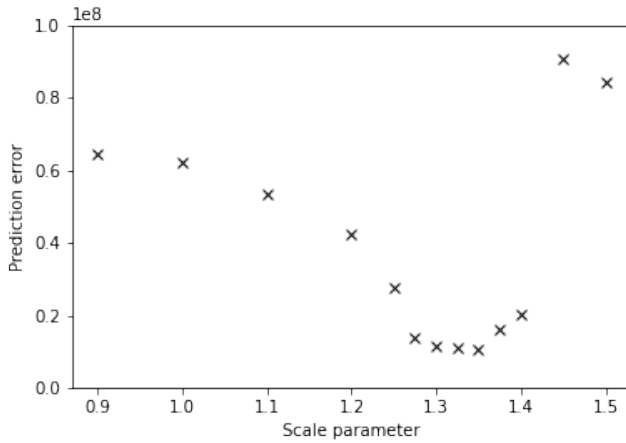


Figure 6.7: Final error function value of the reconstruction of transmission data as a function of the geometric correction factor.

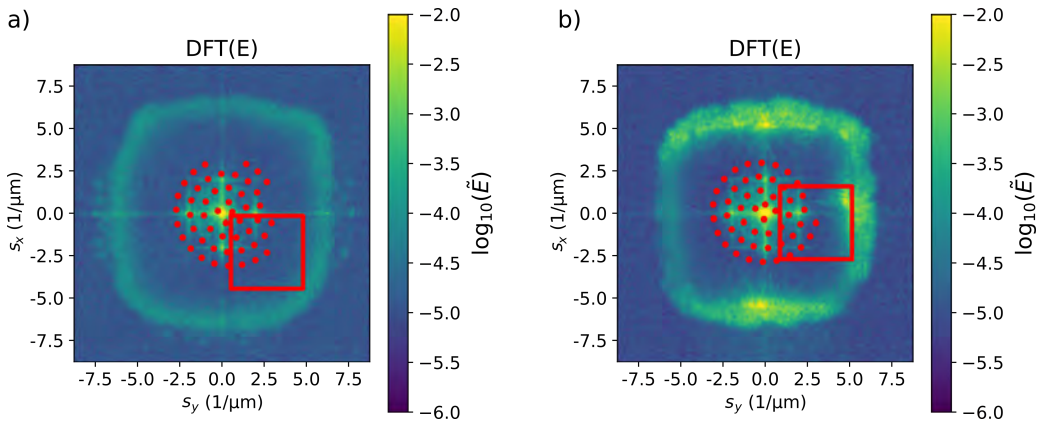


Figure 6.8: Fourier transform of reconstructed sample function of the resolution target sample in transmission mode using a) the data set taken with a decoherer and b) the data set taken without a decoherer. The red dots mark the different lens positions and the red square marks the size of the lens at the last position in the data set.

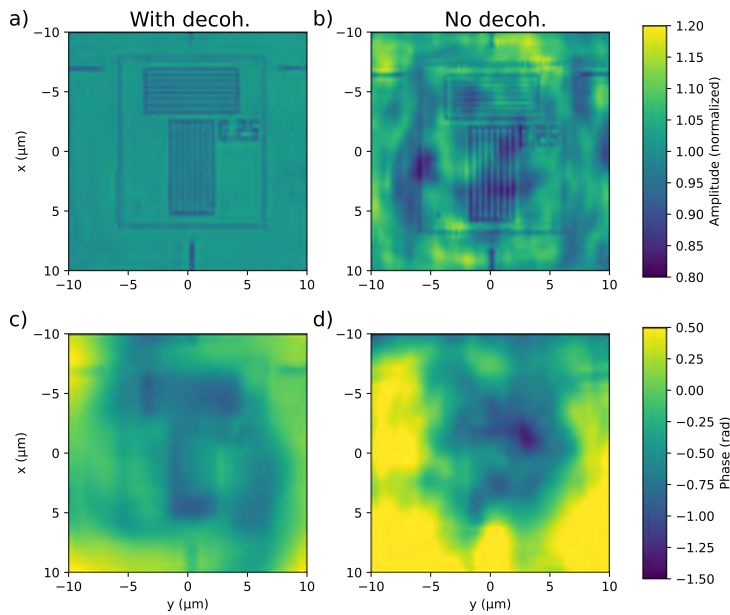


Figure 6.9: Plots of the reconstructed amplitude (a,b) and phase (c,d) of the resolution target using the data set with (a,c) and without (b,d) the decoherer.

We filter out the high-frequency noise by a simple Fourier filter and plot the reconstructed amplitude and phase in Fig. 6.9. The reconstructions are able to recover the expected features of the sample. The phase recovered from the dataset with decoherer suffers from low-frequency noise while both the amplitude and phase of the reconstruction without the decoherer suffer from stronger noise with higher frequency. While the coherent reconstruction does contain a lot of noise, it compares favorably to single raw images from the data set. (Fig. 6.5 c )

Both the reconstruction with and without decoherer appear to be defocused. This is visible by ringing artifacts around the dot-features lining the sample pattern and by the inverted contrast of the reconstructed phase in the dense line patterns. Using the normal free space propagator (Eq. (4.23)) we can digitally re-focus the reconstruction. To find the appropriate defocus distance, we calculate a stack of propagated images with different defocus distances and plot a line through the reconstruction as a function of defocus distance. Figure 6.10 shows a number of these images. We find good agreement between the simulated defocus-stack and the one calculated from the reconstruction and use this to determine the proper defocus-distance.

Figure 6.11 shows a zoomed in region of the original and the refocused image. The improvement of the phase-image is clear. The numbers are now readable and the contrast in the line-pattern now has the expected sign. In the amplitude image the improvement is mainly evident from the improved visibility of the line of dots in the right hand side of the images.

We have shown that we are able to achieve stable reconstruction in transmission mode, where we recover the expected sample features to a resolution of approximately 2 times the NA of the objective lens. It is interesting to compare our result to the much simpler DPC, as described in Sec. 4.4 method of treating the same data set. The results achieved with DPC are very similar to those of FP. The DPC result does not have the high-frequency

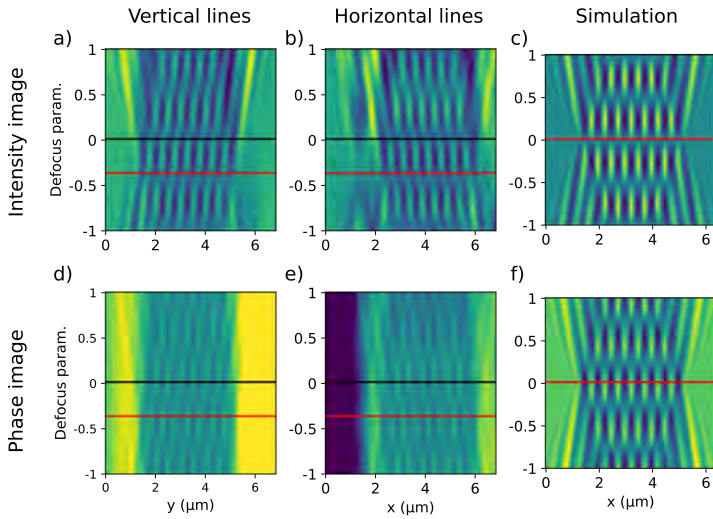


Figure 6.10: Slices through defocus stack showing the amplitude (a-c) and phase (d-f) of respectively vertical lines (a,d) and horizontal lines (b,e) of the incoherent reconstruction. The final column (d,f) shows a simulated defocus stack of a perfect line-pattern at approximately the same resolution. The defocus parameter is given in units of the Talbot length. The black line marks the original image and the red line marks the focused position.

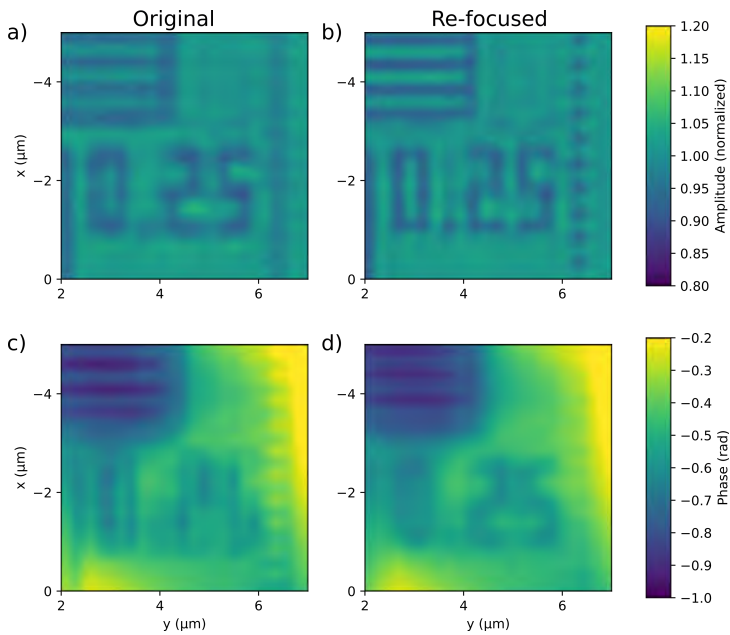


Figure 6.11: Plots of the reconstructed amplitude (a,b) and phase (c,d) of the resolution target using the data set with the decoherer. a,c) show the original image and b,d) show the digitally refocused image. The plotted region is a zoomed in version of Fig. 6.9.

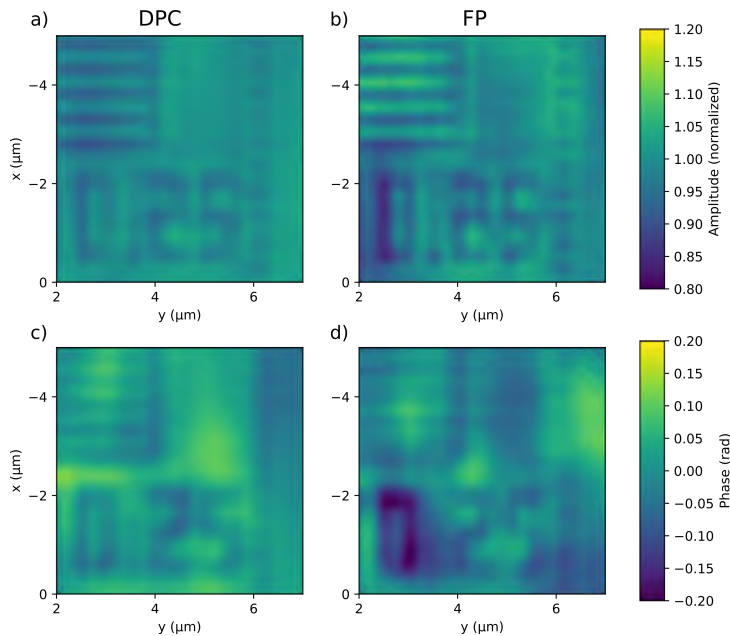


Figure 6.12: Plots of the reconstructed amplitude (a,b) and phase (c,d) of the resolution target using the data set with the decoherer. a,c) show DPC result b,d) show FP result. Both phase-images have been high-pass filtered to remove the low-frequency artifacts. The plotted region is a zoomed in version of Fig. 6.9.

errors that had to be filtered out of the FP reconstructions, but DPC has similar resolution and shows the same defocus. The reconstruction made without the decoherer contains noise of similar amplitude and frequency as that observed in the FP reconstruction (Fig. 6.9 b,d) ) but the noise is apparently not spatially correlated between the two images. We can digitally re-focus the DPC images by the same method as the FP images and find approximately the same defocus distance. In Fig. 6.12 we plot a comparison between the FP and DPC images. The two images appear to be of similar quality.

Considering that the quality of the FP reconstruction and the DPC images are of such similar quality, we cannot argue that our FP reconstruction succeeds in the aim of compensating for lens-aberrations and beating the resolution limit of the objective lens. The approximate resolution of the reconstruction of 2 times the NA is also the theoretical resolution limit for this type of DPC method.[76]

## 6.4 Thin film Bragg-reflection experiments

We now move on to look at FP of a Bragg-scattered beam. We want to avoid the complications caused by the condenser lens and by multiple diffraction effects, so as a first experiment, we use an epitaxial thin film. The sample chosen is a Bismuth ferrite (BFO) film which is known from previous studies[18, 69] to have a small mosaic spread and to contain elastic twin domain of a sub-micron size. It therefore constitutes a good test sample for Fourier Ptychography to test the resolution of the reconstructions.

In this experiment the sample is full-field illuminated and we collect data sets both with and without a decoherer in the beam. Figure 6.13 shows the experimental geometry. The experiment is done in a symmetric Bragg-geometry with scattering vector is normal

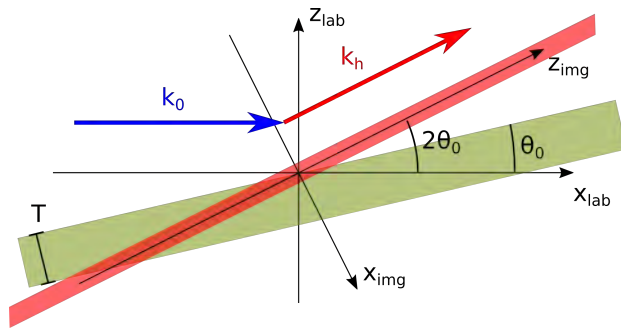


Figure 6.13: Experimental geometry of the thin-film diffraction experiment. The red bar marks the point-spread of the objective lens projected through the thickness of the sample.

to the surface of the thin-film. The scattered field is given by an integral of the scattering function through the thickness of the sample along the direction of the scattered beam, marked with a red stripe.

Inspecting the raw DFXM images in Fig. 6.14 we see a behavior very similar to the one observed for transmission images (Fig. 6.5) where there is a bright field and a dark field region and the shape of the bright field region is an outline of the aperture. The interpretation is similar to the one in transmission mode: If we consider the sample to be a single near-perfect crystal containing only small strained regions, then the scattering will primarily be in one single direction. The strained regions will give rise to weak diffuse intensity away from this direction. In some part of the image this strong beam hits within the aperture of the lens – we call this the *strong beam* region – and in other regions it hits outside of the aperture – the *weak beam* condition. In the images taken with the decoherer, the edges of the strong beam region are blurred. Furthermore, some speckle-like noise, which is present in the coherent images disappear in the incoherent images due to the averaging-out of high frequency lens aberrations.

The images contain two distinct types of contrast. We see a handful of dislocations in the film that appear as dark spots in the bright field images (6.14 b,e) ) and as bright spots in the dark field images (6.14 b,e) ). In areas away from these dislocations there is high-frequency features that appear as a random grainy pattern. This high-frequency contrast is characteristic of the BFO film and does not appear in other thin-films, we have investigated. The coherent DFXM images shown here appear to contain slightly less speckle noise than the coherent transmission images shown in Fig. 6.5.

Like in the transmission experiments, we are only able to achieve stable reconstructions up to a limited resolution and including images taken at a higher shift causes a high-frequency artifact, as shown in Fig. 6.15.

The reconstructions appear to be of a similar quality to those made in the transmission experiments. In Fig. 6.16 we plot the reconstructions of a region away from any dislocation in the thin film. In both the phase- and amplitude images we see sub-micron features. The features are recognizable from one image to the other, giving confidence that they are features of the sample and not artifacts of the reconstruction. The contrast appears to be stronger in the coherent reconstruction than in the incoherent. Especially the high-frequency features of the phase map appear dampened in the incoherent reconstruction compared to the coherent.

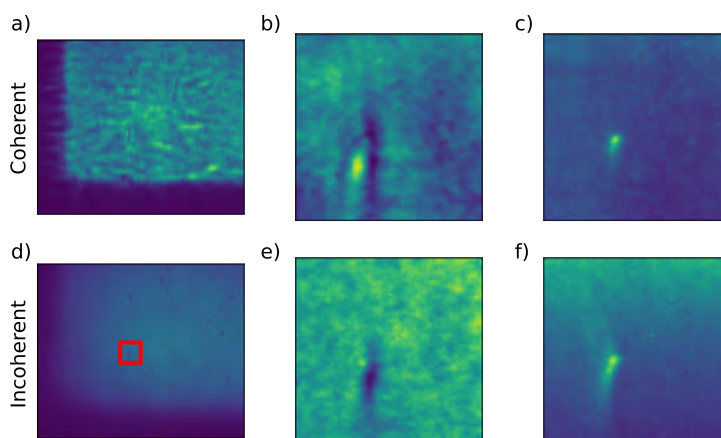


Figure 6.14: Examples of experimental images from a FP data set in transmission mode. a-c) shows a data set captured without the use of a decoherer. d-f) shows a data set captured using a decoherer. a,d) are images of the full detector b,e) show a zoomed in region containing a single dislocation of the same images as a,d). The size and position of this region is marked by the red square in a). b,f) show the same region in an image with larger  $s$  showing weak beam contrast from the dislocation.

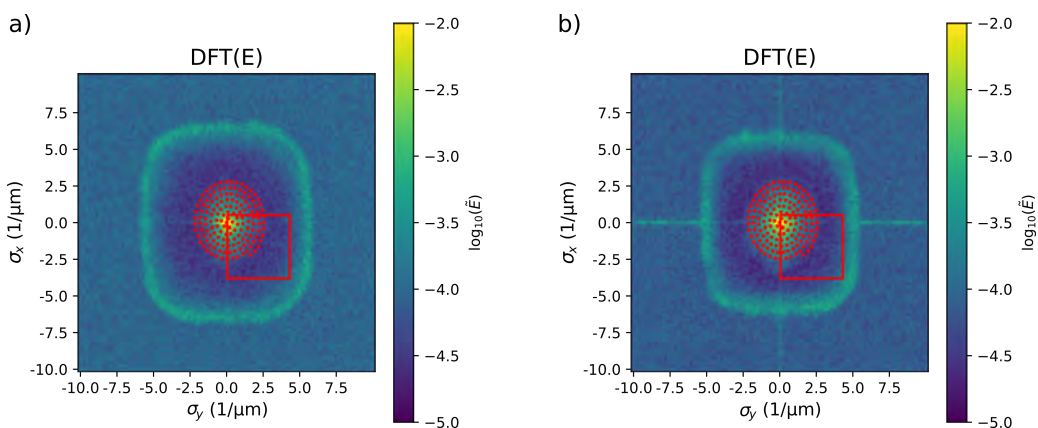


Figure 6.15: Fourier transform of reconstructed sample function of the BFO thin-film sample in Bragg-mode mode using a) the data set taken with a decoherer and b) the data set taken without a decoherer. The red dots mark the different lens positions and the red square marks the size of the lens at the last position in the data set.

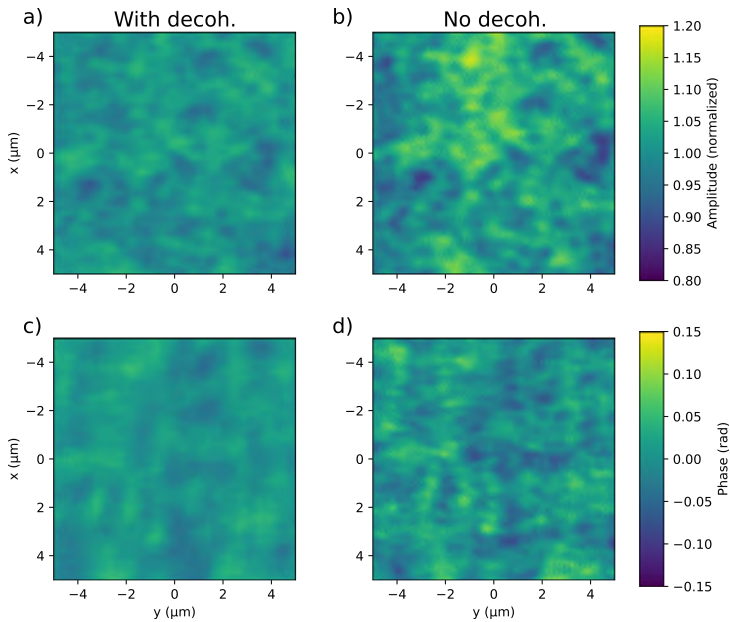


Figure 6.16: Plots of the reconstructed amplitude (a,b) and phase (c,d) of the BFO sample using the data set with (a,c) and without (b,d) the decoherer. The phase images have been high-pass filtered to remove a large "saddle point" type artifact present in both reconstructed phase maps.

To estimate the resolution of the reconstructions, we perform two independent reconstructions, each using half of the images from the same data set. We calculate the Fourier ring correlation between these two reconstructions (Fig. 6.17) and find a half-period resolution between 0.2 and 0.1  $\mu\text{m}$ .

We have also made FP reconstruction of regions of the sample around dislocations. As discussed in Sec. 2.2.2, dislocations cause vortex lines in the scattering function and therefore the projection through a thin film containing a surface-to-surface dislocation should contain a phase vortex with winding number given by the dot-product of the  $hkl$  vector and the Burger's vector of the dislocation. These phase vortices do not appear spontaneously in our FP reconstructions, but we can achieve stable reconstructions containing phase-vortices by initializing the reconstruction with such a phase vortex.

The DPC approach does not handle phase vortices well. While we can still calculate the phase-gradients (and thereby the deflection angles) using Eq. 4.34, these gradients cannot be integrated by normal gradient-field integration methods since the phase function does not exist. The integration algorithms could likely be adapted to give the wrapped phase, but this is not pursued here, rather we compare only the phase-gradients.

Figure 6.18 shows the phase-gradients calculated using DPC and two different FP reconstructions with respective 0 and 2 phase vortices. From comparing the images, it is clear that the reconstruction without a phase-vortex does not match the DPC phase gradients. The reconstruction made with the phase vortices appears to fail close to the dislocation core, where the two phase-vortices are separated by a distance of about 1  $\mu\text{m}$ , but further away from the dislocation core the agreement is excellent.

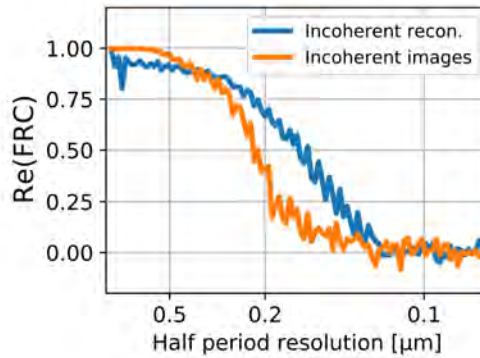


Figure 6.17: Fourier ring correlation between two independent reconstructions and between two different images. Figure reproduced from [13]

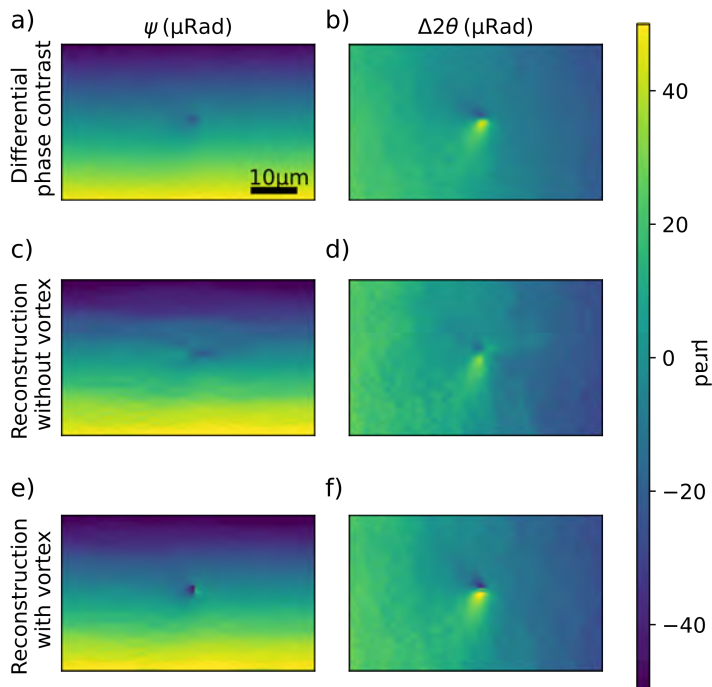


Figure 6.18: Deflection angles of the scattered beam as defined in Eq. (2.43) calculated from a,b) differential phase contrast, c,d) an FP reconstruction without phase vortices and e,f) a FP reconstruction with two phase vortices of the same sense. Figure reproduced from [13]

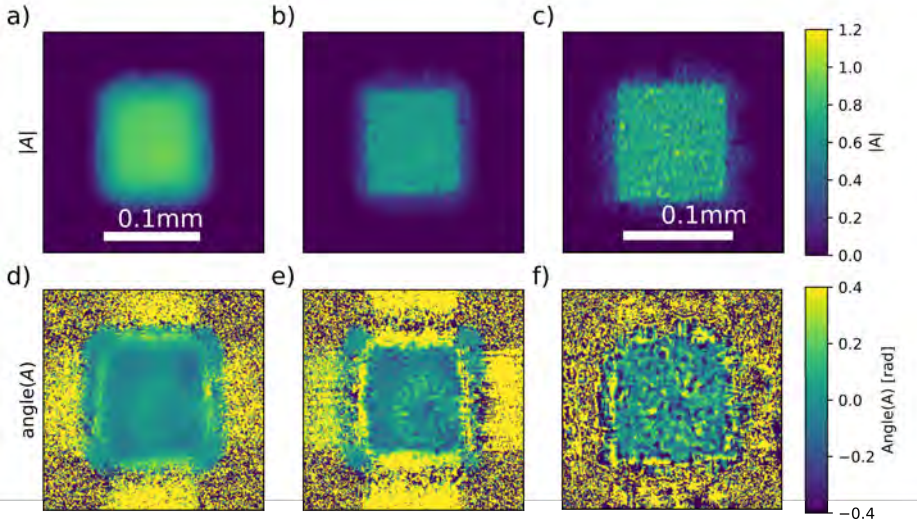


Figure 6.19: a-c) Amplitude and d-f) phase of reconstructed aperture functions. From a,d) the Bragg scattering experiment including the decoherer and b,e) without the decoherer. c-f) Are from the transmission experiment without the decoherer. Figure reproduced from [13]

## 6.5 Role of the decoherer

The decoherer is a spinning disk of amorphous material, that is inserted in the beam upstream of the sample to make the beam less coherent.[21, 27] The disk can be modeled as a random diffuser screen. Because the disk is spinning fast, this random diffuser is replaced many times over on the timescale of the exposure of the x-ray detector. Therefore, the collected images are a time average (or an ensemble average) over the different possible realizations of the random diffuser. This time-average is equivalent to how partially coherent light is described in the usual theory of partially coherent radiation based on statistical optics.[9]

The effect of the decoherer is seen in the raw images (Fig. 6.5) where the noise features due to lens-aberrations disappear and the edge of the bright field region is smoothed. This effect is also apparent from the reconstructed aperture function from FP shown in Fig. 6.19. Comparing the reconstructed aperture made with the decoherer (Fig. 6.19a,d) ) with those made without a decoherer (Fig. 6.19b,e) ), it appears that the first is a blurred version of the second. This makes sense intuitively, as the role of the decoherer is to increase the divergence of the incident light and therefore to smear out features in reciprocal space.

We find the same behavior in reconstructions of simulated data using a partially coherent forward model. The forward model is based on Abbe's method[1] for incoherent sources, where the incoherent image is given by the superposition of the intensity from a range of coherent images with different angle of illumination, which can be rewritten to:

$$I_{\text{incoh}}(x, y) = \int I(x, y; \sigma) p(\sigma) d\sigma \quad (6.2)$$

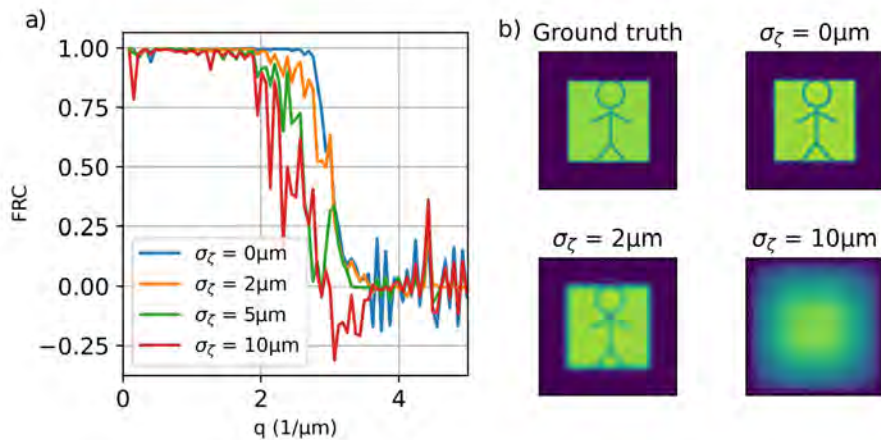


Figure 6.20: a) FRC between ground truth and simulated reconstructions. b) Images of reconstructed apertures. Figure adapted from [13]

using the notation from Eq. (4.35) where  $p(\sigma)$  is a scaled version of the source angular distribution. For the simulation, we choose a symmetric 2D normal distribution centered on zero with variance  $\sigma_\zeta^2$  for a number of different values of the variance. We then carry out FP reconstructions of the simulated data sets.

Figure 6.20 shows some results of this simulation. We see the same blurring effect in the reconstructed apertures as was seen in the experiments. From the FRC curves we see that the low coherence results in a lower resolution reconstruction, but that the reconstructions are not immediately broken by a small amount of partial-coherence.

## 6.6 Discussion & outlook

We have made a proof-of-principle demonstration of a Fourier ptychographic approach to the analysis of DFXM data. The experiments were a partial success in that we were able to recover the phase of the wave-front and to reconstruct images of the objective lens aberrations but we did not achieve a significant improvement of the resolution and image-quality compared to the traditional data-treatment.

There is a number of possible explanations as to why the reconstructions fail at high resolution. We list a few of them here:

1. **Geometric errors:** Determining the exact geometry of the DFXM instrument relies on calibrating a number of motor positions. Typically in DFXM this is not critical to the experiment, as we only rely on the relative distances and do not require high quantitative accuracy of the absolute positions of all optical components. The calibration of the geometry for our FP experiments was done by attempting reconstruction with different values of the correction factor as shown in Fig. 6.7. This shows a wide minimum of the error function value and does not give us a lot of confidence that this parameter was assigned correctly with high precision. Furthermore there are a number of other geometric parameters that possibly cause problems for FP reconstructions, such as misalignment angles of the detector and translation stages relative to the laboratory coordinates.

2. **Weak signal in high shift images:** When the objective lens is shifted to a high angle, the intensity of the images goes down quickly. This is a problem because the images at high shift will then have a poor signal-to-noise ratio. The noise in the experimental images seems to be dominated by electrical readout noise of the detector but other sources such as counting noise and gas scattering probably also contributes.
3. **Non-ideal detector behavior:** The detector used for the experiments was an indirect x-ray detector based on a thin scintillator screen and an optical microscope. This detector was chosen because of the small pixel size, which is needed to oversample the images, a prerequisite of FP. We are aware that the effective resolution of this detector is lower than the pixel size, which we tried to compensate for by including an aperture in the objective lens to make the required resolution as low as 2 times the pixel pitch. We did however not do a proper characterization of the detector point spread. Other non-ideal detector behavior like a non-linear intensity response, geometric image distortions[15] and readout noise could also be a problem for the FP reconstructions.

It is instructive to compare the method of data treatment presented here with “normal” ptychography, [60, 75] where a focusing lens is used to focus the incident light onto the sample. The sample is then raster-scanned while a diffraction pattern is collected for every sample position. As the name suggests, FP is closely related to ptychography. In FP, the Fourier transform of the sample function takes the role of the sample in normal ptychography and the aperture function takes the role of the focused beam profile.

Ptychography has also been used in a Bragg-scattering geometry to image the scattering function of small crystals and thin films,[38] a technique the authors call *projection Bragg ptychography*. The experimental set-up of this method has many similarities to our experiment, the main difference being that the lens is placed before the sample, rather than behind it. This difference makes some aspects of the experiments easier. First of all, the lens does not have to be moved but can remain in a fixed position on the optical axis while only the sample is moved. This means that only one 2D translation stage is needed to do the experiment and a much smaller range of movement is needed.

Another advantage is that since Ptychography measures the far field diffraction pattern, the pixel-size needed to oversample the field can be made larger by moving the detector further away from the sample. This means direct detectors with better noise characteristics can be used instead of the indirect detectors used in DFXM.

Another recently introduced method, called *ptychographic topography*[79] is even more similar to our FP-DFXM. In this method a pinhole aperture is scanned in the scattered beam while diffraction patterns in the far field of the aperture are collected. These diffraction patterns are used to make a ptychographic reconstruction of the scattered field. Because this method only scans optical components placed downstream of the sample, one has the option to introduce a focusing component before the sample to achieve a geometry similar to the slicing mode of DFXM. This has been shown using a pencil-beam rather than a sheet beam.[61] This method is very new and has so far only been demonstrated on small and near-perfect crystals.

The big advantage that DFXM has compared to the various focused-probe methods is the ability to study large 3D samples in the slicing mode by placing the sample in the focus of a 1D condenser that forms a sheet beam. We have made attempts to do FP in the slicing mode of the DFXM microscope but did not achieve stable reconstructions.

It is difficult to suggest a good sample to test FP in the slicing mode. If we choose a near perfect crystal with a few isolated defects, we have to deal with dynamical diffraction effects. It is not clear if the assumption of a coherent field is appropriate in this case. The energy bandwidth of the incident light is comparable to the Darwin width of dynamical scattering and when the condenser is used, the angular spectrum of the incident beam is much wider than this, so the scattered beam at any one setting is given by an integral over the dynamical rocking curve.

Choosing, on the other hand, a highly deformed crystal, where we can ignore dynamical scattering effects, we face the problem that the scattered beam at a fixed rocking angle consists of small disconnected regions, where the crystal satisfies the Bragg condition, separated by regions of zero intensity. In this case the scattering pattern would not have enough non-zero intensities to be able to refine the aperture function. Also, DFXM images are only sensitive to short-distance correlation in the phase function (over the size of the coherent point spread function), so the relative phase between such disconnected regions can not be determined.



# 7 Simulating a Dark-Field X-ray Microscope

In the existing literature on DFXM, efforts to describe and simulate the method have typically relied on ray optics.[59, 67] In ray optics, one assumes that interference only takes place over a small length scales which gives rise to refraction and Bragg-scattering that changes the path of a given ray, but rays that have taken significantly different paths to reach the same point on the detector are assumed to have uncorrelated phases. In Sec. we observed strong speckle-like noise in transmission and thin-film diffraction data, an example of these diffraction effects, that are not handled by ray optics.

Another subject of interest are the multiple scattering effects, *dynamical scattering*, that are present in diffraction images of near-perfect crystals. FP is thought as a possible tool for studying weak defects in near perfect crystals, where dynamical scattering features are bound to show up. So in order to better understand these effect, we set out to develop a computational model of the DFXM-instrument based on the propagation of coherent wave-fronts. In this model diffraction effects are included by using coherent wavefront propagators and dynamical diffraction can be included within the framework of the Takagi-Taupin Equation.

Figure 7.1 sketches the flow of such a simulation. The steps are as follows:

1. Characterization of the incident beam.
2. Characterization of the sample crystal.
3. Propagation of the beams (transmitted and scattered) through the sample crystal by numerical integration of the TTEs.
4. Propagation of the scattered beam through the CRL and onto the detector.
5. Simulating detector characteristics.

## 7.1 Characterizing the incident beam

The starting point for the simulation is a description of the incident x-rays at the plane where they meet the sample. One way to achieve this would be to model the electron beam, undulator source and beam-shaping optics of the beamline using existing software packages such as SRW.[19] Due to time constrains, we instead choose to make the assumption that the beam is spatially uniform at the plane of the condenser lens with a Gaussian energy bandwidth set by the monochromator and with a Gaussian mutual coherence function.

To get the transverse coherence lengths, we use the source parameters specified on the ESRF website and propagate them using a Gauss-Schell[70, 83] model to the plane of the condenser lens. We find (Fig. 7.2) that both the vertical beam width and coherence lengths are longer than the aperture of the condenser lens typically used ( $\approx 200\mu\text{m}$ ). Therefore, we can use a model where the beam is fully coherent in the vertical direction.

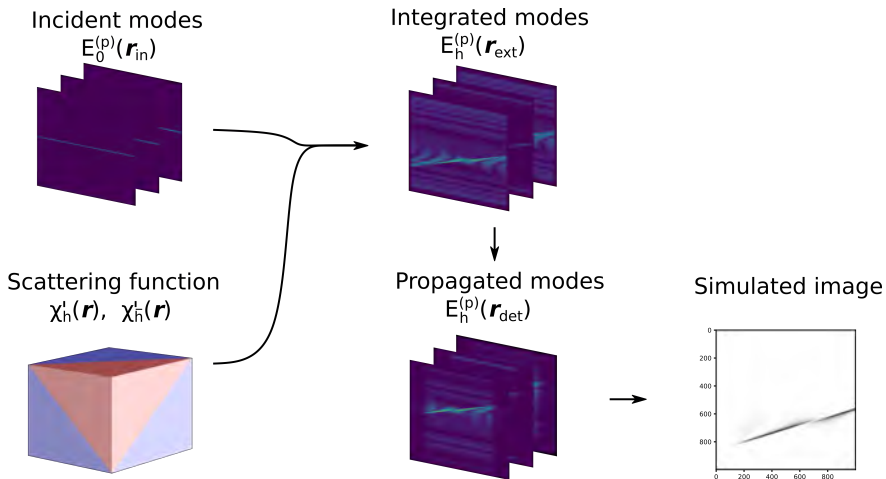


Figure 7.1: Sketch of the flow of the simulation of the DFXM microscope. Figure adapted from [12].

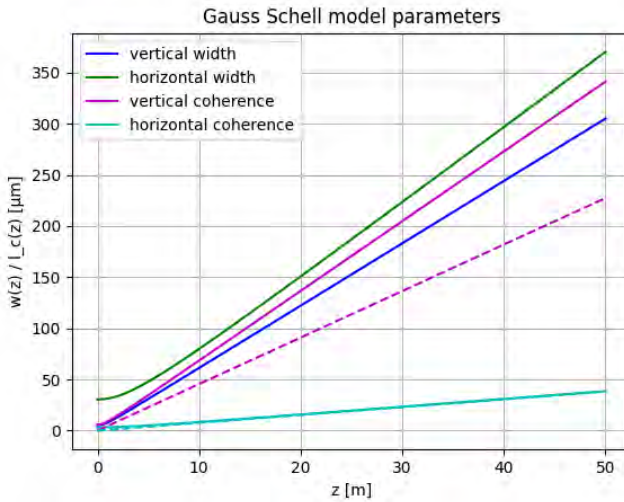


Figure 7.2: Beam widths and coherence lengths calculated using a Gauss-schell model with full lines. The dashed lines are the coherence lengths calculated assuming an incoherent source of the same size.

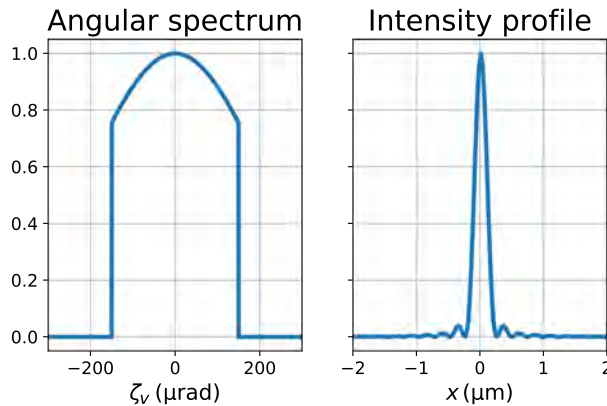


Figure 7.3: a) Vertical divergence and b) spatial profile of the incident beam at the sample plane. Figure reproduced from [12].

The horizontal coherence length is found to be around  $40 \mu\text{m}$ , which is smaller than the FOV of the microscope and therefore we should include several partially coherent modes in the horizontal direction, but since a microscope can typically be considered to be fully coherent when the coherence length is larger than the point spread function we believe that the effects of partial coherence in the horizontal direction will be small. We therefore approximate the beam is horizontally coherent and describe the beam by only one mode in the horizontal direction as well. Thereby we end up with a model of the incident beam that is transversely fully coherent but has a finite energy bandwidth.

The condenser lens used in the ID06-HXM is a 1D CRL of either Be or plastic depending on the X-ray wavelength used. Typically a set of slits close to the condenser lens is used to limit the vertical extend of the beam incident on the condenser lens and thereby the vertical divergence of the beam incident on the sample. For our purposes we would like to treat the slits and the lens as a single optical component in the thin lens approximation. The transmission function of this component will be the product of a 1D ideal-lens term that focuses the beam in the vertical direction onto the plane of the sample and an aperture function consisting of both a hard cut-off in both directions from the slits and a Gaussian profile in the vertical direction due to the absorption in the lens-material. We will consider both ideal condenser lenses and aberrated condenser lenses, that have high-frequency errors in the aperture functions. The aperture and line-beam profile of the condensed beam with an ideal condenser lens are plotted in figure 7.3.

As a first test of the chosen model, we place a analyzer crystal in the focused beam and measure the rocking curve. The measured rocking curve of the analyzer crystal is shown in figure 7.4 a). We see that there is some misalignment of the hard cut off compared to the Gaussian profile. The hard cut-off is blurred due to a combination of dynamical scattering effects, diffuse scattering from the surface, and the finite bandwidth. When the effects are taken into account, using a perfect-crystal propagator to handle the dynamical scattering, we get the simulated rocking curve of Fig. 7.4 b) where the hard cutoffs are blurred to approximately the same width as on the measured curve.

The detector used to measure the rocking curve was an image detector with small pixel size. We can use the spatial profile of the rocking curve to infer some information about the kind of aberrations present in the condenser lens. Figure 7.5 a) shows the integrated intensity of the rocking curve. This is a section topography image and displays pendelö-

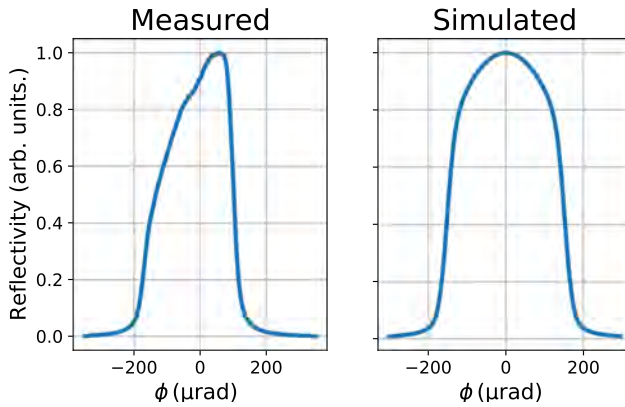


Figure 7.4: a) Measured and b) simulated rocking curve of an analyzer crystal. Figure reproduced from [12].

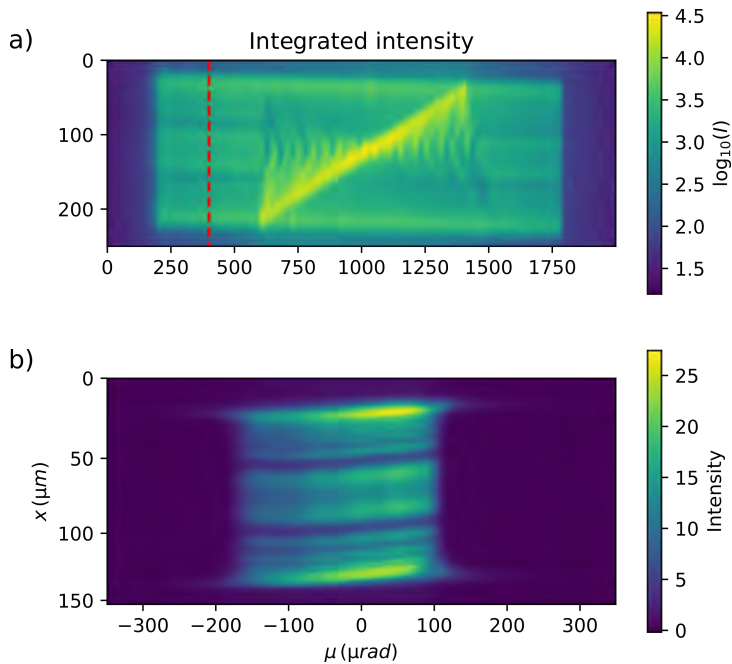


Figure 7.5: Measured near-field rocking curve of an analyzer crystal. a) section topography integrated over rocking curve. b) Intensity of a line-profile marked with a dashed red line in a) as a function of rocking angle.

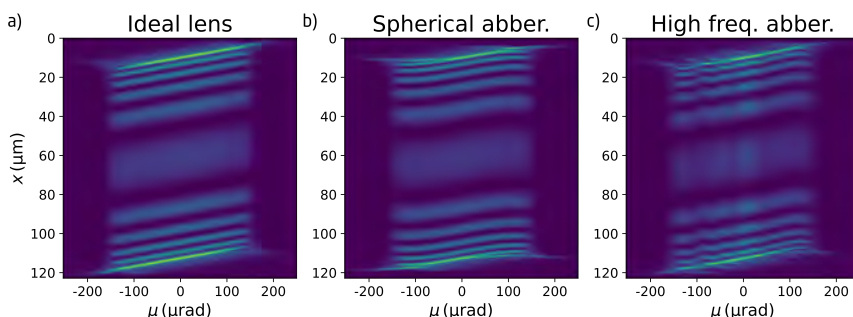


Figure 7.6: Simulated near-field analyzer rocking-curve with a) an ideal condenser lens, b) a condenser lens containing a large spherical aberration and c) a condenser lens with high-frequency aberrations.

sung fringes in the form of horizontal stripes. In the center of the image is a stacking fault. The bright line is the direct image of the intersection between the transmitted beam and the stacking fault. We plot the intensity in one line of this image as a function of the rocking angle in Fig. 7.5 b). Here we see the width of the angular spectrum of the incident beam and a sharp cut-off. Furthermore we see that the image shifts position as the crystal is rocked. This is due to the finite distance between the sample and the detector and has a purely geometrical interpretation. More interestingly, there appear to be some vertical stripe-features in the image, which we interpret to be due to aberrations in the condenser lens.

As a test we simulate a number of such rocking curves with different models of the condenser lens shown in Fig. 7.6. Here we see that the vertical stripe features observed experimentally also appear in simulations using a condenser lens with high-frequency aberrations. The characteristic width of these stripes are due to the finite bandwidth of the incident light. The aberration function used contains structures on all length scales and monochromatic simulations contain stripes of much shorter width than the ones observed in this image but these are blurred out by the integration over photon energy.

The simulated rocking curve using a condenser lens with (the 1D equivalent of) spherical aberration has wavy lines instead of the straight lines observed in the two other images. This is because the analyzer crystal only reflects a small part of the incident angular spectrum at any one angle. With a spherically aberrated lens, different parts of the angular spectrum is focused into slightly different positions on the sample plane, therefore the image moves up and down.

All of the simulated images appear sharper than the measured one. This is probably due to the relatively poor point spread of the near-field detector. This is also probably why we don't see any signs of aberrations in the horizontal direction, that would appear as vertical stripes in figure 7.5 a).

## 7.2 Model of the sample crystal

In order to simulate a DFXM image, we need a model of the sample crystal. The quantity of interest is the spatially varying susceptibility functions of Eq. (2.26). To determine this function, we need to know the value of the Fourier coefficients  $\chi_0$ ,  $\chi_h$  and  $\chi_{\bar{h}}$ , that depend on the atomic structure. When a sample contains twin domain boundaries without twinning strain, these coefficients are spatially varying. But in most cases these can be

assumed to be constants and can be calculated from the crystal structure.

$\chi_h$  and  $\chi_{\bar{h}}$  are not uniquely defined, as they depend on the choice of origin of the unit cell. We can always pick a unit cell where one of the two is real. A Bragg reflection with a real-valued coefficient is sometimes called a *central reflection*. For a given reciprocal lattice vector  $\mathbf{h}$ , the value of  $\chi_h$  is given by:

$$\chi_{\mathbf{h}} = \frac{1}{V_{\text{u.c.}}} \int_{\text{u.c.}} \chi(\mathbf{r}) e^{i\mathbf{h}\cdot\mathbf{r}} d\mathbf{r} \quad (7.1)$$

where the integral is over the first unit cell. This constant is directly proportional to the more commonly utilized structure factor  $F_h$ :

$$\chi_h = - \left( \frac{4\pi r_0}{k^2 V_{\text{u.c.}}} \right) F_h \quad (7.2)$$

where  $V_{\text{u.c.}}$  is the volume of the unit cell and  $r_0 = 2.82 \cdot 10^{-15}\text{m}$  is a physical constant known as the classical electron radius.

If we change the origin by a vector  $\Delta\mathbf{r}$ , we change the value of the exponential function by a factor  $e^{i\mathbf{h}\cdot\Delta\mathbf{r}}$  which we can draw outside of the integral thereby changing the scattering function by an arbitrary phase factor. By the same consideration, we would also change the value of the opposite scattering function by the opposite phase. Therefore, the product of the two scattering functions is constant and is the real physical quantity of interest. We note that only the product of the scattering functions appears in measurable quantities such as the pendellösung length, the extinction length, and the Darwin width. When we can ignore anomalous absorption effects, that is to say when  $\chi(\mathbf{r})$  is real, Friedel's law holds and the product of the scattering functions is real. It is therefore tempting to consider the two real quantities  $\phi_h = \text{Re}(\chi_h \chi_{\bar{h}})$  and  $\psi_h = \text{Im}(\chi_h \chi_{\bar{h}})$  that describe the strength of the reflection and the anomalous absorption respectively.[48]

The quantity  $\chi_0$  does not have this ambiguity and can be determined from the density and atomic content of the crystal. The real part,  $\chi_0^{(r)} = -2\delta$ , describes refraction and is for the most part not important. The imaginary part,  $\chi_0^{(i)} = 2\beta$ , describes absorption and can have a large impact on the dynamical diffraction patterns.  $\chi_0^{(i)}$  is related to the linear attenuation coefficient:  $\mu_{\text{att}} = \chi_0^{(i)} k/2$ . In the literature on X-ray topography it is common to classify Laue-experiments based on the dimensionless quantity  $\mu_{\text{att}} t$ , where  $t$  is the thickness of the crystal.

When  $\mu_{\text{att}} t < 1$  we call it a thin crystal or a low-absorption topography. When  $\mu_{\text{att}} t > 10$  we correspondingly call it a thick crystal and a high-absorption topography. In DFXM we typically only use thin crystals. In thick crystals the contrast mechanisms are different. Especially in the case where  $\psi_h$  is also large (of similar size to  $\chi_0^{(i)}$ ) where the *Borrmann effect* comes to dominate the diffraction patterns.[48]

The scattering constants of a number of relevant materials are listed in Table 7.1. The first three entries show the trend that as the atom-number is increased, both the refraction- and absorption constants increase, but the absorption increases more quickly. The large absorption is a problem for the experiment as it attenuates the measured signal. Increasing the photon energy conversely decreases both the refraction- and absorption constants. For all the materials listed here, the refraction constants are at least an order of magnitude larger than the absorption constants.

Material	Energy	Reflection	$-\text{Re}(\chi_0)$	$\text{Im}(\chi_0)$	$\text{Re}(\sqrt{\chi_h \chi_{\bar{h}}})$	$\text{Im}(\sqrt{\chi_h \chi_{\bar{h}}})$
Diamond	17 keV	(111)	$5.0 \cdot 10^{-6}$	$1.4 \cdot 10^{-9}$	$1.8 \cdot 10^{-6}$	$1.0 \cdot 10^{-9}$
Aluminium	17 keV	(111)	$3.8 \cdot 10^{-6}$	$1.6 \cdot 10^{-8}$	$2.6 \cdot 10^{-6}$	$1.6 \cdot 10^{-8}$
$\alpha$ Iron	17 keV	(110)	$1.1 \cdot 10^{-5}$	$3.7 \cdot 10^{-7}$	$7.8 \cdot 10^{-6}$	$3.7 \cdot 10^{-7}$
	33 keV	(220)	$2.9 \cdot 10^{-6}$	$2.8 \cdot 10^{-8}$	$1.3 \cdot 10^{-6}$	$2.8 \cdot 10^{-8}$
BaTiO <sub>3</sub>	17 keV	(200)	$7.6 \cdot 10^{-6}$	$2.1 \cdot 10^{-7}$	$5.2 \cdot 10^{-6}$	$2.1 \cdot 10^{-7}$
	17 keV	(111)	$7.6 \cdot 10^{-6}$	$2.1 \cdot 10^{-7}$	$3.2 \cdot 10^{-6}$	$1.4 \cdot 10^{-7}$

Table 7.1: Scattering parameters of relevant materials. Materials, reflections and energies are taken to match the experiments presented here as well as a number of recent publications. [53, 84, 85]

For most samples, the scattering constants can be assumed to be constant throughout the crystal and the real quantity of interest is the displacement field  $\mathbf{u}(\mathbf{r})$ . For a number of ideal defects such as isolated dislocations, symbolic expressions for the associated displacement fields are given in the literature.[36]. For perfect twin-domain boundaries, like the ones described in Section 3.2, the displacement field is related to the strain-tensor, and can in a fairly straight forward manner be constructed from the transformation matrices  $\mathbf{S}$  by separating space the space into two regions separated by a domain wall with normal  $\mathbf{n}_w$  centered on zero. The displacement field is then:

$$\mathbf{u}(\mathbf{r}) = \begin{cases} 0, & \mathbf{r} \cdot \mathbf{n}_w \leq 0 \\ (\mathbf{S} - \mathcal{I})\mathbf{r}, & \mathbf{r} \cdot \mathbf{n}_w > 0 \end{cases} \quad (7.3)$$

As discussed in Section 3.2, some combinations of a specific domain wall and a Bragg-peak cause a split-Bragg peak. When a splitting occurs, the distance between the sub-peaks is on the order of the symmetry breaking strain, typically orders of magnitude larger than the Darwin-width, so we believe that we can essentially treat the domains on either side of such a domain wall as two separate crystals. That is to say, we believe that x-rays scattered inside one domain should not be re-scattered inside a different domain.

For domain walls that do not split a given Bragg-peak, including non-elastic inversion domain boundaries in ferroelectric crystals, the difference in the scattering function due to the domain boundary will at most be a discrete jump of the phase of the scattering function from one side of the boundary to the other. The value of this jump depends both on the crystal structure and on the structure of the domain wall. Namely, the position within the unit cell of the twinning operation (either the rotation axis or the mirror plane) that generates the twin.[42] The structure of domain walls is not often reported in the literature, so the value of this phase jump is not straight forward to predict.

## 7.2.1 Implementation

For the simulations presented here, we only consider slab shaped crystals and Laue geometries.

We use a discrete representation of the sample structure on an orthogonal grid defined by the three directions  $\hat{\mathbf{x}}$ ,  $\hat{\mathbf{y}}$ , and  $\hat{\mathbf{z}} = \hat{\mathbf{n}}$  and corresponding step sizes  $d_x$ ,  $d_y$ , and  $d_z$ . The beam enters the crystal through the surface at  $z = 0$  and, as we are only considering Laue-geometries, both the transmitted and scattered beam exit the crystal through the opposite surface.  $\hat{\mathbf{n}}$  is the outward pointing unit normal of the exit surface.

We do not need to restrict the final free rotation about the  $z$ -axis, but we get a simplification of the scattering calculation by choosing a coordinate system where the  $x$ - $z$  plane coincides with the scattering plane.

The number of grid points in each direction will be labeled  $N_x$ ,  $N_y$ , and  $N_z$ , giving a total size of the simulated domain of  $L_x = d_x(N_x - 1)$ ,  $L_y = d_y(N_y - 1)$ ,  $t = d_z(N_z - 1)$ .  $t$  is the thickness of the simulated crystal slab.

The complex value of these scattering functions needs to be known with high resolution. For simple test-cases, where the displacement field is given by an analytical expression, this is not a point of concern. If, however, the displacement field is generated by a numerical simulation, then it needs to be computed with sufficient resolution to at least match the resolution of the experiment ( $\approx 50$  nm) throughout the volume of the sample. The size of the sample can be up to several hundred micrometers.

For strained samples, the scattering function contains a phase factor of the shape  $e^{i\mathbf{Q}\cdot\mathbf{u}}$ . In order to limit the phase variation between adjacent voxels to less than  $2\pi$ , step-sizes must be below  $|\nabla\mathbf{u}|/(2\pi|Q|)$ , which means small steps must be used for highly deformed samples. In samples with nanometer-sized domains or other small structures, all structural features has to be resolved.

## 7.3 Integrating the Takagi-Taupin Equations

The Takagi-Taupin equations (TTEs) introduced in Chapter 2 are system of coupled first order PDEs and provide a way to calculate the complex envelope of scattered and transmitted beam when the amplitude of the incident beam and the structure of the sample crystal is given. In that chapter, we showed how to solve the TTEs in perfect crystals. For deformed crystals, these (semi-)analytical methods fail and we have to resort to numerical integration of the PDEs.

The TTEs are typically solved using a finite difference integration scheme. A number of different algorithms have been used in the literature, the most common being a simple 2nd order finite difference scheme called *the half-step method*[74, 6, 23]. This method uses a computational grid where two of the axes are aligned with  $\mathbf{k}_0$  and  $\mathbf{k}_h$ , respectively and therefore needs the input of the crystal displacement field given on a sheared grid.

We instead choose to use a scheme that works directly on an orthogonal input for the displacement field. To do this we implicitly utilize Fourier interpolation at the level of the individual steps in the intragration algorithm inspired by the methods outlined by Li et al.[50] that we were previously using to simulate kinematical scattering in an earlier version of the simulation. This scheme is derived and tested in the following subsection.

### 7.3.1 A novel finite difference scheme for integrating the TTEs

The TTEs on the form given in Equations (2.30) have the shape of an initial value problem in  $z$ . In order to apply boundary conditions in the two transverse directions, we assume that the initial condition given for  $E_0$  on the plane  $z = 0$  is only non-zero inside an area  $\Omega$ . Following the arguments in [72], we know that the fields are only non-zero inside a finite volume defined by the projection of  $\Omega$  along the directions of  $\mathbf{k}_0$  and  $\mathbf{k}_h$ . (see Fig 7.7) If this volume is contained inside the simulated grid, we can impose zero boundary conditions in the  $x$ - and  $y$ -directions.

This will be fulfilled if  $\Omega$  is contained in the rectangle

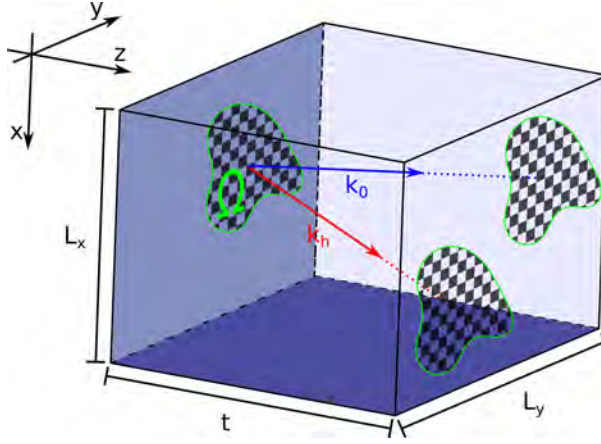


Figure 7.7: Sketch of simulation geometry. Figure reproduced from [14].

$$\max(0, tk_{0,x}/k, tk_{h,x}/k) < x < \min(L_x, L_x + tk_{0,x}/k, L_x + tk_{h,x}/k) \quad (7.4)$$

$$\max(0, tk_{0,y}/k, tk_{h,y}/k) < y < \min(L_y, L_y + tk_{0,y}/k, L_y + tk_{h,y}/k) \quad (7.5)$$

Starting from the Fourier transformed form of the TTEs in Equation (2.31), we re-write them:

$$\begin{aligned} \frac{\partial}{\partial z} \begin{bmatrix} \tilde{E}_0(s_x, s_y, z) \\ \tilde{E}_h(s_x, s_y, z) \end{bmatrix} &= \begin{bmatrix} A_{00}(s_x, s_y) & 0 \\ 0 & A_{hh}(s_x, s_y) \end{bmatrix} \begin{bmatrix} \tilde{E}_0(s_x, s_y, z) \\ \tilde{E}_h(s_x, s_y, z) \end{bmatrix} \\ &+ \begin{bmatrix} 0 & B_0 \\ B_h & 0 \end{bmatrix} \begin{bmatrix} \mathcal{F}_\perp \{ \chi'_h(x, y, z) E_0(x, y, z) \} \\ \mathcal{F}_\perp \{ \chi'_h(x, y, z) E_0(x, y, z) \} \end{bmatrix} \end{aligned} \quad (7.6)$$

where

$$\begin{aligned} A_{00}(s_x, s_y) &= \frac{-ik^2}{2k_{0,z}} \chi_0 - \frac{i2\pi}{k_{0,z}} \mathbf{s} \cdot \mathbf{k}_{0,\perp} \\ A_{hh}(s_x, s_y) &= \frac{-ik^2}{2k_{h,z}} (\chi_0 + \beta) - \frac{i2\pi}{k_{h,z}} \mathbf{s} \cdot \mathbf{k}_{0,\perp} \\ B_0 &= -\frac{ik^2}{2k_{0,z}} \\ B_h &= -\frac{ik^2}{2k_{h,z}} \end{aligned} \quad (7.7)$$

We can consider these equations to be equations for the Fourier components of the DFT of the discretized fields. In that case the last term in Eq. (7.6) has the appearance of a convolution:

$$\mathcal{F}_\perp \{ \chi'_h(x, y, z) E_0(x, y, z) \} = \mathcal{F}_\perp \left\{ \chi'_h(x, y, z) \mathcal{F}_\perp^{-1} \{ \tilde{E}_0(s_x, s_y, z) \} \right\} \quad (7.8)$$

This quantity can be numerically evaluated by replacing the Fourier transforms on the RHS by DFTs. Collecting the components of  $\tilde{E}_0$  and  $\tilde{E}_h$  into a single vector  $\mathbf{E}$ , we write the systems of equations as:

$$\frac{\partial}{\partial z} \mathbf{E} = \mathbf{A} \mathbf{E} + B(\mathbf{E}, z) \quad (7.9)$$

where  $\mathbf{A}$  is a diagonal matrix containing the values of  $A_{00}(s_x, s_y)$  and  $A_{hh}(s_x, s_y)$  evaluated on the computational grid and  $\mathbf{B}(E, z)$  contains the scattering terms. We have thereby separated the RSH into a diagonal term that is easy to integrate exactly and an off diagonal term, that we will treat with an appropriate finite difference scheme.

### Exponential Runge-Methods and convergence behaviour

The Fourier-transformed TTEs can be solved by exponential Runge-Kutta methods of the type given by [37]. To test the convergence of this approach, we utilized two different exponential integrators. The first is an archetypal exponential integrator based on the explicit Euler scheme, given by:

$$\mathbf{E}(z + h) = \exp(hA) \mathbf{E}(z) + h(hA)^{-1}(\exp(hA) - 1) \mathbf{B}(z, \mathbf{E}(z)). \quad (7.10)$$

The second exponential integrator is an explicit second-order method based on Heun's method, given by the steps: [31]

$$\begin{aligned} E_1^* &= \mathbf{E}(z), \\ b_1 &= \mathbf{B}(z_n, E_1^*), \\ E_2^* &= \phi_0 E_1^* + h \phi_1 b_1, \\ b_2 &= \mathbf{B}(z_n + h, E_2^*), \\ \mathbf{E}(z + h) &= \phi_0 E_1^* + \frac{h}{2}((2\phi_1 - \phi_2)b_1 + \phi_2 b_2), \end{aligned} \quad (7.11)$$

where the  $\phi$ -functions are given by:  $\phi_0 = \exp(hA)$  and  $\phi_n = n(hA)^{-1}(\phi_{n-1} - 1)$ , and  $\exp(hA)$  is in general the matrix-exponential which here is equal to the element-wise exponential because  $A$  is diagonal. We choose this scheme based on Heun's method because it only evaluates the  $B$  function on the same regular intervals where the field is calculated, and therefore only requires the value of the scattering function on the same grid where the fields are evaluated.

For comparison with existing methods, we also implemented a normal finite difference method based on a recent publication by Shabalin et al.[65] using the half-step finite difference for the derivatives.

To evaluate the convergence behaviour of these exponential methods, we generated a virtual sample consisting of a perfect single crystal with a single edge dislocation with Burger's vector (100) close to the path of the direct beam. Plots of the displacement field as well as the amplitudes of the converged solution are shown in figure 7.8.

The fields are simulated under low absorption and highly dynamical conditions, and we simulated only a single slice in the  $y$ -direction with the dimensions  $50 \mu\text{m} \times 115 \mu\text{m}$  at a point  $1 \mu\text{m}$  from the dislocation core. The incident beam is a narrow Gaussian of width  $\sigma = 0.2 \mu\text{m}$ , with parameters chosen corresponding to the (111) reflection of a diamond crystal with at 17 keV photon energy. The incident beam has a Gaussian envelope with width  $\sigma_x = 0.2 \mu\text{m}$

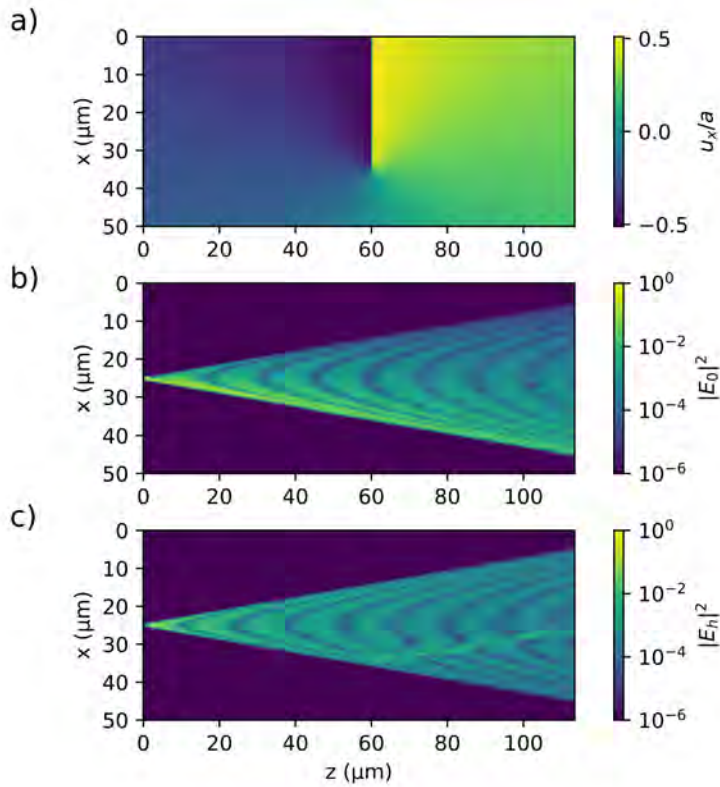


Figure 7.8: Plots of the sample and calculated fields used in the second convergence test. a) displacement field in units of the lattice constant,  $a$ . b) Transmitted field on a logarithmic scale, c) scattered field on a logarithmic scale. The calculated fields are for the case  $\beta = 0$ . Figure reproduced from [14].

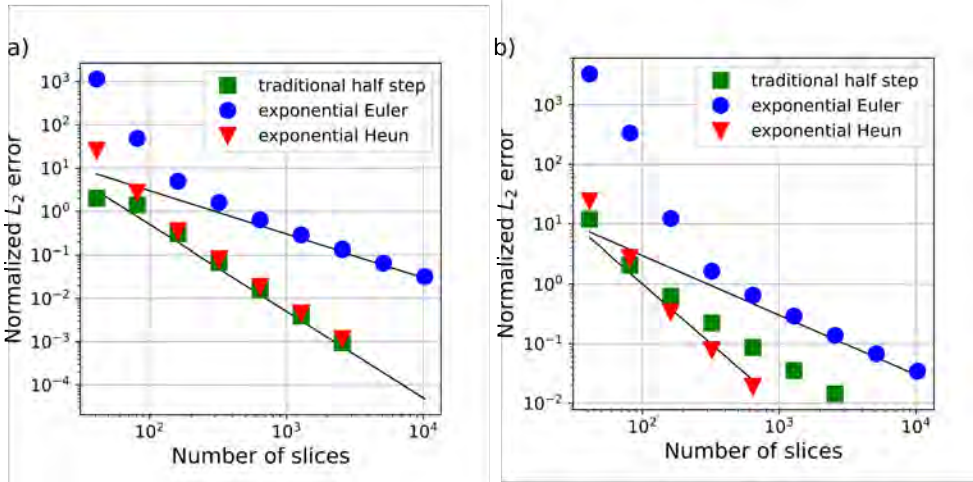


Figure 7.9: Convergence of the new exponential integrators and a traditional finite difference scheme. The black lines mark first- and second-order convergence respectively. All errors are calculated relative to the solution using the traditional half step method with 10,241 steps. We tested integration schemes on two different samples. One a) is a perfect crystal the other b) is the edge dislocation type sample shown in Fig. 7.8. All calculations are in the case  $\beta = 0$ . Figure reproduced from [14].

In order to accommodate the comparison with existing methods, we utilized a grid with step sizes  $\Delta z = h$  and  $\Delta x = 2 \tan(\theta)h$  for the exponential methods and a grid with the same density of points for the normal finite difference method. Then, to check the convergence of the methods we calculate the fields on progressively finer grids from a first grid consisting of  $101 \times 41$  points. The error represents the deviation of the exit surface amplitudes to that computed using the normal finite different approach on a very fine grid of  $10,241 \times 25,601$  steps (evaluated at the points where the coarse and fine grids coincide).

Figure 7.9 shows the convergence of the three integration methods. While all methods show the expected convergence on a perfect sample a), the traditional half-step method does not show the expected second order convergence with the edge dislocation sample b). The first order exponential Euler method suffers from an exponential instability and only gives a qualitatively correct result when impractically small step-sizes are utilized.

For the simulation presented here we use the exponential Heun scheme. Further details of the algorithm are given in.[14]

### 7.3.2 Energy-angle effect

So far we have treated the incident beam as monochromatic with a photon energy frequency  $\omega_0$ , but we would now like to handle incident illumination with a finite bandwidth. To simulate polychromatic x-rays, we simulate a number of different energy components and sum over the energies in the final step of the simulation. This is the normal approach in partially coherent wave front simulations.[20]

Consider one such energy component with frequency  $\omega$ . We introduce the relative offset in energy  $\delta E = \omega/\omega_0 - 1$  and we assume that this number is much smaller than 1. It is then natural to define the envelope-function (first defined in Eq. (2.7)) of this energy

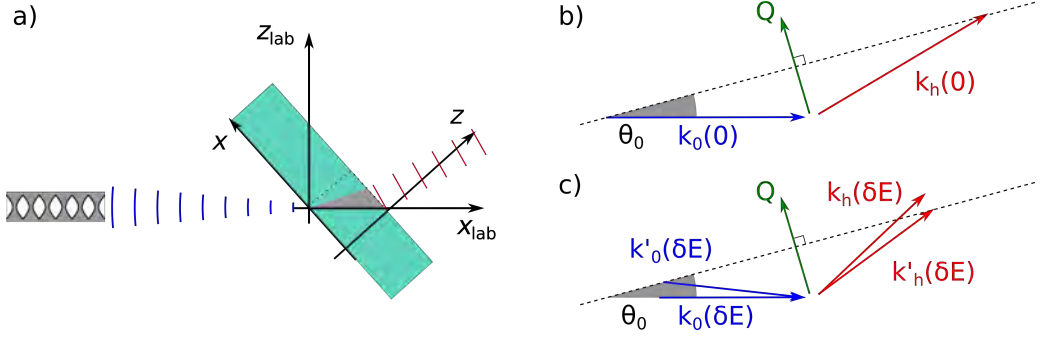


Figure 7.10: a) Sketch of the experimental geometry in a non-symmetric Laue geometry in laboratory coordinates with the coordinated used in the scattering calculation given as  $x$  and  $y$ . b) Reciprocal space geometry for the central energy component,  $\delta E = 0$ . c) Reciprocal space geometry for a different energy component with  $\delta E < 0$ .

component with the  $k$ -vector,  $\mathbf{k}_0(\delta E) = \mathbf{k}_0(0)(1 + \delta E)$ .

$$\mathbf{E}(r, \delta E) = E_0 e^{-i\mathbf{k}_0(\delta E) \cdot \mathbf{r}} \quad (7.12)$$

This wave-vector, however, does not satisfy the Bragg-condition. When we derived the Takagi-Taupin Equations, we assumed exact satisfaction of the Bragg-condition, which means we need to choose a different wave-vector,  $\mathbf{k}'_0(\delta E)$ , that satisfies the Bragg-condition exactly. (see Fig. 7.10)

If the central energy component, with energy  $\omega_0$ , satisfies the Bragg-condition with a Bragg angle of  $\theta_0$ , the  $\delta E$  energy component satisfies the Bragg-condition with an angle:

$$\theta(\delta E) = \arcsin\left(\frac{c}{2\omega_0}(\delta E + 1)|\mathbf{Q}|\right) \approx \theta_0 + \tan(\theta_0)\delta E \quad (7.13)$$

where the last expression results from a 1st order Taylor expansion of the second. In laboratory coordinates, we therefore have:

$$\mathbf{k}'_0(\delta E) = k(1 + \delta)(\cos(\theta(\delta E) - \theta_0)\hat{\mathbf{x}}_{lab} + \sin(\theta(\delta E) - \theta_0)\hat{\mathbf{z}}_{lab}) \quad (7.14)$$

To account for this, the initial condition has to be modified by a factor  $e^{-i[\mathbf{k}_0(\delta E) - \mathbf{k}'_0(\delta E)] \cdot \mathbf{r}}$  when going from the laboratory space to the coordinates used for the scattering calculation and back. To demonstrate the energy-angle correlations and to test the implementation, we perform a simulation of the scattering by a perfect crystal using the perfect crystal propagators of Section 2.2.3.

Figure 7.11 a) shows the power spectral density of the scattered beam as a function of the simulated photon energy. The peak intensity follows the trend predicted by Eq. (7.13) but is has a small constant offset due to refraction of the x-rays. The scattered beam has a limited width and oscillatory features due to the finite width of the crystal and multiple scattering effects. When we integrate over the energy the oscillations are lost and the width is determined by the energy bandwidth of the incident light. Figure 7.11 b) shows the power spectral density integrated over photon energy as a function of rocking angle. The maximum follows see the expected  $\Delta 2\theta = \phi$  trend predicted by the geometric

theory. When the rocking angle becomes higher than the NA of the condenser aperture, the scattering disappears.

Figures 7.11 c,d) illustrate the geometric-optics interpretation of these effects. At  $\phi = 0$ , the Bragg condition intersects the phase space density of the incident light at an angle  $\theta$ . When the sample is rotated the Bragg condition travels up-and-down the angular spectrum of the incident beam and eventually “falls off the rocking curve”. Therefore the scattered beam intensity as a function of rocking angle maps out the spectrum of the incident beam in a distorted coordinate system. This figure differs from the measured curves (Fig. 3.3b) because it does not account for the aperture of the objective lens, which effectively blurs the pattern along the  $\Delta 2\theta$  direction.

## 7.4 Propagating through the imaging forming optics

To model the propagation of the scattered x-ray beam from the exit-surface of the sample through the objective lens to the detector, we make use of the quadratic phase propagators described in Section 5.2. Numerical modeling of CRLs was already dealt with at length in that section.

In the DFXM experiments, the objective lens is aligned with the scattered beam, which is at an angle  $2\theta_0$  relative to the incident beam and therefore not aligned with any special direction of the laboratory coordinate system. We therefore introduce a new coordinate system, *the imaging coordinate system*, with the  $z_{\text{img}}$ -axis aligned with  $\mathbf{k}_h$  and the  $y$ -axis orthogonal to the scattering plane.

To bridge the gap between the two coordinate systems, we project the points of the computational grid on the exit-surface onto the  $z_{\text{img}} = 0$  plane and keep the value of the complex amplitudes. This way we omit diffraction effects that take place in the gap between these two planes. This is commonly done in wave-optical simulations involving Bragg-scattering. [71, 65]

Both the focusing length and the absorbing aperture of the CRL is a function of the photon energy, through the energy dependence of  $\chi_0$ . Most critical is the focus length. The photon energies typically used are far above any transition lines of Be, so  $\text{Re}(\chi_0)$  scales as one over photon energy squared. Therefore, the focal length scales as the energy squared. With a typical focus-length of 300 mm and relative energy bandwidth of  $10^{-4}$ , the focus length varies by 0.06 mm which is comparable to the thickness of the sample but small compared to the depth-of-focus and, as was also found in [56], we find that the chromaticity of the lenses only adds a small contribution to the overall point-spread of the CRL. This effect is included in our simulations but does not give a noticeable effect in the final images.

When the beam has been propagated to the detector-plane, we incoherently sum over the modes of the beam to find the x-ray intensity on the detector. The effect of the detector is included by convoluting this intensity by a incoherent point spread function characteristic to the detector. This blurred intensity is then interpolated to the positions of the detector pixels to yield the image intensities. Counting- and read-out noise can be added to simulate other non-ideal behavior of the detector.

The detector used at the ID06-HXM is an indirect detector composed of a thin scintillator screen and an optical microscope. The spatial resolution of the combined detector depends both on the characteristics of the scintillator screen and of the optical microscope. A detailed characterization of the detector used at the ESRF was not possible. A Gaussian point spread with a FWHM of  $1.5 \mu\text{m}$ , about two times the effective pixel size, was

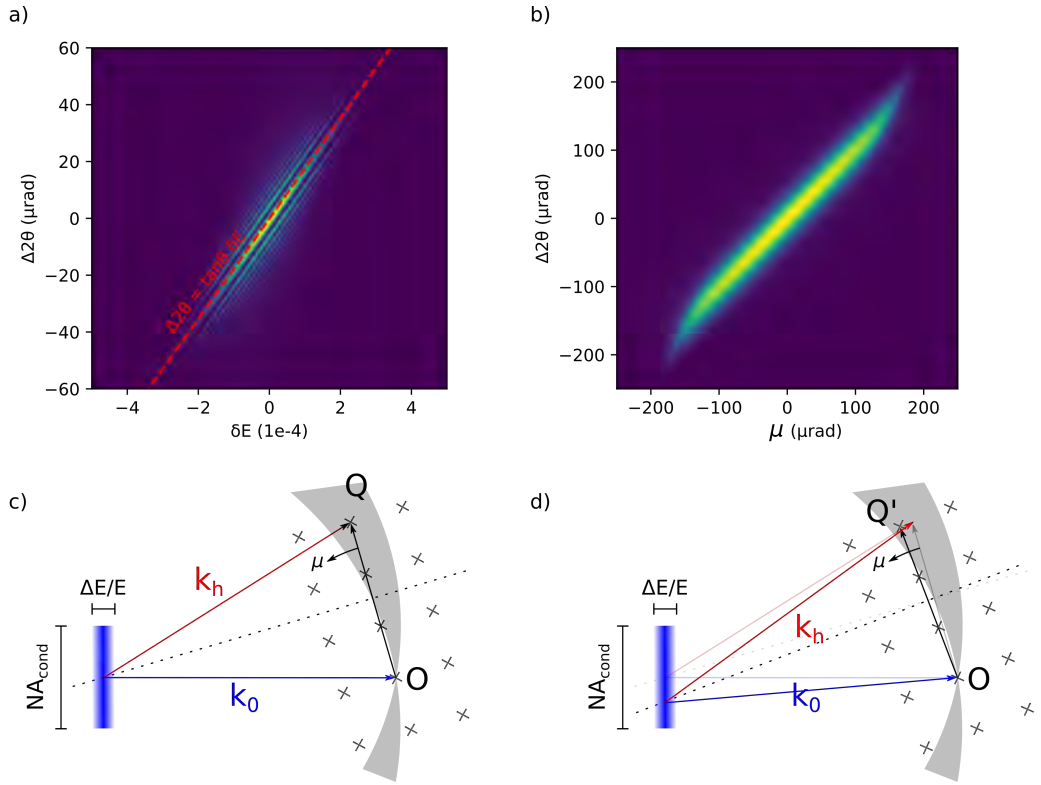


Figure 7.11: a) Simulated power spectral density of the beam scattered by a perfect crystal as a function of the relative photon energy. The red dashed line marks the Bragg-condition. b) Simulated power spectral density integrated over the photon energy as a function of rocking angle. The simulations were done for a perfect Aluminium crystal (111) reflection using the parameters of Table 7.1. c) Ewald-construction for the simulated geometry in laboratory coordinates at zero rocking angle. The blue rectangle marks the phase-space density of the incident beam with its characteristic dimensions given by the energy bandwidth and the numerical aperture of the condenser lens. The dotted line marks the Bragg condition.  $O$  is the origin in reciprocal space,  $Q$  is the probed reciprocal lattice vector. d) Ewald-construction at a finite positive rocking angle. The reciprocal lattice and  $Q$  have been rotated by an angle  $\mu$  around the origin. The result is a scattered beam at a higher angle compared to c).

assumed for the simulations shown here.

## 7.5 Comparison with experiment

We want to test our simulation by comparison with an experiment. We therefore need a test sample where we know the structure beforehand, so that we can model the scattering. This necessarily means that we need a near perfect crystal with a low defect concentration so that we can find an isolated ideal defect. We find this in a high-pressure high-temperature diamond made as a phase-plate for x-ray optical purposed in which we know there to be a few isolated dislocations and stacking faults.

The stacking fault is a planar defect, which arises by the addition or removal of a single close-packed plane of atoms in the FCC parent-lattice of the diamond. This can be seen as a discontinuous jump in the value of the displacement field. The magnitude of this jump is a vector of the family  $\mathbf{b}_{\text{sf}} = \frac{1}{3}\langle 111 \rangle$  which is not a symmetry of the fcc lattice. These planar defects are bounded either by the surfaces of the crystal and or by Frank-type partial dislocations.[30, 45]

Sufficiently far away from these bounding dislocations, the stacking fault can be regarded as an ideal flat discontinuity of the displacement field and therefore in the TTE-formalism, a discrete jump in the phase of the scattering function of magnitude  $2\pi[hk\ell] \cdot \mathbf{b}_{\text{sf}} = \pm 2/3\pi$  when imaged using any  $[111]$  reflection that is not orthogonal to the stacking fault normal. In this way the stacking fault can be seen as a prototype of the inversion twin domain boundary, which has been discussed earlier. The dynamical scattering patterns produced by isolated stacking faults in diamonds have previously been studied in detail by classical x-ray topography.[45]

Figure 7.5 show a near-field measurement of a sample containing such a stacking fault. The image contains a bright feature, called the direct image, going diagonally through from edge to edge of the crystal. The dynamical fringes found in a perfect crystal are disturbed in a characteristic hourglass shape around the direct image.

Figure 7.12 shows the result of the full DFXM simulation and experimental data with two different positions of the objective lens and a comparison to experimental data. The region is a zoomed in image compared to Fig. 7.5 showing only one edge of the crystal and most of the direct image. The center of the hourglass shape appears on the right-hand side of these images. In the experimental images, the direct image of the stacking fault was over-exposed, so when plotting the images, we choose a colormap that clips the highest intensities. The simulation qualitatively recreates the features of the experimental images. However, there are a number of deviations:

- We underestimate the magnification of the imaging set-up by about 5%. As discussed in section 5.2.1 we believe this deviation to be due to systematic production errors of the Be lenses.
- The simulated images contain a smaller number of dynamical fringes than the measured data. This error could be due to an error of any number of parameters. The photon energy, the crystal thickness, or the scattering constant.
- The simulated images have a regular pattern of vertical streaks close to the right hand side of the images that are not seen in the measured images. These are Fresnel diffraction fringes and appear because we assume the edges of the aperture to be perfectly sharp and because we assume that the light is perfectly coherent in the transverse direction.

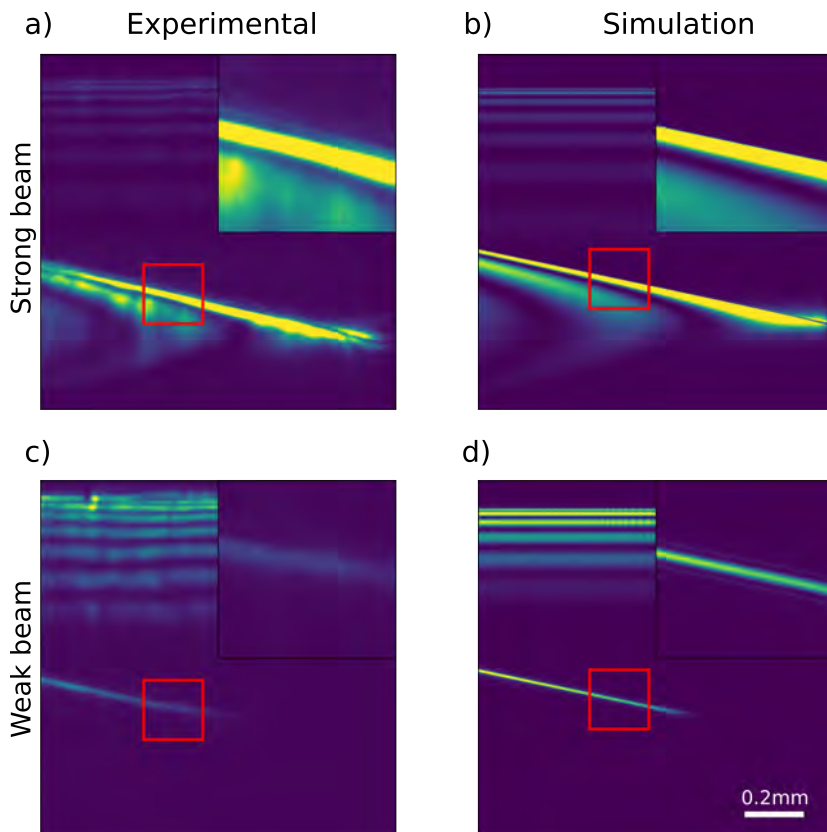


Figure 7.12: Measured (a,c) and simulated (b,d) DFXM images of a stacking fault defect in a diamond single crystal. (a,b) show images where the objective lens is placed in the center of the diffracted beam. (c,d) show images where the lens is displaced from the diffracted beam leaving the bottom half of the FOV in the dark field. The dotted white line marks the edge of the Borrmann triangle. Figure reproduced from [12].

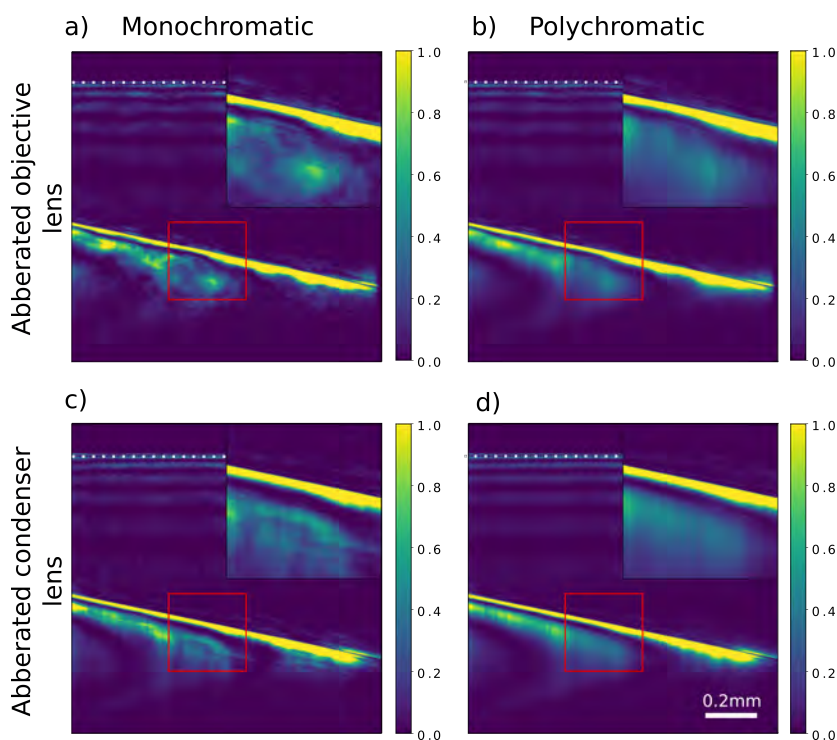


Figure 7.13: a) Monochromatic and b) polychromatic simulation using an aberrated objective lens. c) Monochromatic and d) polychromatic simulation using an aberrated condenser lens. The scale bar refers to distances on the detector. Figure reproduced from [12].

- The measured images contain noise with the appearance of vertical streaks and speckle-like features close to the brightest features,. This can be explained either by the aberrations in the condenser lens or in the objective lens.

So far, we have ignored the effect of the aberrations in the lenses. In the transmission and thin-film diffraction images shown in the previous chapter we see that aberrations in the objective lens cause strong noise features in the images when the decoherer is not included. The experimental images in Fig. 7.12a,c) also contains noise that is not present in the simulated image. This noise, compared to the features observed in the transmission images appears to be less strong and appear to vary more quickly in the horizontal (normal to the scattering plane) than the vertical direction. We know that low coherence averages out this speckle noise. In this case, the averaging out is caused by the finite energy bandwidth of the incident light and the "energy-angle effect" discussed in Section 7.4.

Figure 7.13 a) shows a simulated image with an aberrated objective lens but assuming a monochromatic source. In this image, we see strong noise similar to that observed in transmission images. When we include the finite bandwidth in the simulation (Fig. 7.13 b) ) this noise gets partially averaged out and what remains is weaker noise that has the appearance of vertical stripes similar to those observed in the experimental images.

In Fig. 7.13 c,d) we look at the effect of including the same type of aberrations in the condenser lens instead of the objective lens. We again see that the polychromatic simu-

lation has less strong noise than the monochromatic. Also, like before the noise has the appearance of vertical stripes but in this case the noise appears a full unbroken lines that can be traces from the top to the bottom of the images rather than the short stripes seen in the experimental images.

## 7.6 Future prospects for simulations

The simulation described in this chapter is quite flexible and can be used to simulate the scattering pattern of near perfect crystals containing a range of different crystal defects. The main obstacle to applying these simulations is to construct a model of sample's microstructure. Aside from a number of ideal defects, dislocations, domain walls, stacking faults, and point defects, we can also construct combinations of ideal defects such as low-angle domain boundaries (regular arrays of dislocations) and lamellar twin-domain patterns can be constructed by combining several of these ideal defects, but more realistic models of the sample micro-structure are hard to come by.

Another idea is to use the output of numerical modeling methods such as phase-field models, commonly used to simulate ferroelectric domain structures,[87] as an input for the optical simulation. In general though, it will be difficult to come up with a model of the micro-structure that matches a real sample, since DFXM images appear quite chaotic.

The computation time of the simulations presented here might prove to be an obstacle for applying such simulation more widely.

The simulations presented here used a grid of  $2048 \times 2048 \times 3001$  points with corresponding step sizes of 60 nm, 60 nm, and 100 nm respectively. This matches the  $300 \mu\text{m}$  thickness of the sample and gives a simulated FOV of  $\approx 100 \mu\text{m}$  in the transverse directions. The step sizes here are chosen small enough that the nearfield phase factors and the objective lens aperture are well sampled, but for a more disordered sample, smaller step-sizes might be necessary.

The execution time is dominated by the integration of the Takagi-Taupin equations, which took 3.5 hours per energy mode running on a single core. The simulation was parallelized over the modes. The use of computer resources scales linearly with the number of modes, so if a transversely incoherent model was to be used, the needed resources would increase with a factor of the number of modes. In the study presented here computation time was not an issue, but if high throughput simulation was needed, large performance gains could likely be achieved by applying a more efficient algorithm for the integration of the TTEs.



# Bibliography

- [1] Ernst Abbe. Beiträge zur theorie des mikroskops und der mikroskopischen wahrnehmung. *Archiv für Mikroskopische Anatomie*, 9:413–468, 1873.
- [2] S. R. Ahl, H. Simons, Y. B. Zhang, C. Detlefs, F. Stohr, A. C. Jakobsen, D. Juul Jensen, and H. F. Poulsen. Ultra-low-angle boundary networks within recrystallizing grains. *SCRIPTA MATERIALIA*, 139:87–91, OCT 2017.
- [3] Sonja Rosenlund Ahl. *Elements of a Method for Multiscale Characterization of Recrystallization in Deformed Metals*. PhD thesis, 2018.
- [4] J. Als-Nielsen and D. McMorrow. *Elements of Modern X-ray Physics*. Wiley, 2011.
- [5] G. Artl and P. Sasko. Domain configuration and equilibrium size of domains in BaTiO<sub>3</sub> ceramics. *Journal of Applied Physics*, 51(9):4956–4960, 1980.
- [6] A. Authier, C. Malgrange, and M. Tournarie. Etude théorique de la propagation des rayons X dans un cristal parfait ou légèrement déformé. *Acta Crystallographica Section A*, 24(1):126–136, Jan 1968.
- [7] W Berg. Über eine röntgenographische Methode zur Untersuchung von Gitterstörungen an Kristallen. *NATURWISSENSCHAFTEN*, 19:391–396, 1931.
- [8] Pierre Bon, Serge Monneret, and Benoit Wattellier. Noniterative boundary-artifact-free wavefront reconstruction from its derivatives. *Appl. Opt.*, 51(23):5698–5704, Aug 2012.
- [9] M. Born and Wolf. *Principles of Optics*. Cambridge University Press, 1959.
- [10] W. R. Busing and H. A. Levy. Angle calculations for 3- and 4-circle X-ray and neutron diffractometers. *Acta Crystallographica*, 22(4):457–464, Apr 1967.
- [11] R.W. Cahn. Twinned crystals. *Advances in Physics*, 3(12):363–445, 1954.
- [12] Mads Carlsen, Carsten Detlefs, Can Yildirim, Trygve M Ræder, and Hugh Simons. Simulating dark-field x-ray microscopy images with wave front propagation techniques. *Acta Crystallographica Section A*, 2022. (in press).
- [13] Mads Carlsen, Trygve M Ræder, Can Yildirim, Raquel Rodriguez-Lamas, Carsten Detlefs, and Hugh Simons. Fourier ptychographic dark field x-ray microscopy. *Opt. Express*, 30(2):2949–2962, Jan 2022.
- [14] Mads Carlsen and Hugh Simons. A finite difference scheme for integrating the Takagi–Taupin equations on an arbitrary orthogonal grid. *Acta Crystallographica Section A*, 78(5), Sep 2022.
- [15] Rafael Celestre, Oleg Chubar, Thomas Roth, Manuel Sanchez del Rio, and Raymond Barrett. Recent developments in X-ray lens modelling with SRW. In Oleg Chubar and Kawal Sawhney, editors, *Advances in Computational Methods for X-Ray Optics V*, volume 11493, pages 88 – 101. International Society for Optics and Photonics, SPIE, 2020.
- [16] Chunguang Chen, Tao Zhou, Dmitri L. Danilov, Lu Gao, Svenja Benning, Nino Schoen, Samuel Tardif, Hugh Simons, Florian Hausen, Tobias U. Schulli, R-A Eichel,

and Peter H. L. Notten. Impact of dual-layer solid-electrolyte interphase inhomogeneities on early-stage defect formation in Si electrodes. *NATURE COMMUNICATIONS*, 11(1), JUL 1 2020.

- [17] Shun-Yu Cheng, New-Jin Ho, and Hong-Yang Lu. Transformation-induced twinning: The 90° and 180° ferroelectric domains in tetragonal barium titanate. *Journal of the American Ceramic Society*, 89(7):2177–2187, 2006.
- [18] Y.-H. Chu, Q. Zhan, L. W. Martin, M. P. Cruz, P.-L. Yang, G. W. Pabst, F. Zavaliche, S.-Y. Yang, J.-X. Zhang, L.-Q. Chen, D. G. Schlom, I.-N. Lin, T.-B. Wu, and R. Ramesh. Nanoscale domain control in multiferroic bifeo<sub>3</sub> thin films. *Advanced Materials*, 18(17):2307–2311, 2006.
- [19] Oleg Chubar and Rafael Celestre. Memory and cpu efficient computation of the fresnel free-space propagator in fourier optics simulations. *Opt. Express*, 27(20):28750–28759, Sep 2019.
- [20] Oleg Chubar, Yong S. Chu, Konstantine Kaznatcheev, and Hanfei Yan. Application of partially coherent wavefront propagation calculations for design of coherence-preserving synchrotron radiation beamlines. *Nuclear Instruments and Methods in Physics Research Section A: Accelerators, Spectrometers, Detectors and Associated Equipment*, 649(1):118–122, 2011. National Synchrotron Radiation Instrumentation conference in 2010.
- [21] Peter Cloetens, Raymond Barrett, José Baruchel, Jean-Pierre Guigay, and Michel Schlenker. Phase objects in synchrotron radiation hard x-ray imaging. *Journal of Physics D: Applied Physics*, 29(1):133–146, jan 1996.
- [22] Leora E. Dresselhaus-Marais, Grethe Winther, Marylesa Howard, Arnulfo Gonzalez, Sean R. Breckling, Can Yildirim, Philip K. Cook, Mustafacan Kutsal, Hugh Simons, Carsten Detlefs, Jon H. Eggert, and Henning Friis Poulsen. In situ visualization of long-range defect interactions at the edge of melting. *Science Advances*, 7(29):eabe8311, 2021.
- [23] Y. Epelboin and A. Soyer. Simulation of X-ray traverse topographs by means of a computer. *Acta Crystallogr. A*, 41(1):67–72, Jan 1985.
- [24] J. Erhart. Domain wall orientations in ferroelastics and ferroelectrics. *Phase Transitions*, 77(12):989–1074, 2004.
- [25] ESRF. "ESRF upgrade program phase II (2015-2022) - Technical Design Study (Orange book)". 2022.
- [26] PP Ewald. On the explanation of crystal optics. *ANNALEN DER PHYSIK*, 54(23):519–556, 1917.
- [27] Ken Vidar Falch, Carsten Detlefs, Magnus Sebastian Christensen, David Paganin, and Ragnvald Mathiesen. Experimental investigation of gaussian random phase screen model for x-ray diffusers. *Opt. Express*, 27(15):20311–20322, Jul 2019.
- [28] J. Fousek and P. Mokry. Stress-free domain quadruplets in ferroics. *Ferroelectrics*, 323(1):3–9, 2005.
- [29] Jan Fousek and Vaclav Janovec. The orientation of domain walls in twinned ferroelectric crystals. *Journal of Applied Physics*, 40(1):135–142, 1969.

- [30] F.C. Frank. Lxxxiii. crystal dislocations.—elementary concepts and definitions. *The London, Edinburgh, and Dublin Philosophical Magazine and Journal of Science*, 42(331):809–819, 1951.
- [31] A. Friedli. Verallgemeinerte Runge-Kutta Verfahren zur Lösung steifer Differentialgleichungssysteme. In *Numerical treatment of differential equations (Proc. Conf., Math. Forschungsinst., Oberwolfach, 1976)*, pages 35–50. Lecture Notes in Math., Vol. 631, 1978.
- [32] Semën Gorfman, Hyeokmin Choe, Guanjie Zhang, Nan Zhang, Hiroko Yokota, Anthony Michael Glazer, Yujuan Xie, Vadim Dyadkin, Dmitry Chernyshov, and Zuo-Guang Ye. New method to measure domain-wall motion contribution to piezoelectricity: the case of  $\text{PbZr}_{0.65}\text{Ti}_{0.35}\text{O}_3$  ferroelectric. *Journal of Applied Crystallography*, 53(4):1039–1050, Aug 2020.
- [33] Semën Gorfman, David Spirito, Guanjie Zhang, Carsten Detlefs, and Nan Zhang. Identification of a coherent twin relationship from high-resolution reciprocal-space maps. *Acta Crystallographica Section A*, 78(3):158–171, May 2022.
- [34] Manuel Guizar-Sicairos, Samuel T. Thurman, and James R. Fienup. Efficient sub-pixel image registration algorithms. *Opt. Lett.*, 33(2):156–158, Jan 2008.
- [35] Detlev Hennings. Barium titanate based ceramic materials for dielectric use. *International Journal of High Technology Ceramics*, 3(2):91–111, 1987.
- [36] John Price Hirth and Jens Lothe. *Theory of Dislocations*. Krieger Pub Co, 1992.
- [37] Marlis Hochbruck and Alexander Ostermann. Exponential integrators. *Acta Numerica*, 19:209–286, 2010.
- [38] S. O. Hruszkewycz, M. Allain, M. V. Holt, C. E. Murray, J. R. Holt, P. H. Fuoss, and V. Chamard. High-resolution three-dimensional structural microscopy by single-angle Bragg ptychography. *NATURE MATERIALS*, 16(2):244–251, FEB 2017.
- [39] Lei Huang, Mourad Idir, Chao Zuo, Konstantine Kaznatcheev, Lin Zhou, and Anand Asundi. Comparison of two-dimensional integration methods for shape reconstruction from gradient data. *Optics and Lasers in Engineering*, 64:1–11, 2015.
- [40] Jürgen Härtwig. Hierarchy of dynamical theories of x-ray diffraction for deformed and perfect crystals. *Journal of Physics D: Applied Physics*, 34(10A):A70–A77, may 2001.
- [41] L. Katz and H. D. Megaw. The structure of potassium niobate at room temperature: the solution of a pseudosymmetric structure by Fourier methods. *Acta Crystallographica*, 22(5):639–648, May 1967.
- [42] H Klapper. X-Ray topography of twinned crystals. *Prog. Cryst. Growth Charact. Mater.*, 14:367–401, 1987.
- [43] V. G. Kohn. On the theory of x-ray refractive optics: Exact solution for a parabolic medium. *Journal of Experimental and Theoretical Physics Letters*, 76(10):600–603, 2002.
- [44] Pavan Chandra Konda, Lars Loetgering, Kevin C. Zhou, Shiqi Xu, Andrew R. Harvey, and Roarke Horstmeyer. Fourier ptychography: current applications and future promises. *Opt. Express*, 28(7):9603–9630, Mar 2020.

- [45] G Kowalski, A R Lang, A P W Makepeace, and M Moore. Studies of stacking-fault contrast by synchrotron x-ray section topography. *J. Appl. Crystallogr.*, 22(5):410–430, OCT 01 1989.
- [46] M Kutsal, P Bernard, G Berruyer, P K Cook, R Hino, A C Jakobsen, W Ludwig, J Ormstrup, T Roth, H Simons, K Smets, J X Sierra, J Wade, P Wattecamps, C Yildirim, H F Poulsen, and C Detlefs. The ESRF dark-field x-ray microscope at ID06. *IOP Conference Series: Materials Science and Engineering*, 580(1):012007, aug 2019.
- [47] AR LANG. A METHOD FOR THE EXAMINATION OF CRYSTAL SECTIONS USING PENETRATING CHARACTERISTIC X-RADIATION. *ACTA METALLURGICA*, 5(7):358–364, 1957.
- [48] M. v. Laue. Die Absorption der Röntgenstrahlen in Kristallen im Interferenzfall. *Acta Crystallographica*, 2(2):106–113, Apr 1949.
- [49] M. von Laue. Die dynamische Theorie der Röntgenstrahlinterferenzen in neuer Form. *Ergebn. d. Exakten Naturwiss.*, 10:133–158, 1931.
- [50] P. Li, S. Maddali, A. Pateras, I. Calvo-Almazan, S.O. Hruszkewycz, W. Cha, V. Chamard, and M. Allain. General approaches for shear-correcting coordinate transformations in Bragg coherent diffraction imaging. Part II. *Journal of Applied Crystallography*, 53(2):404–418, Apr 2020.
- [51] Ivan Lyatun, Peter Ershov, Irina Snigireva, and Anatoly Snigirev. Impact of beryllium microstructure on the imaging and optical properties of X-ray refractive lenses. *J. Synchrotron Rad.*, 27(1):44–50, JAN 1 2020.
- [52] Andrew M. Maiden and John M. Rodenburg. An improved ptychographical phase retrieval algorithm for diffractive imaging. *Ultramicroscopy*, 109(10):1256–1262, 2009.
- [53] Jeppe Ormstrup, Emil V. Østergaard, Magnus S. Christensen, Can Yildirim, Philip K. Cook, Mustafacan Kutsal, Thomas Olsen, and Hugh Simons. Bulk heterogeneity in barium titanate above the curie temperature. *Applied Physics Letters*, 119(20):202901, 2021.
- [54] Jeppe Ormstrup, Emil V. Østergaard, Carsten Detlefs, Ragnvald H. Mathiesen, Can Yildirim, Mustafacan Kutsal, Philip K. Cook, Yves Watier, Carlos Cosculluela, and Hugh Simons. Imaging microstructural dynamics and strain fields in electro-active materials in situ with dark field x-ray microscopy. *Review of Scientific Instruments*, 91(6):065103, 2020.
- [55] H.M. Ozaktas, O. Arikan, M.A. Kutay, and G. Bozdogt. Digital computation of the fractional fourier transform. *IEEE Transactions on Signal Processing*, 44(9):2141–2150, 1996.
- [56] Anders Filsøe Pedersen, Hugh Simons, Carsten Detlefs, and Henning Friis Poulsen. The fractional fourier transform as a simulation tool for lens-based x-ray microscopy. *Journal of Synchrotron Radiation*, 25(3), 2018.
- [57] H. F. Poulsen, P. K. Cook, H. Leemreize, A. F. Pedersen, C. Yildirim, M. Kutsal, A. C. Jakobsen, J. X. Trujillo, J. Ormstrup, and C. Detlefs. Reciprocal space mapping and strain scanning using X-ray diffraction microscopy. *Journal of Applied Crystallography*, 51(5):1428–1436, Oct 2018.

- [58] H. F. Poulsen, L. E. Dresselhaus-Marais, M. A. Carlsen, C. Detlefs, and G. Winther. Geometrical-optics formalism to model contrast in dark-field X-ray microscopy. *Journal of Applied Crystallography*, 54(6):1555–1571, Dec 2021.
- [59] H. F. Poulsen, A. C. Jakobsen, H. Simons, S. R. Ahl, P. K. Cook, and C. Detlefs. X-ray diffraction microscopy based on refractive optics. *Journal of Applied Crystallography*, 50(5):1441–1456, Oct 2017.
- [60] J. M. Rodenburg and H. M. L. Faulkner. A phase retrieval algorithm for shifting illumination. *Applied Physics Letters*, 85(20):4795–4797, 2004.
- [61] Angel Rodriguez-Fernandez, Ana Diaz, Anand H. S. Iyer, Mariana Verezhak, Klaus Wakonig, Magnus H. Colliander, and Dina Carbone. Imaging ultrafast dynamical diffraction wave fronts in strained si with coherent x rays. *Phys. Rev. Lett.*, 127:157402, Oct 2021.
- [62] J. Sapriel. Domain-wall orientations in ferroelastics. *Phys. Rev. B*, 12:5128–5140, Dec 1975.
- [63] Vanessa Schoeppler, Phil K. Cook, Carsten Detlefs, Raffaella Demichelis, and Igor Zlotnikov. Untangling the mechanisms of lattice distortions in biogenic crystals across scales. *Advanced Materials*, 34(28):2200690, 2022.
- [64] Jan Schultheiß, Lukas Porz, Lalitha Kodumudi Venkataraman, Marion Höfling, Can Yildirim, Phil Cook, Carsten Detlefs, Semën Gorfman, Jürgen Rödel, and Hugh Simons. Quantitative mapping of nanotwin variants in the bulk. *Scripta Materialia*, 199:113878, 2021.
- [65] A. G. Shabalin, O. M. Yefanov, V. L. Nosik, V. A. Bushuev, and I. A. Vartanyants. Dynamical effects in bragg coherent x-ray diffraction imaging of finite crystals. *Phys. Rev. B*, 96(6):064111, Aug 2017.
- [66] H. Simons, A. King, W. Ludwig, C. Detlefs, W. Pantleon, S. Schmidt, F. Stöhr, I. Snigireva, A. Snigirev, and H. F. Poulsen. Dark-field x-ray microscopy for multiscale structural characterization. *Nature Communications*, 6-98(6), 2015.
- [67] Hugh Simons, Sonja Rosenlund Ahl, Henning Friis Poulsen, and Carsten Detlefs. Simulating and optimizing compound refractive lens-based X-ray microscopes. *Journal of Synchrotron Radiation*, 24(2):392–401, Mar 2017.
- [68] Hugh Simons, Astri Bjørnetun Haugen, Anders Clemen Jakobsen, Søren Schmidt, Frederik Stöhr, Marta Majkut, Carsten Detlefs, John E. Daniels, Dragan Damjanovic, and Henning Friis Poulsen. Long-range symmetry breaking in embedded ferroelectrics. *Nature Materials*, 17(9):814–819, 2018.
- [69] Hugh Simons, Anders Clemen Jakobsen, Sonja Rosenlund Ahl, Henning Friis Poulsen, Wolfgang Pantleon, Ying-Hao Chu, Carsten Detlefs, and Nagarajan Valanoor. Nondestructive mapping of long-range dislocation strain fields in an epitaxial complex metal oxide. *Nano Letters*, 19(3):1445–1450, 2019.
- [70] A. Starikov and E. Wolf. Coherent-mode representation of gaussian schell-model sources and of their radiation fields. *J. Opt. Soc. Am.*, 72(7):923–928, Jul 1982.
- [71] John P. Sutter, Oleg Chubar, and Alexey Suvorov. Perfect crystal propagator for physical optics simulations with Synchrotron Radiation Workshop. In Manuel Sanchez del Rio and Oleg Chubar, editors, *Advances in Computational*

*Methods for X-Ray Optics III*, volume 9209, pages 171 – 185. International Society for Optics and Photonics, SPIE, 2014.

- [72] S. Takagi. Dynamical theory of diffraction applicable to crystals with any kind of small distortion. *Acta Crystallographica*, 15(12):1311–1312, Dec 1962.
- [73] S TAKAGI. A DYNAMICAL THEORY OF DIFFRACTION FOR A DISTORTED CRYSTAL. *JOURNAL OF THE PHYSICAL SOCIETY OF JAPAN*, 26(5):1239–&, 1969.
- [74] D TAUPIN. THEORIE DYNAMIQUE DE LA DIFFRACTION DES RAYONS X PAR LES CRISTAUX DEFORMES. *BULLETIN DE LA SOCIETE FRANCAISE MINERALOGIE ET DE CRISTALLOGRAPHIE*, 87(4):469–&, 1964.
- [75] Pierre Thibault, Martin Dierolf, Oliver Bunk, Andreas Menzel, and Franz Pfeiffer. Probe retrieval in ptychographic coherent diffractive imaging. *Ultramicroscopy*, 109(4):338–343, 2009.
- [76] Lei Tian and Laura Waller. Quantitative differential phase contrast imaging in an led array microscope. *Opt. Express*, 23(9):11394–11403, May 2015.
- [77] N. T. Tsou, P. R. Potnis, and J. E. Huber. Classification of laminate domain patterns in ferroelectrics. *Phys. Rev. B*, 83:184120, May 2011.
- [78] IA Vartanyants and MV Kovalchuk. Theory and applications of x-ray standing waves in real crystals. *REPORTS ON PROGRESS IN PHYSICS*, 64(9):1009–1084, SEP 2001.
- [79] Mariana Verezhak, Steven Van Petegem, Angel Rodriguez-Fernandez, Pierre Godard, Klaus Wakonig, Dmitry Karpov, Vincent L. R. Jacques, Andreas Menzel, Ludovic Thilly, and Ana Diaz. X-ray ptychographic topography: A robust nondestructive tool for strain imaging. *Phys. Rev. B*, 103:144107, Apr 2021.
- [80] Klaus Wakonig, Ana Diaz, Anne Bonnin, Marco Stampanoni, Anna Bergamaschi, Johannes Ihli, Manuel Guizar-Sicairos, and Andreas Menzel. X-ray fourier ptychography. *Science Advances*, 5(2):eaav0282, 2019.
- [81] Timm Weitkamp, Bernd Nöhammer, Ana Diaz, Christian David, and Eric Ziegler. X-ray wavefront analysis and optics characterization with a grating interferometer. *Applied Physics Letters*, 86(5):054101, 2005.
- [82] Harold H. Wen, Eric E. Bennett, Rael Kopace, Ashley F. Stein, and Vinay Pai. Single-shot x-ray differential phase-contrast and diffraction imaging using two-dimensional transmission gratings. *Opt. Lett.*, 35(12):1932–1934, Jun 2010.
- [83] Emil Wolf. New theory of partial coherence in the space–frequency domain. part i: spectra and cross spectra of steady-state sources. *J. Opt. Soc. Am.*, 72(3):343–351, Mar 1982.
- [84] C. Yildirim, C. Jessop, J. Ahlström, C. Detlefs, and Y. Zhang. 3d mapping of orientation variation and local residual stress within individual grains of pearlitic steel using synchrotron dark field x-ray microscopy. *Scripta Materialia*, 197:113783, 2021.
- [85] C. Yildirim, N. Mavrikakis, P.K. Cook, R. Rodriguez-Lamas, M. Kutsal, H.F. Poulsen, and C. Detlefs. 4d microstructural evolution in a heavily deformed ferritic alloy: A new perspective in recrystallisation studies. *Scripta Materialia*, 214:114689, 2022.
- [86] F. Zernike. Phase contrast, a new method for the microscopic observation of transparent objects. *Physica*, 9(7):686–698, 1942.

- [87] W. Zhang and K. Bhattacharya. A computational model of ferroelectric domains. part i: model formulation and domain switching. *Acta Materialia*, 53(1):185–198, 2005.
- [88] Guoan Zheng, Roarke Horstmeyer, and Changhui Yang. Wide-field, high-resolution Fourier ptychographic microscopy. *NATURE PHOTONICS*, 7(9):739–745, SEP 2013.



# A Appendices

## A.1 Fourier series & crystallography

A crystal is a periodic arrangement of matter. Because of the periodic arrangement of matter in a crystal, many physical properties of a crystal are represented by periodic functions of the same period as the crystal itself. In this section we introduce periodic functions and their *Fourier series* representation.

A periodic function,  $f(x)$  is defined by the equation,  $f(x+L) = f(x)$  for all  $x$ . The constant  $L$  is called the period. By successive application of the rule we see that the value of the function at any point  $x$  can be equated to the value at a point lying the interval  $0 < x < L$ .

In three dimensions, we need a set of three linearly independent vectors:  $\mathbf{a}$ ,  $\mathbf{b}$ ,  $\mathbf{c}$ . The value of the periodic function is constant after the addition of an integer times any of these three vectors to the argument. The choice of these *basis vectors* is not unique, but we will assume that it is given. Collecting the three vectors into a matrix,  $A$  and the three indices into a vector  $\mathbf{i}$ , we can write:

$$f(\mathbf{r} + A\mathbf{i}) = f(\mathbf{r}) \quad (\text{A.1})$$

the infinite set of vectors  $A\mathbf{i}$  for  $\mathbf{i} \in \mathbb{I}^3$  are called the crystal lattice. The parallelepiped constructed by drawing the three basis vectors from a common origin is called the unit cell of the crystal. The unit cell constructed by choosing  $\mathbf{r} = 0$  as the origin is called the first unit cell. Sometimes it will be useful to specify a position inside the crystal by a linear combination (might also be non-integer) of basis vectors,  $\mathbf{r} = A[p_1, p_2, p_3]^T$ . The length of such a vector is:

$$|\mathbf{r}|^2 = \mathbf{r}^T \mathbf{r} = \mathbf{p} A^T A \mathbf{p} \quad (\text{A.2})$$

The matrix  $T = A^T A$  is called the metric.

Periodic functions can be exactly represented by a Fourier series: an infinite sum of harmonic functions with a discrete set of spatial frequencies. In three dimensions, these spatial frequencies are three dimensional vectors and fall on a different lattice defined by:

$$\mathbf{h} = B[h, k, \ell]^T \quad (\text{A.3})$$

where  $h$ ,  $k$ , and  $\ell$  are three integers. These vectors have the units of reciprocal lengths and the lattice is typically called *the reciprocal lattice* of the crystal.  $B$  is a 3-by-3 matrix given by:

$$B = 2\pi A^{-T} \quad (\text{A.4})$$

In the special case of a cubic lattice, that is a lattice where the three lattice vectors are mutually orthogonal and of equal length,  $a$ , the reciprocal lattice is also cubic with the same orientation and length  $2\pi/a$ .

Using this, an arbitrary periodic function may be written:

$$F(\mathbf{r}) = \sum_{\mathbf{h}} c_{\mathbf{h}} e^{-i\mathbf{h}\cdot\mathbf{r}} \quad (\text{A.5})$$

The scalar constants  $c_{\mathbf{h}}$  are called the Fourier coefficients and can be calculated by *Fourier's trick*:

$$c_{\mathbf{h}} = \frac{1}{V_{\text{U.C.}}} \int_{\text{U.C.}} F(\mathbf{r}) e^{i\mathbf{h}\cdot\mathbf{r}} d\mathbf{r} \quad (\text{A.6})$$

where the integral is over a single real-space unit cell and  $V_{\text{U.C.}} = |\det(\mathbf{A})|$  is the volume of the unit cell.

## A.2 Properties of the continuous Fourier transform

In this chapter we define the form of the continuous Fourier transform used in the thesis and state the most important properties of the Fourier transform with this definition. We use a Fourier transform with full-period-frequencies following the convention in Fourier optics. The DFXM literature uses the letter  $q$  for normalized angular frequencies (Eq. (3.7)) so we instead choose the letter  $s$  following Guinier.

We define the direct continuous 2D Fourier transform, which takes a function,  $E$  defined on  $(x, y) \in \mathbb{R}^2$  and returns a function  $\tilde{E}$  on  $(s_x, s_y) \in \mathbb{R}^2$

$$\tilde{E}(s_x, s_y) = \mathcal{F}\{E(x, y)\} = \int dx dy E(x, y) e^{-i2\pi(xs_x + ys_y)} \quad (\text{A.7})$$

Along with this definition follows a definition of the inverse Fourier transform.

$$\mathcal{F}^{-1}\{\tilde{E}(s_x, s_y)\} = \int ds_x ds_y \tilde{E}(s_x, s_y) e^{i2\pi(xs_x + ys_y)} \quad (\text{A.8})$$

The inverse Fourier transform is the inverse of the Fourier transform:

$$\mathcal{F}^{-1}\{\mathcal{F}\{E(x, y)\}\} = E(x, y) \quad (\text{A.9})$$

for any function  $E(x, y)$  where the Fourier transform exists.

The Fourier transform is *unitary*, it conserves the L2 norm of the function. This is also known as Parseval's theorem:

$$\int dx dy |E(x, y)|^2 = \int ds_x ds_y |\mathcal{F}\{E(x, y)\}|^2 \quad (\text{A.10})$$

The following property, called the Fourier derivative theorem:

$$\mathcal{F}\left\{\frac{\partial}{\partial x} E(x, y)\right\} = i2\pi x \mathcal{F}\{E(x, y)\} \quad (\text{A.11})$$

The convolution theorem allows us to rewrite transforms of products. First we define the convolution of two functions denoted by the symbol:  $\otimes$ :

$$E(x, y) \otimes H(x, y) = \int dx' dy' E(x', y') H(x + x', y + y') \quad (\text{A.12})$$

The transform of such a convolution is a product of the individual transforms:

$$\mathcal{F}\{E(x, y) \otimes H(x, y)\} = \mathcal{F}\{E(x, y)\} \mathcal{F}\{H(x, y)\} \quad (\text{A.13})$$

Finally the Fourier shift theorem:

$$\mathcal{F}\{E(x - x_0, y - y_0)\} = e^{i2\pi(x_0 s_x + y_0 s_y)} \mathcal{F}\{E(x, y)\} \quad (\text{A.14})$$

